QATAR UNIVERSITY

COLLEGE OF ENGINEERING

DEVELOPMENT OF INTERNALLY PRESSURIZED

COMPOSITE/METALLIC/COMPOSITE HYBRID PIPES

BY

FATIMA GHASSAN ALABTAH

A Dissertation Submitted to

The College of Engineering

In Partial Fulfillment of the Requirements for the Degree of

Doctorate of Philosophy in Mechanical Engineering

June 2021

COMMITTEE PAGE

The members of the Committee approve the Dissertation of

Fatima Ghassan Alabtah defended on 19/04/2021.

_____
Prof. Elsadig Mahdi

Thesis/Dissertation Supervisor

_____
Prof. Hossam Kishawy

Committee Member

_____
Dr. Wael Alnahhal

Committee Member

_____
Dr. Anwarul Hasan

Committee Member

Approved:

_____

Khalid Kamal Naji, Dean, College of Engineering

ABSTRACT

Alabtah, Fatima, Ghassan, Doctorate: June : 2021,

Doctorate of Philosophy in Mechanical Engineering

Title: Development of Internally Pressurized Composite/Metallic/Composite Hybrid Pipes

Supervisor of Dissertation: Prof. Elsadig, Mahdi, Saad.

The challenge to the pipeline industry is to meet the increased worldwide demand while reducing the cost. Currently, metallic and composite pipelines are the most cost-effective way of transporting water, oil, and gas. Limitations of metallic and composite pipelines are familiar. Corrosion reduces the load-carrying capacity of metallic pipelines, while matrix cracking/abrasion causes the failure of the composite pipelines. Both corrosion and abrasion cause significant losses and decrease the structural integrity of pipelines. This work proposes a corrosion-free hybrid pipe, which will improve the pipeline's pressure capacity and eliminate internal and external corrosion. First, this research aimed to examine fiber type and fiber orientation's effects on the interface bonding between steel and fiber-reinforced composites. To this end, fracture loads for modes I and II were experimentally determined for FRP/steel samples with different fiber types and orientations. Results showed that fiber orientations and fiber types have significantly affected the interface bonding between the steel and fiber-reinforced composite. Second, a detailed investigation for the effect of the FRP overwrap system on the bending behavior of metallic pipes was presented, especially

in the presence of heat-affected zone in the case of welded pipes. It was proved that the use of the proposed FRP overwrap system had eliminated the effect of the heat-affected zone in welded / steel pipes, and the maximum bending flexural load showed a noticeable increase.

Third, the internal pressure capacity of hybrid composite/steel/composite pipes was tested according to ASTM D1599 standard. The testing results showed significant improvement in the internal pressure capacity compared to the conventional steel pipes. Fourth, a detailed evaluation of fiber type's effect on the electrochemical corrosion aspects in different highly corrosive solutions, 0.5 M NaCl, 0.5 M HCl, and 0.5 M H_2SO_4, was presented. Finally, the corrosion aspects of composite overwrapped steel pipes were evaluated. The FRP/steel pipes were immersed in a glass container containing the corrosive solutions and monitored for six months and one year. The corrosion condition was qualitatively analyzed using SEM, EDX and XRD analysis. Results showed an excellent corrosion resistance for the FRP/steel pipes compared to the conventional carbon steel pipes.

DEDICATION

I dedicate this work to my country, my motherland- beloved "Palestine".

ACKNOWLEDGMENTS

TABLE OF CONTENTS

LIST OF TABLES

LIST OF FIGURES

LIST OF ABBREVIATIONS

CFRP: Carbon Fiber Reinforced Polymer

EDX: Energy-Dispersive X-ray

EIS: Electrochemical Impedance Spectroscopy

FRP: Fiber Reinforced Polymer

GFRP: Glass Fiber Reinforced Polymer

KFRP: Kevlar Fiber Reinforced Polymer

MPH: Metal Polymer Hybrids

OCP: Open-Circuit Potential

PTFE: Polytetra Fluoroethylene

PVC: Polyvinyl Chloride

RFWT: Robotic Filament Winding Technique

SCE: Saturated Calomel Electrode

SEM: Scanning Electron Microscopy

XRD: X-ray Diffraction Analysis

LIST OF NOMENCLATURE

a is the crack progress length [m]

b is the sample width [m]

F is the critical load at [N]

δ is the corresponding displacement [m]

$G_{.C.}$ is the strain energy release rate [J/m^2]

$2L$ is the span length [m]

$K_{.I.}$ stress intensity for mode I [MPa$\sqrt{m}$]

K_{II} stress intensity for mode II [MPa$\sqrt{m}$]

$E_{.I.}$ is the effective moduli for modes I [GPa]

E_{II} is the effective moduli for mode II [GPa]

F is the Force acting on the beam [N]

E_x is the Modulus of Elasticity [GPa]

I_x is the Area Moment of Inertia [m^4]

T is the time of exposure [hours]

A is the area of exposure [m^2]

D is the density [g/cm^3]

CHAPTER 1: INTRODUCTION

1.1 Introduction

The pipeline, which is in high demand worldwide, is susceptible to operation problems prevented with composite materials. Metallic and composite pipelines are the most economical means for transporting water, oil, and gas in various applications [1]. Limitations of installed metallic and composite pipelines are well known. Corrosion degrades metallic pipelines' strength capacity, while matrix cracking/abrasion causes leakage of composite pipelines [2]. Both corrosion and abrasion cause significant losses and decrease the structural integrity of pipelines. Corrosion in the metallic pipeline can be classified into two types. These are external and internal corrosions. External corrosion is generally slowed down using organic coating and cathodic protection, while corrosion inhibitors are widely used to fight internal corrosion [3]. In the long run, the existing technology is not helping to eliminate internal corrosion. Medium-range pressure composite materials have been used in transportation and gathering systems for many years in the oil and gas industry [4].

Current technology has not fully met operation goals, especially in cost for distribution at higher pressures and more severe conditions (i.e., corrosive media). Alternatives to purely metallic or composite pipes are looked for to increase reliability and durability. Many researchers were interested in using hybrid pipes where FRP material is added to the conventional pipelines to eliminate matrix cracking and decrease the possible corrosion. In addition to producing pipelines that are overwrapped with FRP composite, FRP layers are also being used to repair the existing conventional pipes. FRP composites are worthy of their lightweight, corrosion resistance, and high-pressure capacity [5]. Recently, many manufacturers provided pipes made of steel with outer

wraps of glass or carbon-based composite layers. The idea behind the external layers of composite materials is to prevent/eliminate external corrosion and add extra strength to the pipe [6]. The thickness of these layers is a bit higher than the standard coating. Most FRP applications in pipelines were for repair purposes, where an FRP wrap is a permanent, economical and effective repair technology [7]. Extensive research was carried out on the repair of damaged pipes due to corrosion with fiber-reinforced composite wraps. The advantages of using composite repairs are that there is no need for high temperature to apply them; they could be applied to the pipe while it is in operation. They have corrosion resistance, and minimal facilities are required on site. The lifetime of a composite repair is 20 years, according to ISO/TS 24817 (2006) [8]. Also, welded pipes repaired from defects with FRP were reported to maintain mechanical strength at high pressures without leakages [9]. Oil and gas pipelines received most of the literature's attention concerning restoring strength after localized metal loss, considering FRP composites for their high-pressure capacity and durability. FRP has been investigated in characterization and failure pressure studies, mainly with the use of glass fibers and epoxy resin [10] [11] [12]. Composite materials proved reliable for repairing damaged pipes, increasing burst pressure, and reducing strain.

1.2 Motivation

Due to the increase in population and industrial development, petroleum products' demand as crude oil and natural gas also increased. It is essential to have high-strength materials that can be utilized in pipelines. The usage of composite pipes in the oilfields has been accepted and in service for many years, but the pressure range is low to moderate. However, the existing oil and gas pipeline technology cannot be extrapolated to achieve the cost and performance goals required to implement a vast distribution

network successfully. Experts in the oil and gas industry agreed that higher operating pressure transmission pipelines are needed to reduce corrosion costs. Researchers are trying to find an alternative to the conventional metallic pipe and the pure composite pipelines to increase demand, be competitive and preserve safety and reliability. Hybrid systems using advanced alloys and composite materials fiber-reinforced polymer (Steel/FRP) fascinated substantial attention since they have a low material cost and great load-bearing capacity. This hybridization can deliver better design freedom and different potentials for efficient integration[13]. However, the fabrication process of MPHs is not an easy subject since both materials have different physical and chemical properties. These differences end up with some fabricating difficulties, for example, the imperfect bonding between conventional materials and composite materials [14]. The most challenging part is to reinforce the steel pipes with FRP composite from inside. This challenge is the main driving force behind this research. Also, when used in the chemical industry, the FRP may be degraded due to abrasion, change in brittleness, delamination, separation of fiber from the matrix, and the matrix's degradation in highly corrosive environments. Some researchers investigated acid solutions' effect on the GFRP/epoxy mechanical properties, durability, and performance. But most of the existing studies are based on short immersion times. Moreover, there is no recent research related to the study of corrosion behavior of FRP/steel under long-term immersion in a highly corrosive environment. In this work, the interfacial properties, bending behavior, internal pressure capacity, and corrosion behavior for the hybrid composite/steel pipe are investigated.

1.3 Research Objectives

This research aims to develop a corrosion-free FRP/steel/FRP hybrid pipe to improve

3

the pipeline's pressure capacity and eliminate internal and external corrosion. The detailed objectives of this study are as follows:

- Examine the interfacial bonding between the metallic and the internal and external composites by examining fiber type and fiber orientation's effects on the interface bonding between steel and FRP composites.

- To investigate the effect of the FRP overwrap system on the bending behavior of steel pipes.

- To develop an innovative, flexible system to reinforce the innermost surface of the pipe.

- To test the internal pressure capacity of the FRP/steel/FRP pipes.

- To study the effect of fiber orientation on the FRP/steel/FRP pipes' pressure capacity.

- Evaluate the hybrid composite/steel pipes' performance under harsh corrosive conditions and evaluate its electrochemical corrosion aspects.

1.4 Outline of the Dissertation

This dissertation consists of eight main chapters. The details of each chapter are as following:

- Chapter 1 introduces the present context and motivation of the research.

- Chapter 2 surveys the literature re the different FRP composites' applications in pipelines, their development over time, and the current state of the art of pipeline fabrication and repair using FRP composites.

- Chapter 3 presents a detailed investigation of the effect of fiber type and fiber

orientation on the interface bonding between steel and FRP composites.

- Chapter 4 provides a detailed explanation for the FRP overwrap system's effect on metallic pipes' bending behavior.

- Chapter 5 introduces the innovative, flexible system for hybrid pipeline fabrication and presents the effect of different winding angles on the FRP/steel/FRP pipes' internal pressure capacity.

- Chapter 6 provides a detailed evaluation of fiber type's effect on the electrochemical corrosion aspects in different highly corrosive solutions.

- Chapter 7 addresses the performance of the hybrid composite/steel pipes under long-term immersion in different corrosive environments.

- Chapter 8 presents the overall current research work conclusion and recommends future work for an improved hybrid pipe performance.

CHAPTER 2: LITERATURE REVIEW

In operation, pipelines are being increasingly used worldwide to meet higher transportation demands for strategic fluids while optimizing costs. Fiber-reinforced polymer (FRP) composite is used in many pipeline industries of water, oil, and gas transportation since they could resist corrosion and have lighter weight to high strength ratios. FRP composite pipes are getting cheaper in installation costs, favored in various applications. FRP has good mechanical properties, which improve stiffness, strength, pressure capacity, durability, cost-benefit, and environmental footprint when combined with other materials. This chapter covers different FRP composites' applications in pipelines and their development over time. It reviews the pipelines based on the transported fluid and reviews the developed composite pipelines and the repaired conventional pipelines against corrosion or leaking using different FRP types. The review includes the most common way to employ FRP composites in different pipeline applications. Different designs and applications of FRP composites in pipelines towards achieving enhanced properties are summarized and compared.

2.1 FRP Composite in Conventional Pipelines

Composites consist of base material and filler material. The term matrix refers to the base material that incorporates the filler material. The matrix works typically as adhesive to tie the fiber up together and shift the applied loads to fibers. Furthermore, they behave as a barrier to protect them from physical, environmental, and chemical defects. Filler material could exist in the matrix as fibers or particles or others, synthesized or extracted from natural sources. Fibers (from 30 to 70% in volume and nearly on average 50% in weight [15]) carry the load and influence the mechanical properties of the composite substances overall [16] [17]. The mechanical properties of

6

composites, especially shear strength, transverse strength, and compressive strength, are influenced by the matrix material properties [18]. Matrices are typically selected based on the design requirement temperature of the desired composite structure. For low-temperature applications, the polymer is a suitable choice, and for high-temperature requirements, ceramic is usually used. Ceramic and metal matrices have a high cost. Because of the different benefits of polymers, they are applied as matrix materials in many of pipeline applications. The main advantages of polymers for this purpose are the low cost, good endurance against chemical defects, ease of processing and lightweight [19]. Polymer matrices are mainly divided into thermosets and thermoplastics. When thermoset polymers are heated, irreversible chemical changes take place between polymer molecular bonds. Therefore, by heating this material they can be cured to the desired shapes. Thermosets are commonly used in current applications, even though they have small share in the PMC industry, synthesized as nonreactive solids even under heat and pressure when applied. Thermoplastics however respond to heat for reshaping.

2.1.1 Single-Fiber Composite System

The fibers' selection depends on the desired properties required in finished composite structures and the application [20]. Density, tensile and compressive strengths, tensile and compressive moduli, fatigue strength and failure mechanism, and other properties are influenced by the type, volume fraction, length, and fiber orientation [21]. In the engineering applications of FRP composites, there are two primary fibers: synthetic and natural fibers. The most used synthetic fibers are Glass, Carbon, and Aramid (Kevlar).

2.1.1.1 Glass Fibers-Reinforced Composites

Glass fibers are economical and commonly used reinforcements for their excellent mechanical and insulating properties and deterioration resistance [22] [23]. From the literature, it could be noticed that thermoset resins with glass fiber are dominant. There are only a few applications for the use of thermoplastic resins in pipeline applications. Thermoset resins can easily form on pipe walls, harden quickly, and are deterioration-resistant, making them of common choice in the field. The most used thermoset resins include epoxy, polyester, vinyl ester, phenolic, polyurethane, and polyamide. The most used resin type among them with glass fiber in pipeline applications is epoxy because of the sound mechanical, adhesion, shrinkage, and cure properties and corrosion, heat resistance and are more resistant to most common chemicals. [24]. numerous studies experimentally tested the use of glass-reinforced polymers (GRP) pipes in different applications. Figure 1 consolidates pressure and corresponding pipe diameter for a design for different applications.
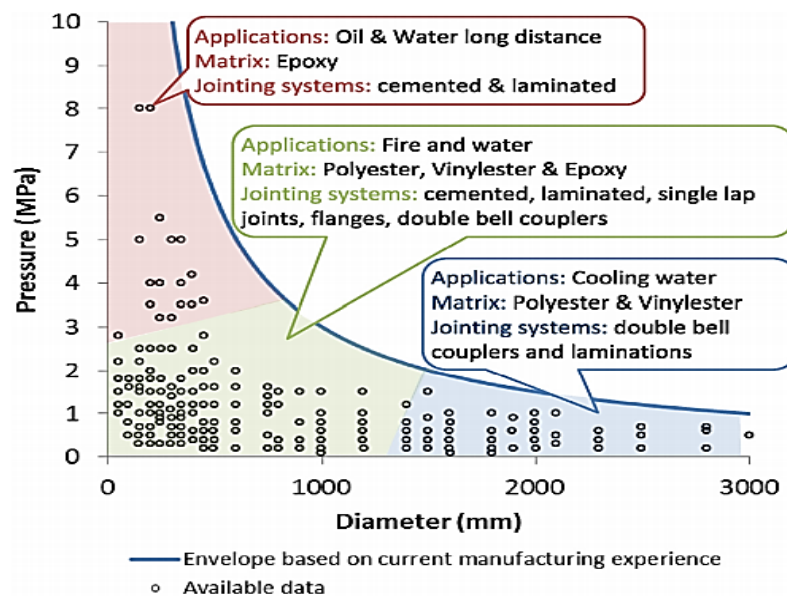
Figure 2. Pressure and diameter of GFRP pipelines (EN ISO 14692) [25].

2.1.1.2 Carbon Fiber-Reinforced Composites

Carbon fibers are electrically conductive, inducing higher susceptibility for galvanic corrosion when used in fastener applications [26]. CFRP composites should generally contain at least a 40% fiber volume fraction for failure probability to be less than that of uncorroded steel pipe [27]. In the literature, review most of the pipeline applications includes epoxy resin with carbon fibers. CFRP in pipelines increases strength/weight ratio and burst resistance. Kong et al. repaired a defected steel pipe with carbon fiber and epoxy resin (putty filling) [28]. The burst pressure tests like on the pipe shown in (Figure 3) indicated the load transfer from the pipe material to the wrapped CFRP depends on the length of the defect in hoop direction, up to 20% less than the pipe diameter, for confinement after breakage of the brittle putty.
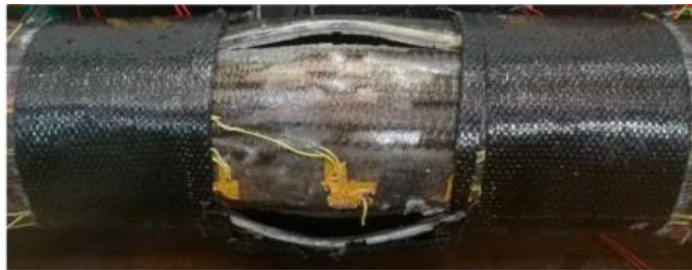
Figure 3. Failure of the repaired steel pipe with CFRP material under burst test [28].

2.1.1.3 Aramid (Kevlar) Fibers-Reinforced Composites

Aramid fibers are lightweight and have superior strength and elasticity modulus (by 2 to 3 times as glass fibers) and high corrosion and temperature resistance (by as 500ºC) [29]. Aramid fibers are used in many pipeline applications, with both thermoset and thermoplastic resins. Aramid fiber's mechanical properties with thermoplastic resins received attention from many researchers, such as Kruijer et al. [30]. The new class of polyethylene liner pipes overwrapped with non-impregnated, twisted Aramid cords in two layers was fabricated. The Aramid yarns were embedded in a polyethylene (P.E.)

matrix of high density and viscoelastic response (Figure 4). Upon pressuring, the pipes showed a torsional response complex in a model that needed to consider the matrix's viscoelastic properties.
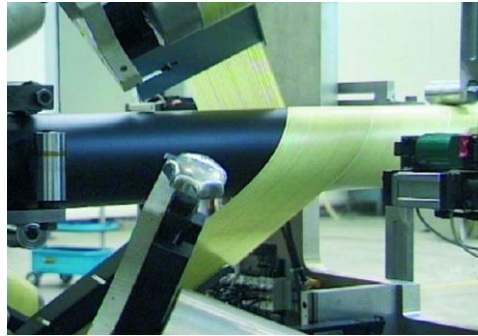
Figure 4. The twisting wrapping process for aramid fiber layer [30].

Guoquan et al. studied a similar aramid thermoplastic-resin to evaluate the thermostability of polythene (PE-RT) pipes reinforced with aramid-based, polyolefin resin matrix at high temperature for water transport (Figure 5) [31]. When applying the water pressure blasting test on the pipe, it was found that the aramid/PE-RT pipe satisfied the operation demands of 20-yr service for a service of 20 years, at high 95°C and 4 MPa conditions.

Figure 5. failed aramid fiber reinforced pipe under internal pressure at 90 °C[31].

Aramid FRP could also be used in joining pipes. Farag et al. used a new joining method with fiber-reinforced aramid about fiber orientation angles under three-point bending [32]. The wet fabric wrapping technique was utilized to fabricate the FRP joining, and

it was tested under three-point bending loads (Figure 6). The results revealed that the FRP joining system enhances the flexural capacity when compared to conventional joining methods as welding.

Figure 6. failure of AFRP joining after 3-point bending test[32].

Despite their strength and resilience, Kevlar fibers have several disadvantages, which restricts their efficiency. It can absorb moisture faster than glass and carbon fibers, meaning it is more sensitive to its surrounding environment [33]. Kevlar fibers are weaker in compression than comparable filaments of high strength, high modulus. The fracture was reported to occur without plastic deformation in the matrix [34]. Deteresa et al. reported, for Kevlar fibers, that tensile strength/compressive strength ratio was 5:1, tensile strength/shear strength ratio was 17:1, and tensile modulus/shear modulus was 70:1 [35]. Allred et al. reported that transverse moisture had measurable effects on aramid/epoxy composites at 25°C, 14% stiffness loss, 35% strength loss, and 27% elongation loss [36].

2.1.1.4 Natural Fibers-Reinforced Composites

Natural FRP is generally advantageous over synthetic FRP in environmental footprint, recycling, and cost[37][38]. Danasabe[39] and Danasabe et al.[40] applied water absorption tests on the banana stem and doum-palm PVC composite pipes, respectively (Figure 7). The composite pipes with Kankara clay as a filler were utilized with low-cost materials of good mechanical and weight properties, with lower density and higher

water absorption, respectively, with higher fiber content.

Figure 7. Banana stem reinforced PVC composite pipe [39].

Shi et al. studied pipes made of bamboo and evaluated the environmental footprints across from the extraction phase of raw material to the end of service [41]. A pipe was fabricated from bamboo fiber and urea-formaldehyde resin, which is a class of thermosetting resins. The pipe was made with high-tension winding (Figure 8. The bamboo winding composite pipes in the installation site [41].). Compared to the conventional PVC pipe, the bamboo pipe's life cycle assessment revealed that all significant environmental impacts, burdens, and cumulative energy demand were reduced.
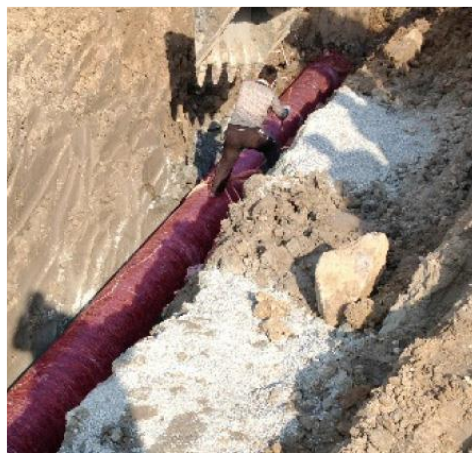
Figure 8. The bamboo winding composite pipes in the installation site [41].

Even though natural fibers have many benefits, they are not a good fit to utilize in pipe manufacturing, especially in filament winding techniques. The challenges are related

to the short length of fibers, as winding requires continuous fibers and high tensile strength (to withstand pulling forces) [42].

2.1.2 Hybrid Fiber Composite System

Hybrid composites contain more than one reinforcement material in the same matrix, where usually one fiber type has a more considerable failure strain than the other. They are termed as high elongation and low elongation fibers, respectively [43]. One of the advantages is that hybridization enhances energy absorption [44]. Moreover, in hybrid FRP composites, the mechanical properties could be tailored perfectly because of the combination of high tensile strength and high failure strain elements [45]. Hybrid fibers could be combined in configurations shown in Figure 9. In the interlayer configuration, the layers of two fiber types are wound alternatively in a cheap and straightforward technique. In the intralayer hybrid configuration, two fiber types are combined. In intrayarn hybrid configuration, two fiber types are mixed fiber by fiber. A complex configuration involves combining any two of the abovementioned configurations, as an inter yarn hybrid configuration can be mixed with a homogenous yarn configuration [46].
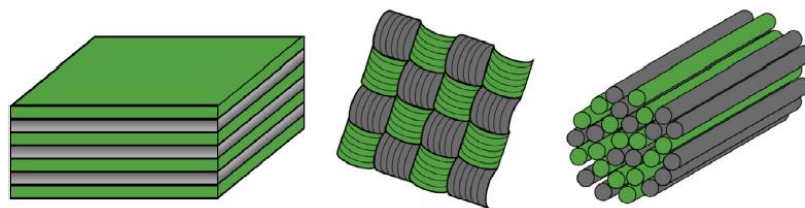
Figure 9. The three main hybrid configurations: (a) interlayer or layer-by-layer, (b) intralayer or yarn-by-yarn, and (c) intrayarn or fiber-by-fiber [46].

The interlayer hybrid FRP composite is the most used fiber hybridization technique in polymer composites in pipeline applications. According to the literature, most of the

hybrid FRP composites applications in pipelines include glass and carbon fibers and epoxy resin. Galvanic corrosion across CFRP laminates and pipe metal can be inhibited by one GFRP layer on the surface. Zongchen et al. evaluated the crack growth on an external pipe surface reinforced with hybrid carbon/glass FRP composite [47]. FRP layer was applied using the hand lay-up method (Figure 10). A fatigue test on the pipe was carried out with four-point bending. The FRP layer decreased the fatigue crack growth, and the reinforcement limited deformation noticeably.
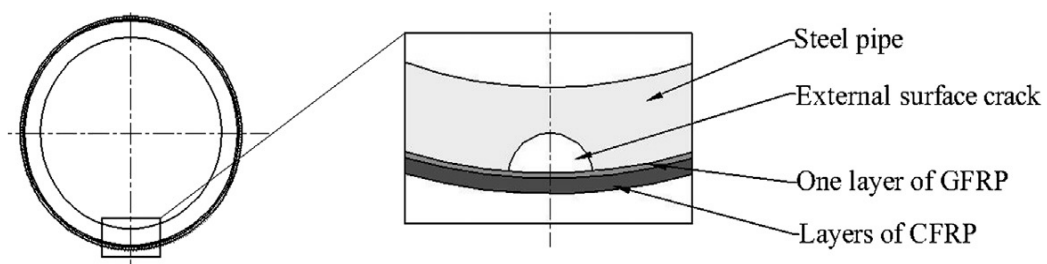
Figure 10. The configuration of the reinforced pipe specimen [47].

Many researchers investigated repaired steel pipes' behavior with hybrid glass/carbon FRP composite under flexural bending loads and a combination of axial compression and bending loads. Dong [48] evaluated the flexural response of composite pipes reinforced with hybrid carbon and glass fibers. He also used FEA to model pipe failure during three-point bending, with wrapping angle and fiber volume fraction as model parameters. The pipe resisted top bending load at ply angles of 60° to 75°, of failure loads comparable to those of carbon fiber or glass fiber composite pipes. Hybrid pipes can have better cost and weight characteristics, therefore, with better-optimized locations of failure initiation. In another work, Dong [49] evaluated optimum designs of carbon and E glass hybrid pipes with FEA, modeling the pipes under flexural loading. They reported that carbon and E glass fibers have good weight/cost characteristics (compared to carbon and S glass fibers) in Figure 10, but reinforcing the

pipes with mostly carbon fiber achieves higher failure loads.
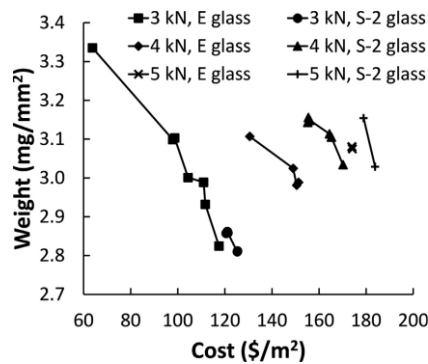
Figure 11. optimal candidate points for the relation between weight and cost at different failure loads from non-dominated sorting GA-II (NSGA-II) [49].

George et al. evaluated steel tubes' response rehabilitated with hybrid glass/carbon FRP composite when subjected to axial compression and bending in combination, pictured in Figure 12 [50]. THE tested FRP layer involved a first layer made of triaxial E-glass woven cloth (preventing galvanic corrosion) and a second layer that involved CFRP (for the strength of repair).

a-   b-

Figure 12. Repaired specimens (a) while and (b) after combined axial compression and bending testing [50].

Some specimens were repaired in exposure to air and others in the water, in Figure 13, as foam blasting is applicable for surface preparation in any condition. Strength regain ratios of the two repairs were analyzed, showing comparability. One layer of GFRP and

two layers of CFRP sufficed in restoring capacity in pipes damaged in 20% wall thickness from corrosion.

Figure 13. Repairing in water with hybrid glass/carbon layers [50].

Another type of hybrid fiber composite system is the hybrid Textile Tape that consists of two fiber types woven together in one fabric; this hybrid fabric type provides an extreme strength when used with epoxy resin [51]. Singh et al. analyzed a repaired steel pipe's strength using Glass-Carbon Textile Tape (Figure 14) numerically and experimentally [52]. The burst pressure was higher by 20%, verified by hydrostatic pressure tests for high-pressure crude transportation.

a-   b-
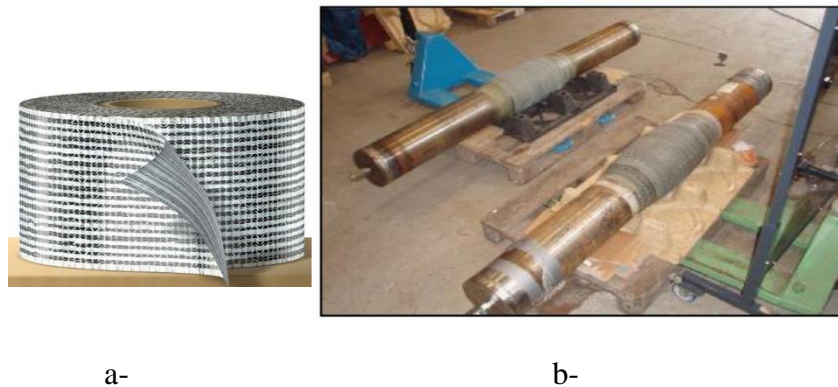
Figure 14. a- Glass-Carbon Textile Tape, b- repaired steel pipes [52].

Table 1 presents a summary for the previous section by comparing the characteristics of the most used polymeric fibers, namely, carbon, glass, and aramid (Kevlar) fibers.

Table 1. Comparison for the characteristics of different polymeric fibers.

	Glass FRP Pipe	Carbon FRP pipe	Aramid FRP pipe
Fabric Cost ($/kg) [53]	1-2 (cheapest)	35-60	50-150 (most expensive)
Density g/cm3	≈ 2.5 (heaviest)	≈ 1.8	≈ 1.44 (lightest)
Tensile Strength (MPa)	≈ 2200 (lowest)	≈ 3500 (Highest)	≈ 3200
Corrosivity	corrosion resistance	corrosive	corrosion resistance

2.2 Fabrication Processes using FRP composites

Composite components are fabricated in a variety of ways. Selection of fabrication method is as crucial as design and application by end-user. The most known fabrication process of FRP composite pipes and composite overwrapped conventional pipes is filament winding. Pipe's filament wounds are common and are extensively used in onshore and offshore oil and gas applications, including pipes (in different diameters, pressure vessels, storage tanks). Short fibers and resin are typically applied with centrifugal molding, also utilized in FRP sewer liners, water tanks, and drainage components [54]. Other fabrication processes that allow continuous production of FRP structural shapes are pultrusion and pull winding, which can produce pipes with constant cross-section.

2.2.1 Filament Winding

Filament winding is one of the most frequently used fabricating processes using continuous fiber-reinforced resin composites. It has the advantage of high productivity, low cost, and a high strength-to-weight ratio [55]. In filament winding, fibers are passed through a resin bath and woven onto a mandrel rotating at specified rotational speeds

or onto the pipe (of conventional type) itself to become a layer providing strength or protection, along a geometrically predetermined path of controlled tension, to be later cured and demolded, shown in

Figure 15 [56]. The winding machine typically has numerical X, Y, and Z axes for linear motions and A, B, and C axes for rotational motions. Figure 14 developed from being 2-axis, a lathe to a 6-axis type machine [57].

a-   b-
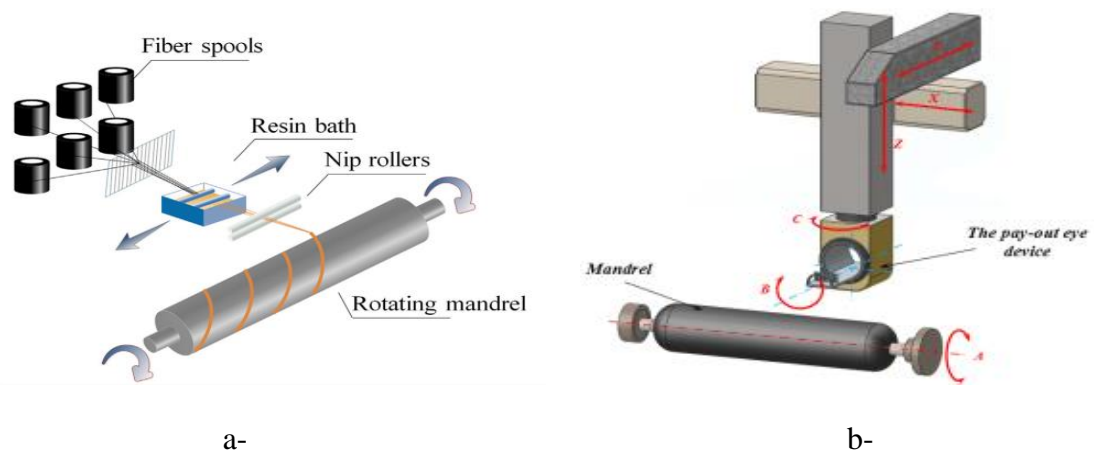
Figure 15. a-Schematic of the filament winding process [58], b- Filament winding numerically controlled axes configuration [57].

Abdalla et al. designed a low-cost, lathe-type winding machine for pipes (of up to 100 mm diameter and 1000 mm length) and round specimens fabrication [59]. The winding orientation was from 20 to 90º, with single glass fiber through the pre-catalyzed resin. The curing process was carried out at room temperature and in oven conditions. The technique reported was efficient and precise for mandrels of different shapes, producing composite parts for different applications, and strongly correlated to the materials, winding angle, fiber, resin composition, and curing. Later in more recent research, Quanjin *et al*. evaluated a 3-axis winding machine's experimental performance in circular repeatability in winding and angle quality, using circular winding testing and

winding angle measurement methods [60]. They reported satisfactory 0.83 to 1.13 mm winding circular distance with nearly 3% standard deviation and angle quality on 0.35 to 0.62° difference. The machine and the carbon/epoxy tubes evaluated are in Figure 16. The authors reported the evaluation of winding circular distance at different angles with time, mentioning that 75° winding angles offered optimum reliability quality, with nearly 0.8 mm distance value. The higher the winding angle, the lower the difference value. It was concluded that the machines of type offer optimum products at high winding angles.
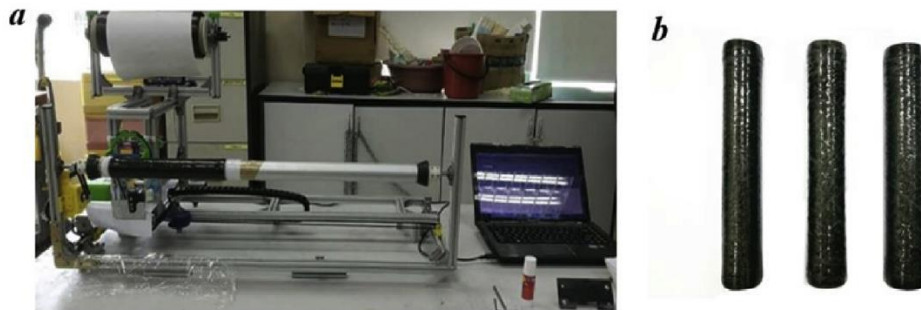
Figure 16. Equipment: (a) portable 3-axis winding machine; (b) filament wound carbon reinforced plastic tubes [60].

Some researchers also investigated the ability of filament winding machines to produce more complex shapes. Rojas et al. worked on unifying a filament winding technique for complex shapes using a validated generic mathematical model [61]. The validation was carried out experimentally with the four-axis winding machine. The approach addressed manufacturing limitations, used the theory of surfaces for describing curvatures, and used the slippage tendency of fiber over the surface to establish a local stability criterion. The solved general path equation was developed to become the basis for studying the mechanical response in association with filament winding parameters. The friction function was introduced to describe fiber stability more precisely. For

future works, the author's associated suitability of filament winding models to the technological techniques. The next revolution of filament winding was the Robotic filament winding technique (RFWT), in Figure 17. The technique allowed for winding complex shapes and patterns and new winding approaches surpassing the limitations of the numerically controlled axes [62][63][63]. Quanjin *et al*. consolidated a report on RFWT in the industry about fabrication processes, where the RFWT has more than six axes [57]. Compared to the traditional techniques that involve lathe type and multi-axis structures (used for fabricating composite tubes and vessels, for example), robotic techniques involve machine structures (that can be used for fabricating non-symmetrical and core-less components).
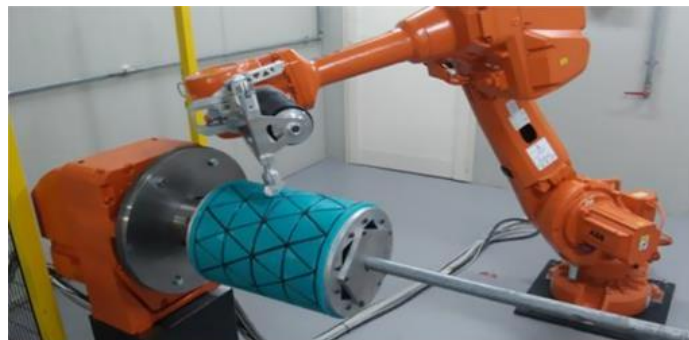
Figure 17. Robotic filament winding technique [62].

It is essential to understand how primary processing parameters that the operator can monitor and control; (as the tow tension) can affect the quality of the fabricated pipe. Mertiny *et al*. evaluated the correlation between the physical and mechanical properties (parametrized with the volume fraction of fiber and wall thickness) of glass-fiber reinforced polymer tubes and the applied tow tension at different ratios biaxial loading [64]. They reported that the greater the fiber is tensioning, the greater the strength against failure with fiber-dominated loading. Interestingly, with less fiber tensioning, failure showed delay with matrix-dominated loading. Also, the volume fraction was

proportional to winding tension, as shown in Figure 17.
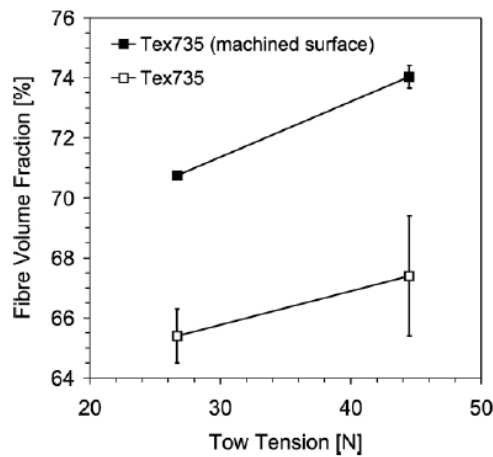
Figure 18. Relationship between fiber volume fraction and winding tension [64].

Wang et al. used filament winding mechanics for three models on void growth and fiber volume fraction about time-dependent manufacturing parameters [58]. The three models covered the diffusion-controlled, thermo-chemical, and resin flow for void growth about fiber volume fraction. The authors introduced resin pressure and processing temperature to predict the void size better. They reported that the higher the winding tension and the lower the humidity, the smaller the voids' size, and the higher the fiber volume fractions, the better the quality. Experiments on filament winding cylinders validated the results. Fiber volume fractions in filament-wound composite pipes range nearly from 48% to 54% [65]. In the last decades, many researchers investigated the effect of winding angle on the pipe's mechanical integrity [66][67]. Experimental and numerical simulation data indicated that deformation and failure mechanisms depend on the winding angle. In the closed-end testing mode, maximum axial and hoop stresses occurred at a winding angle of 55 ° when comparing specimens with pure angle-ply lay-ups [68]. However, multi-angle lay-ups, Multi-angle wound structures were more advantageous than pure angle-ply lay-ups in damage resistance under different load conditions [69].

It should be noted that optimum winding angles depend on loading modes. Hamed et al. found that for hoop pressure loading (mode I), the winding is optimum at 55°, for biaxial pressure loading (mode II), the winding is optimum at 75°, and for biaxial pressure with axial compressive loading (mode III), the winding is optimum at 85° [70]. In recent research, Colombo *et al*. carried out an optimization study on composite pipes' winding parameters based on the long-term mechanical reliability [71]. The critical optimization parameters were pipe wall thickness, fiber type, fiber volume fraction (reported optimal between 40 to 60%), and winding angle (reported optimal between ±44.5° to ±52.5°) – about internal pressure and axial loading. The authors first considered the properties and contents of fiber and matrix to estimate mechanical response from micromechanics models. The optimized parameters and minimum wall thickness were obtained from the internal pressure testing, and failure criteria before a recent ISO were implemented for a combined pressure and axial loading.

2.2.2 Pultrusion and Pullwinding

Fiber reinforcements and resin matrices, commonly glass fiber and polyester resin, can be converted into finished composite components with pultrusion, a continuous and well automated manufacturing process [72] [73][74][75][76]; for high-pressure applications, graphite or hybrid fiber (higher elastic modulus) with epoxies or thermoplastics are pultruded [77]. In the pultrusion process, continuous fibers are pulled off and immersed in a liquid resin bath. The impregnated fibers leave the bath to a series of wipers to get rid of the excess resin. After this, the fiber-resin bundles pass through a collimator before entering a heated die, which has the shape of the pipe. As the fiber/resin material goes through the die, it will be formed and the resin will be cured[78] (Figure 19).
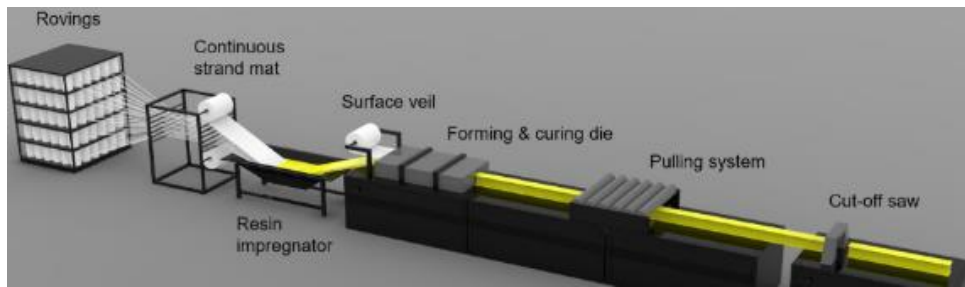
Figure 19. Pultrusion process [79].

The dies' average length is around 1 m long, and there should be a sufficient curing time before pulling out the pipe. The pulling speed is in the range of 10 to 200 cm/min. Pultrusion is a continuous fabrication process where the final cured pipes are pulled out by mechanically or hydraulically driven grippers [80] with fiber volume fraction between 35 to 60% for the pultrusion process [81]. The main pipeline application for the FRP pultrusion pipe includes delivering and supplying drinking water, waste and rainwater drainage, and agricultural irrigation [82]. While to produce FRP pipes with enhancing rigidity and mechanical resistance, a pull winding process is used. Pullwinding differs from traditional pultrusion in roving being placed in the longitudinal direction and circumferential direction, illustrated in Figure 19 [83]. Pull winding products are 20~30% more expensive than pultruded profiles because of the more complicated process [84].
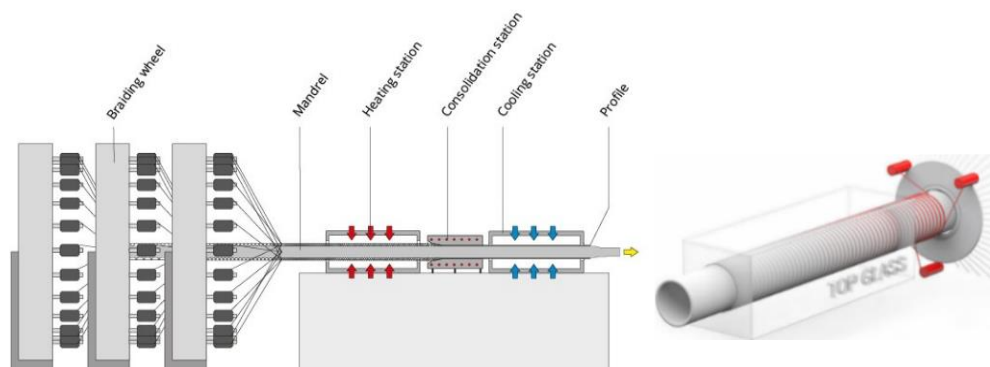
Figure 20. Pullwinding Technology [85].

2.3 Pipeline Repair Processes Using FRP Composite

Damaged pipes that get repaired with FRP composites are mostly made from steel or metallic for their pressure containment capability, reliability, and safety [86]. Steel is susceptible to corrosion occurring from salts, minerals, and sulfur in the water. The traditional way of dealing with damage induced by corrosion was removal or welding, which involves mobilizing equipment and difficulties, especially if it is underwater [87]. Alternatives have been investigated based on lightweight materials and effectiveness [88]. Generally, three main repair situations are involved in pipework based on the type of damage; pipe subjected to external damage (e.g., corrosion and mechanical damage), internal damage (corrosion and/erosion), and through-wall defects (leaks). Repair with FRP materials is documented as an ideal alternative repair method for damaged pipelines and piping systems [89]. Ordinary FRP pipe does not conduct electricity and has improved electrical properties than steel pipes [90]. The viability of this repair solution has been demonstrated by numerous field research.

Different types of fiber were used by Toutanji and Dempsey [91] to repair steel pipes. Carbon fiber was better than glass and aramid in enhancing pressure capacity, strength, and corrosion. Recently, many manufacturers provided pipes made of steel with external wraps of glass or carbon-based composite layers. The idea behind the external layers of composite materials is not only to prevent/eliminate external corrosion but also to add extra strength to the pipe. The thickness of these layers is a bit higher than the standard coating. Several systems have been developed to address corrosion in pipework; these systems allow repair to occur without shutting down gas flow, purging the pipeline, or cutting into the pipe. A permanent, economic and effective repair technology is composite wrap [7]. The advantages of using composite repairs are that

there is no need for high temperature to apply them; they could be applied to the pipe while it is in operation. They have corrosion resistance, and minimal facilities are required on site. The lifetime of a composite repair is 20 years, according to ISO/TS 24817 (2006) [8]. Welded pipes repaired from defects with reinforcement were reported to maintain mechanical strength at high pressures without leakages [9]. FRP was part of rehabilitation strategies of sewer, wastewater, and low-pressure lines [92]. There is still ongoing research worldwide to better understand the mechanics of repaired composite pipes, involving three types of FRP-based techniques, hand lay-up, pre-cured, and prepreg layered.

2.3.1 Hand Lay-Up System

For thermoset composites, hand lay-up is commonly considered in fabrication. The process involves impregnating the fiber reinforcement with resin and bonding it to the external or internal pipe surfaces. The technique applies to a variety of geometries such as those of valves and elbows (limited to low-to-medium pressure applications) and effective in restoring the strength of damaged components from defects and corrosion attacks [87] [93]. For FRP, the technique utilizes a 20 to 30% volume fraction of fiber [81], carried out with the surface's preparation, cleaning from rust and sandblasting, and pasting the laminate onto the steel surface, as shown in Figure 21 [47].
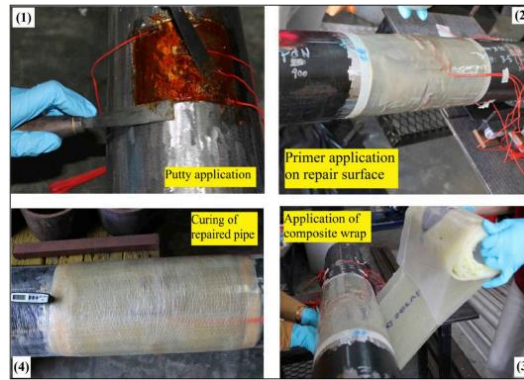
Figure 21. Application of composite wrap on the defective pipe.

2.3.2 Prepreg

Prepreg is reinforcing fabric pre-impregnated with epoxy that was cured partially to ease handling [94]. Several researchers investigated cracked metallic pipes' performance in the last decade when repaired with prepreg patches [95][96]. Benzene et al. [97] compared the performance of repaired APIX65 steel pipelines without patches and with patches applied in single and double configurations. By computing the stress intensity factors (SIF) at the crack tip, it was found that the SIF for a typical crack length of 10-20 mm was decreased by utilizing a double-sided patch which enhanced the fatigue life of the pipeline materials (Figure 22).
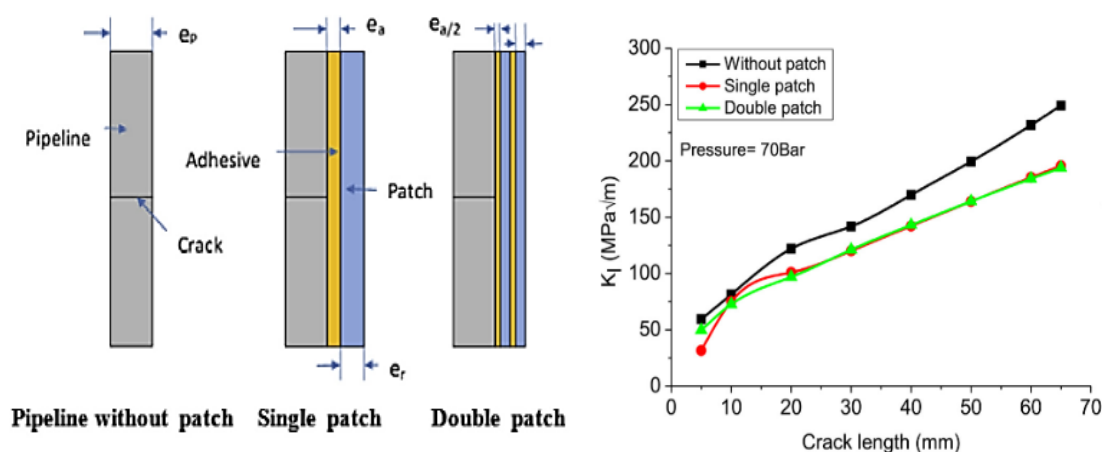
Figure 22. a- repaired pipes, b- SIF for single and double patches correlated with cracking length [97]

In recent research, Liu et al. [98] studied fatigue of cracked aluminum alloy pipe repaired with the CFRP prepreg patch. The patches were preheated on the pressure-heating machine for 15 min and 37°C temperature. The preheating process softens the resin in each prepreg and combines the patches, and they were glued to the pipe using an epoxy adhesive layer (Figure 23). It was established that the CFRP patch could improve the fatigue performance of the cracked aluminum pipe, especially when screw-thread surface treatment is applied.

a-   b-   c-
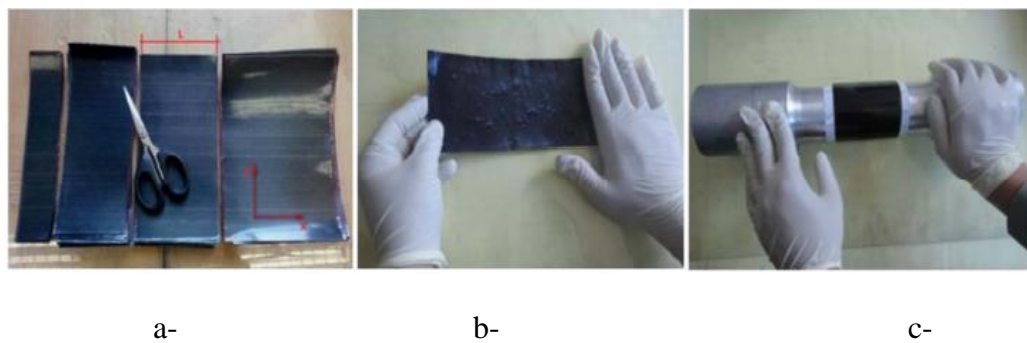
Figure 23. a- cutting, b-folding, c-wrapping specimen [98].

2.3.4 Pre-Cured Layered System

The composite layers bonded on the external surface with an adhesive after pre-curing, illustrated in Figure 23. This system enhances the mechanical performance in proportion with the volume fraction of fiber, which is commonly oriented in the hoop direction to better the damaged pipes [87].
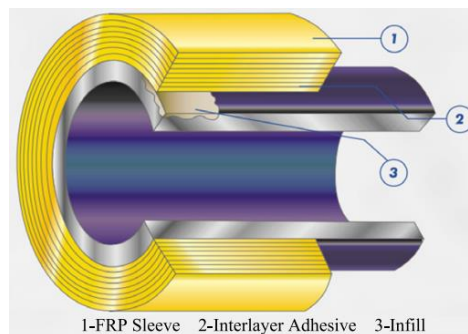
Figure 24. Pre-cured layered system [99].

Mazurkiewicz et al. analyzed pressure capacity and bucket teeth penetration, and they calculated the toughness of a steel pipe repaired with wrapping with fiberglass composite sleeve [100]. They reported the new system had higher capacity and strength than the original pipe with 18 mm thick epoxy resin.

2.4 Pipeline Applications Using FRP Composite

FRP composites are used in many pipeline applications because of their features. The fatigue endurance and the strength-to-weight ratio of FRP pipes are vital attributes associated with replacement costs and the ability to design lightweight, high-performance pipe systems [101]. Many researchers investigated the ability to extend the fatigue life [102], strengthening the durability [103], and enhancing the stability [104] of the conventional pipelines using FRP composites. The main pipeline applications where the FRP composites are employed are detailed in this section.

2.4.1 Water Pipelines

Water pipes have been manufactured with various materials in different sizes (diameter and thickness) utilized for different water-related uses. FRP composite pipes have been in use for a long time in water transport and distribution [105] [106] [107], such as their employment in hydroelectric plants, like in Brazil, in 1128 m of fiber-reinforced polyester pipes. FRP pipes were considered better than steel in weight, cost, and damage resistance [108]. In the US, Kevlar-reinforced polymer liners are extensively used for high-pressure water lines [109]. In this section, a summary of uses, materials, fabrications, conditions, failures, experimental procedures is outlined about the most common types of composites. Al-Mahfooz et al. evaluated the feasibility of glass fiber reinforced polymer (GFRP) overwrapped onto PVC pipes to pursue better flexural load-carrying capacity, which increased to as high as 1140 N against nearly 60 N of

pipes without reinforcement [110]. The ultimate flexural load was 9 times higher, of behavior correlated to the orientation angle of the fiber and pipe diameter (Figure 24). The failure modes of the GFRP/PVC pipes included cracking, fiber debonding, and fiber breakage.
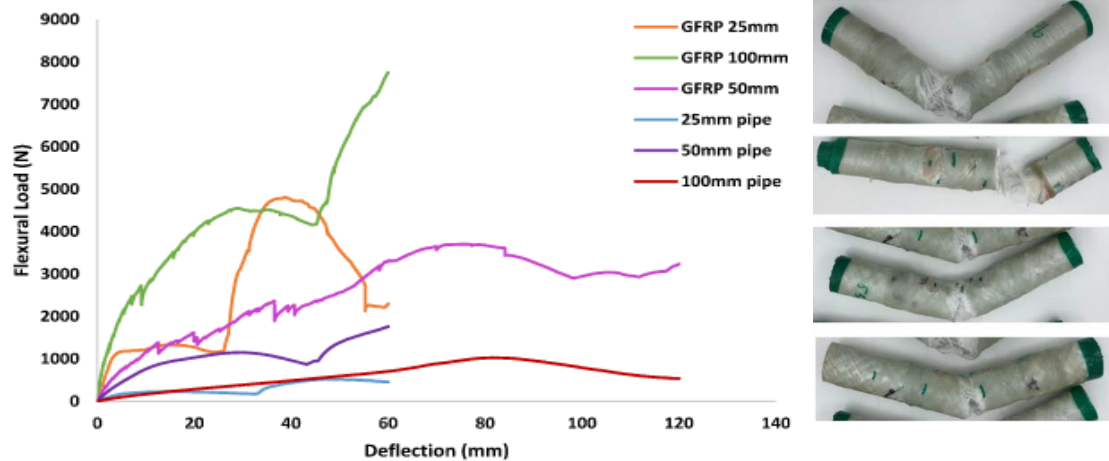
Figure 25. a- Summary of flexural load vs. deflection, b- GFRP overlapped plastic pipes [110].

Shi et al. evaluated the environmental impact of water supply pipes made of polyvinyl chloride (PVC) and bamboo winding composite using SimaPro software. Reporting the latter's environmental impact is less as nearly 500 times [41]. Also, the energy demand cumulatively was less by nearly three times and a half, and the environmental burdens were less by seven times. The Life Cycle Assessment (LSA) and Life Cycle Inventory (LSI) input data as functional units and system boundaries were collected by standard ISO 14040. Data on raw energy and raw materials were extracted from the Ecoinvent database in the used software. An investigation was carried out locally on bamboo, cotton textile, walnut husk, MUF resin, Styrene E, and bamboo fiber. Figure 26 shows the total environmental impact of PVC (hundred percent) and bamboo (percentage of PVC value).
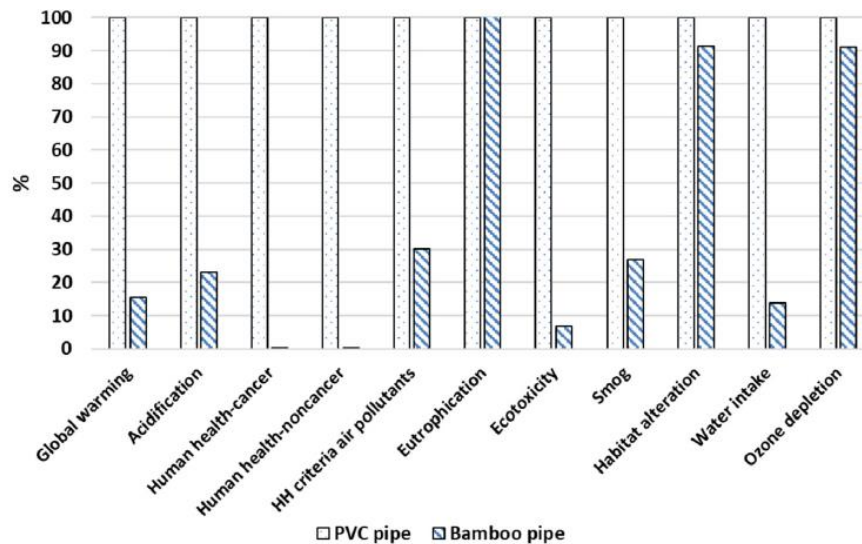
Figure 26. A comparison of the environmental impact of PVC pipe and bamboo pipe [41].

Affolter et al. investigated a failed water steel pipe with a glass fiber reinforced polymer in service for 12 years [111]. The drawing in Figure 27 shows two armored GFRP layers (2 and 6) combined with the stiffening core layer (4). The GFRP layers were made of randomly oriented chopped glass fibers and polyester resin, and the core layer was filled with silica sand. In contrast, the outer protective layer provided impermeability against corrosive species.

1) Protective coating
2) Outer armour (glass fibres, Polyester resin)
3) Transition layer (GFRP, quartz or silica sand)
4) Stiffening layer (Quarz sand, fibres, polyester)
5) Transition layer
6) Inner armour(glass fibres, Polyester resin)
7) Barrier coat
8) Pure resin layer inside
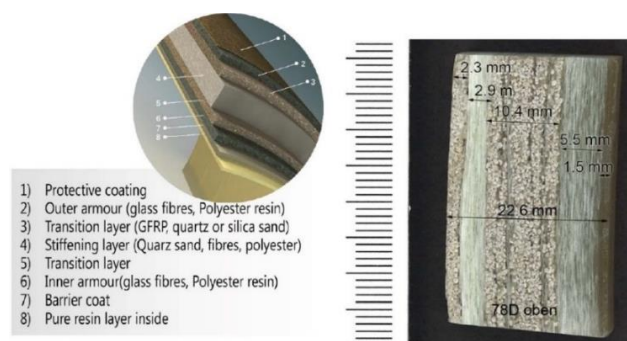
Figure 27. The typical lay-up of a pipe shell is manufactured with the centrifugal casting process (left), resulting in different layers with various reinforcements and filler materials (right: typical sample from a present pipe) [111].

The authors carried out 1) 3-point bending tests for determining bending moduli and

strength, 2) shear tests to determine interlaminar shear strength (ILSS), 3) tensile tests of entire cross-sections to determine tensile properties, 4) calcination methods for textile-glass and mineral-filler content, and 4) performance testing by ring compression. 20% loss of stiffness and up to 40% loss in strength was reported after 12 years of operation. There was partially incomplete backfilling between the composite and the steel surface, causing excessive local stresses. Dan-asabe *et al.* evaluated palm particulate (using compression molding) reinforced polyvinyl chloride (PVC) as a lightweight material for water pipes [40]. Density decreased, and elastic modulus increased with the weight fraction of the particulate reinforcement. Optimum strength of 50 MPa was at 8% of doum palm particulate, achieving 2 GPa elastic modulus, nearly 85 MPa flexural strength, and 1.45 g/cm^3 density. Pricewise, the composite was nearly 87% better compared to carbon steel and 36% compared to PVC. Figure 28 shows the variations of density, water absorption, flexural strength, and hardness with the weight fraction of the reinforcement against PVC (matrix) and Kankara clay (filler).
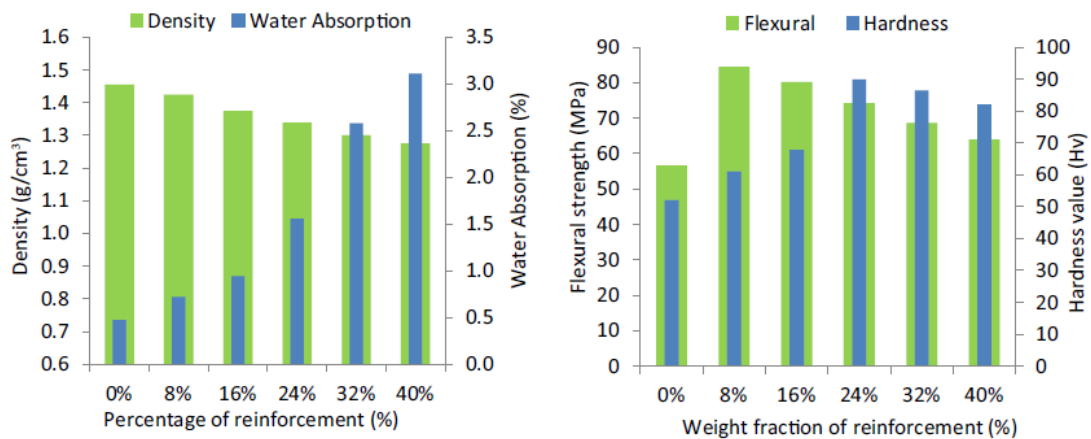
Figure 28. Variations of density, water absorption, flexural strength, and hardness with weight fraction [40].

Rafiee et al. investigated the progressive damage through the pipe wall thickness of Glass fiber Reinforced Polyester (GRP) pipes from water's internal pressure [112]. The

authors utilized a stochastic (random) approach to consider fiber volume fraction and winding angle as random uncertain parameters of defined convergence Monte-Carlo technique. Fiber volume fraction was found to be more significant than the winding angle on the failure pressure. In other work, Rafiee *et al*. correlated the failure of GRP pipes to the internal pressure of water pipes in a predictive model, based on micromechanics equations and failure criteria linked to experimental testing [113]. The parameters were fiber volume fraction and winding angle, against which failure pressures decreased and increased with, respectively. For the experiments, the pipes were placed in the testing machine, shown in Figure 29. After one week of curing, filled with pressurized water, and droplets were observed on the surface, at the average functional failure of 2.5 MPa with no evidence of failure in pipe structure.
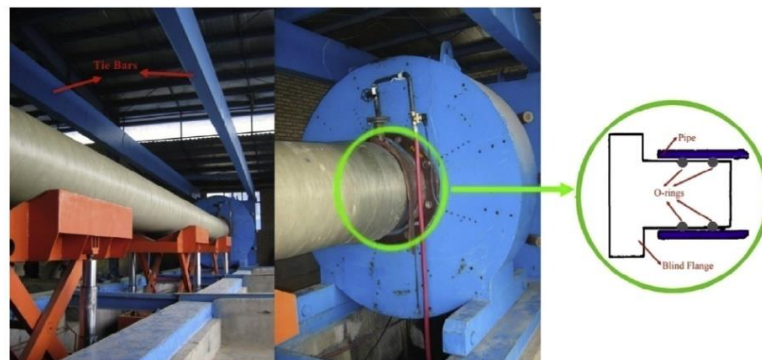
Figure 29. Hydrostatic pressure testing machine [113].

The variations (produced from FEA, using maximum stress and Hashin failure criteria, and material properties formulations as modified rule of mixture/Chamis and Halpin–Tsai) of first-ply failure pressure and functional failure pressure with fiber volume fractions are in Figure 30. First, ply failure was set as matrix cracking and the failure pressures predicted by the maximum stress criterion are higher than those of Hashin failure criteria.
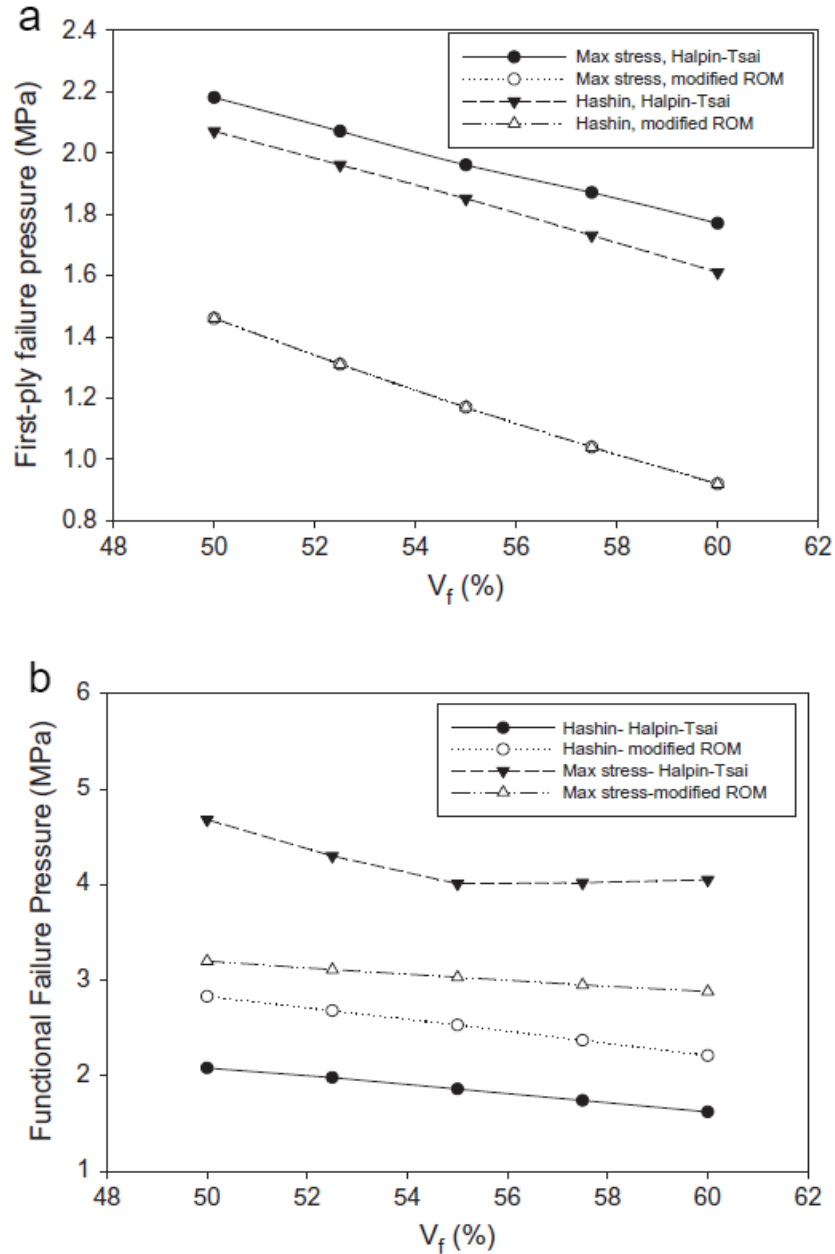
Figure 30. (a) First-ply failure pressure and (b) functional failure pressure for the investigated pipe versus fiber volume fraction V_f (%) [113].

Hu et al. evaluated the performance of prestressed concrete cylinder pipes (PCCP) with carbon fiber reinforced polymer (CFRP), applied at the inner surface, in Figure 31 (helpful in strengthening and repair purposes) [114]. The study was carried out with experimental testing and finite element analysis, together with failure risk analysis. With each additional CFRP layer, the threshold value for design pressure increased by

six broken wires (below damage limit), and that for working pressure by 20 broken wires.

Figure 31. Prepared CFRP-lined PCCP before assembly [114].

FRP was considered better than concrete to select in many sewer and drainage piping applications, as concrete is susceptible to failure due to H_2S attack on the pipe's upper surface. FRP is resistant to H_2S attack as a liner in large diameter sewage pipes made of concrete [115]. One example of a sewer concrete pipe repair by FRP liner was Los Angeles's case when an old sewer pipe showed failure. A new FRP liner repaired it (Figure 32). The reinforcement was a mixture of unidirectional glass fiber and other chopped elements. The inner layer was made of vinyl ester, and the core laminate and outer layer were made of unsaturated polyester [116].

Figure 32. The original concrete pipe while placing the FRP liner since much of its protective liner was missing [116].

Fiber is not added in general to sewer applications, unlike pressure pipes to make them

stronger. Remarkably few researchers handled the use of FRP for gravity sewer pipes. The available FRP pipes for sewer applications have Moderate pressure available sizes up to 72 inches, and it has the critical advantages of lightweight and no corrosion. Still, the critical disadvantage is the high cost compared to PVC and HDPE pipes [117].

2.4.2 Oil and Gas Pipelines

Most oil and gas transportations pipeline are metal pipes. The use of polymeric composites in repairing the steel pipes in the oil and gas industry is common practice, economic, and practical measure for corroded pipes [93]. Many researchers evaluated the effectiveness of such kind of repair for partially and severely corroded pipes. FRP material is common for offshore and onshore applications for high strength and corrosion resistance [9].

2.4.2.1 Onshore Pipelines

Onshore pipelines received most of the literature's attention concerning restoring strength after localized metal loss, considering FRP composites for their high-pressure capacity and durability. FRP has been investigated in characterization and failure pressure studies, mainly with the use of glass fibers and epoxy resin [10] [11] [12]. Composite materials proved reliable for repairing damaged pipes, increasing burst pressure, and reducing strain. Kakaei et al. [118] studied The effect of GFRP on reinforcing the buried and internally pressurized steel pipes against terrorist attacks. The explosive was TNT with 10 kg and a burial depth of 1 m from the ground level. The results show that reinforcing buried and internally pressurized pipes, in-depth to as much as 2.5 m, with GFRP, increased failure resistance and reduced maximum equivalent strain to nearly 35%. GFRP composites were reported to strengthen the welded steel pipes, as done by Alabtah et al., in reducing the effect of the heat-affected

zones on the pressure and deterioration capabilities of welded pipes with GFRP overwrap system using 5-axes filament-winding[6]. Carbon fiber and epoxy resins have been used to complete structural repairs and strengthen and rehabilitate onshore steel pipelines. Mahdi et al. studied the internal pressure behavior of repaired damaged metal pipes for onshore application by wrapping fabric carbon-epoxy systems at ±47° and 0°/90°orientations. The FRP layer was wrapped with a mechanism that allows the system to open and rotate during the damaged area's winding [119]. Pipes with ±47° orientation had higher internal pressure capacity than the hoop 90° wound pipe, observed to fail from axial strain in association to transverse stiffness, dominated by the matrix more than the fiber (Figure 33).
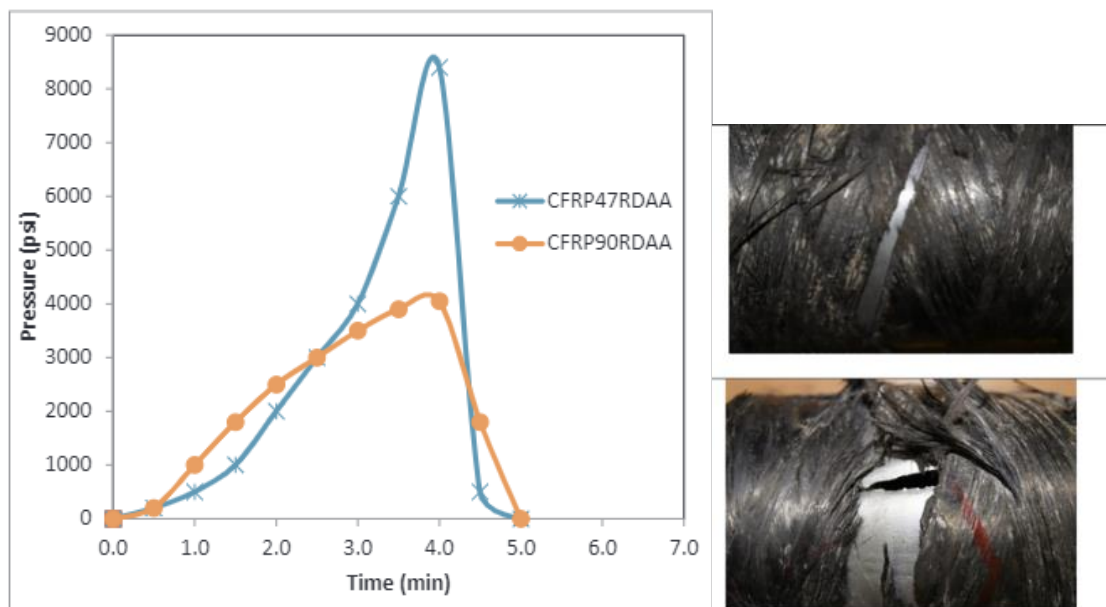
Figure 33. a- Burst mode of internally pressurized CFRP/metallic pipes, b- Effect of fabric orientation on the pressure capacity [119].

Another type of FRP pipe that is rarely used in the oil and gas industry is the flexible composite pipes. Flexible composite pipes have heat resistance less than metallic pipes, used at temperatures less than 90 °C [120]. Some thermoplastic resins could be used in the oil and gas industry as polyethylene matrix material, where it has a good record in

36

the oil and gas industry [30]. Not all pipes used in the oil industry are metallic pipes; some researchers mentioned using plastic pipes in the oil and gas industry. Zhang et al. [121] studied a corrosion-resistant plastic alloy composite pipe used in oil application. (Figure 34). The inner liner was polyvinyl chloride (PVC), and the outer layer consisted of glass fiber reinforced thermosetting resin, accommodating the circumferential pressure. The Vicat softening temperature (VST), and FTIR, T.G., and DSC analyses were used to study the failure mechanism. The additives that might not have been well distributed during extrusion and that might have been added beyond suitable amounts contributed to the failure process. Also, the outer GRP layer had weakened mechanical stability due to the degree of the resin curing used, causing lower glass transition temperature.
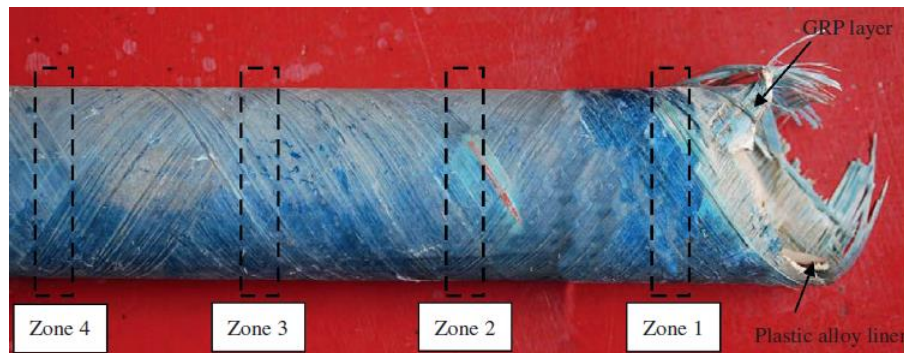
Figure 34. Failed anticorrosion plastic alloy composite pipe [121].

2.4.2.2 Offshore Pipelines

Since the 1970s, the feasibility and use of composite materials for offshore oil facilities in as deep as 1000 m applications have been assessed [122], especially regarding the performance at risers [123]. Studies have been developed to cover the physical/chemical interactions between the pipe steel and composite materials and the reinforcements for the damaged and corrupted risers [124][125][126][127]. To tackle corrosion in the offshore pipeline, an alternative solution to replacement is to

rehabilitate the pipe by adding FRP composite wraps to its exterior surface for the high strength/weight and modulus/weight ratios in the repair system [122]. Watanabe Junior et al. used the fiber-reinforced composite to repair and reinforce damaged pipes from localized corrosion in experimental performance evaluations [9]. They reported that FRP prevented leaking with pipe wall thickness damage as severe as 80% and with wall defects as deep as 50% of the diameter, with no bending. The use of glass fiber reinforced epoxy resins for repairing offshore pipes in Figure 35 was studied by Ahankariet et *al*. with hydrostatic and moisture absorption testing [128]. The hoop stress is repaired pipes after immersion in seawater for 40 days at 85ºC increased from nearly 289 to 358 MPa, but the strength decreased 43%, and the elastic modulus decreased 15%.
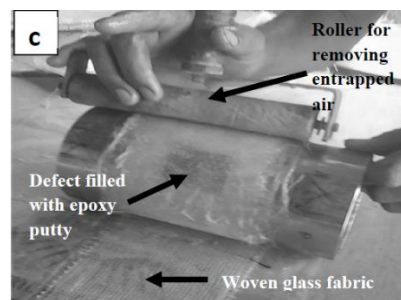
Figure 35. Rehabilitation of steel pipe [128].

Alexander et al. studied the feasibility of repairing offshore steel risers with carbon–fiber reinforced composites to sustain the combined loads of tension, bending, internal pressure, and external hydrostatic pressure [129]. The authors used E-glass in inner and outer reinforcement to protect against corrosion and protect against impacts and wear. Epoxy was applied to bond carbon half shells on the pipe's external surface, as shown in Figure 36, and burst pressure and four-point bending tests were carried out, indicating at reliability and safety of the composite repair system.

Figure 36. Installation of the carbon half-shells [129].

Aluminum pipes are also repaired using FRP material in offshore applications [130]. Some surface treatments should be introduced to increase the interface bonding between the aluminum pipe and the FRP. Boon et al. fabricated an aluminum/carbon pipe by wrapping three CFRP layers at ±55º to the axial direction and tested it under axial compression where grooves were cut on the aluminum liner in the same direction of the fiber. The grooving method was of specimens of higher maximum strength [131]. The growth of fatigue crack in aluminum pipe repaired with glass FRP epoxy was evaluated by Zarrinzadeh et al. [132]. They reported that the fatigue life increased significantly, and the stress intensity factor decreased.

2.4.3 Chemical Pipelines

Some FRP composites have great importance in the chemical industry as the use of glass–polyester pipes, where Stamenovic' et al. evaluated the chemical effects of pH of alkaline and acidic solutions on the longitudinal and circumferential tensile strengths of glass–polyester pipes at different exposure times at room temperature [133]. The pipes were made by filament winding at different reinforcement angles, and servohydraulic testing machines for flat and ring test specimens carried out the testing. The tensile strength and elastic modulus increased in the low-pH solutions, but they decreased in the high-pH solutions. Change in tensile strength was more than a change in modulus of elasticity, proportionally with duration of immersion in liquid. Cracking

progressed with an increase of load to result in fiber-matrix debonding, initiated from breaking fibers and ending in macro-cracks and delamination. Mahmoud et al. evaluated the change in glass fiber-polyester composite pipes' physical and mechanical properties after immersion in HCl, H_2SO_4, HNO_3, and H_3PO_4 100°C [134]. The results revealed that the glass-polyester pipes' material properties decrease with an increase of temperature and Sulfuric acid has the highest effect on the strength compared to other acids. Another research work conducted by Sindhu et al. [135] shows the influence of chemical aging on glass fiber/polyester composite. As shown in Figure 37, the fiber-matrix interaction enhanced by the aging treatment with acidic solutions, and the stress value was highest after 3-month aging.
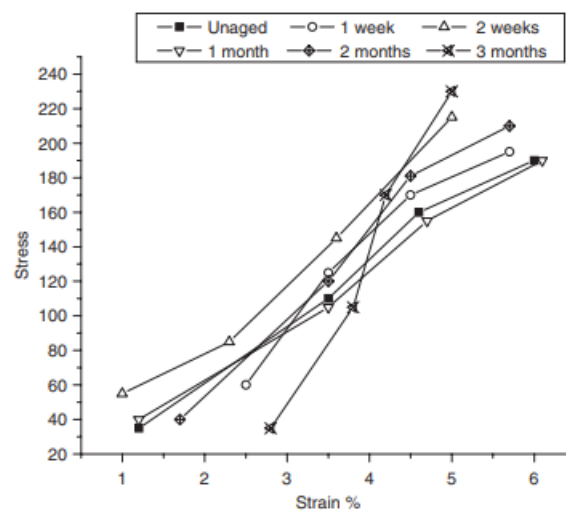
Figure 37. Stress-strain curves of glass fiber/polyester resin composites for different aging times in acidic medium [135].

Methacrylate epoxy fiber reinforced plastic (FRP) pipes are suitable for chemical applications and can be used for repairing. They are 35% less costly than standard epoxy pipes and can meet fire and explosion resistance requirements [136].

Table 2 summarizes the recent research, development, and practices of FRP composite in different pipeline applications worldwide, and they are classified according to the reinforcement and resin type used. All authors agreed on the advantages of using FRP composites in different pipeline applications. Fiber-reinforced composites have been the ideal material choice for the rehabilitation, development, and strengthening of conventional transportation pipelines because of their high strength, lightweight, stiffness, exceptional fatigue properties, and excellent corrosion resistance.

Table 2. summary for the recent research, development, and practices of FRP composite in different pipeline application

Fiber type	Resin type	year	Ref.	Pipeline application	Advantage of using FRP	Fabrication process	Type	Testing
Glass fiber	Polyester	2011	[133]	chemical pipelines	moderate behavior in acidic solution	Filament winding	Newly fabricated	Tensile test
	Polyester	2015	[112]	Water pipeline	Lightweight- good mechanical properties	Filament winding	Newly fabricated	hydrostatic test
	Polyester	2015	[113]	Water pipeline	Lightweight- good mechanical properties	Filament winding	Newly fabricated	hydrostatic test
	Polyester	2018	[111]	water feed steel pipe of a hydraulic power station	Strengthening and corrosion resistance	Composite tube	repair	Static fracture tests
	polyurethane resin	2017	[9]	offshore stainless-steel pipes	resistance to corrosion with good mechanical properties	Hand lay-up	repair	hydrostatic tests
	Epoxy	2013	[121]	oilfield plastic pipes	anticorrosion, thermal resistant, and high strength pipe	Filament winding	Newly fabricated	Fourier transform infrared spectroscopy

Fiber type	Resin type	year	Ref.	Pipeline application	Advantage of using FRP	Fabrication process	Type	Testing
Glass fiber	Epoxy	2016	[10]	Steel pipe with External metal loss	sustain the maximum possible pressure without failure	hand lay-up process	repair	Hydrostatic pressure tests
	Epoxy	2016	[117]	wastewater pipe	strengthening	Filament winding	Newly fabricated	
	Epoxy	2017	[132]	Aluminum pipe	strengthening	Wrapped by Repair patch	repair	tensile axial stress
	Epoxy	2018	[11]	Underground steel pipe	resist the bucket tooth penetration force	composite sleeve	repair	burst pressure loading
	Epoxy	2018	[100]	Steel gas pipeline	Good mechanical strength and resistance	composite sleeve	repair	uniaxial tensile tests
	Epoxy	2019	[12]	Oil and gas Steel pipe	restoring the loading capacity	composite wrap by wet lay-up process	repair	high burst pressure
	Epoxy	2020	[128]	underwater Steel pipe used for marine application	increase the strength and pressure capacity	Wrapping by wet lay-up	repair	high burst pressure

Fiber type	Resin type	year	Ref.	Pipeline application	Advantage of using FRP	Fabrication process	Type	Testing
Glass fiber	Epoxy	2020	[6]	Oil and gas steel pipes	Increase the strength of HAZ areas and corrosion resistance	Filament winding	Strengthening	Three- and four-point bending
	Epoxy	2020	[86]	Cracked steel pipe	Crack initiation pressure and serviceability increased.	Hand lay-up patch (numerical)	repair	cyclic loading
	Epoxy	2020	[110]	(PVC) pipelines for water and sewage transportation	strengthening	filament winding	Newly fabricated	four-point bending test
	Epoxy	2021	[118]	Buried oil and gas pipelines	reducing the deformation of buried pipes against explosions	Filament winding	Newly fabricated	Internal pressure and explosion
Carbon fiber	Epoxy	2001	[91]	Pressurized underground Carbon Steel pipes	improving the ultimate internal pressure capacity of pipes, and enhance the strength, Durability and corrosive properties.	wet lay-up	repair	soil load and internal pressure

Fiber type	Resin type	year	Ref.	Pipeline application	Advantage of using FRP	Fabrication process	Type	Testing
Carbon fiber	Epoxy	2010	[129]	Extending onshore pipeline to offshore steel risers	Strengthening and corrosion resistance	Pre cured layered system	repair	Burst pressure and 4point bending
	Epoxy	2017	[131]	Offshore oil and gas aluminum riser pipe.	very high performance besides being lightweight	filament winding	Newly fabricated	axial compression
	Epoxy	2018	[119]	oil and gas steel pipe	capability to carry high internal pressure	Smart repairing mechanisms allow the system to open and rotate.	repair	Internal pressure and corrosion
	Epoxy	2020	[28]	Steel pipes for petroleum and chemical industry	increase the strength and pressure capacity	Wrapping by wet lay-up	repair	high burst pressure
	Epoxy Grout	2021	[89]	Petroleum Steel pipes with a localized defect metal loss	Restore the capacity of the steel pipe with defects up to about 70% metal loss.	Standoff sleeve	repair	internal pressure test
Aramid fiber	Polyethylene Thermoplastic	2005	[30]	Onshore oil industry composite pipe	Strengthening and corrosion resistance	Prepreg	Repair	internal pressure test

Fiber type	Resin type	year	Ref.	Pipeline application	Advantage of using FRP	Fabrication process	Type	Testing
Aramid fiber	Polyolefin Resin	2015	[31]	Pe-rt Water pipeline	lightweight, ultra-high-strength, and high modulus pipe	----------	Newly fabricated	pipe water pressure blasting
	Epoxy	2019	[32]	Aluminum pipes for oil and gas process	new pipeline joining technique using FRP composites	hand lay-up	Joining and repair	three-point bending
Natural fibers	Kankara Clay	2018	[39]	(PVC) plastic pipelines for water and sewage transportation	low cost with an overall lightweight and good mechanical properties	Composite mold	Newly fabricated	Water absorption
	Kankara Clay	2018	[40]	(PVC) plastic pipelines for water and sewage transportation	low cost, lightweight, and good mechanical properties	Composite mold	Newly fabricated	Water absorption test and hardness
	Urea-Formaldehyde (Thermoset)	2019	[41]	water supply pipes	Better environmental impacts	high tension winding	Newly fabricated	Life cycle inventory

Fiber type	Resin type	year	Ref.	Pipeline application	Advantage of using FRP	Fabrication process	Type	Testing
Hybrid Fibers	Epoxy	2020	[52]	crude transportation carbon alloy steel pipe	burst pressure increased by 20% and reduced strain on the defective region	hand lay-up	repair	high burst pressure
	Epoxy	2020	[47]	cracked fluid transportation steel pipe in the offshore industry	Decreased the crack growth rate and prolonged the residual fatigue life.	Hand lay-up	repair	fatigue tests (four-point bending)
	Subsea epoxy	2021	[50]	Onshore and offshore steel pipe	improvement in the ultimate strength	Hand lay-up	repair	combination of axial compression and bending loads
	Epoxy	2021	[49]	offshore composite pipe	Strengthening and corrosion resistance	FEA	Newly fabricated	flexural loading (bending)
	Epoxy	2021	[48]	offshore composite pipe	Strengthening and corrosion resistance	FEA	Newly fabricated	3point bending

2.5 Limitations of the Existing FRP Technologies in Pipelines

Researchers have developed numerous techniques and material options. It was proved how corroded and damaged pipes restored their initial load-carrying capacity when they were repaired with composite material. It was observed that coating steel pipes with thin layers of FRP composites positively affects corrosion resistance properties and heat loss. Furthermore, it was noticed that strengthening plastic pipes through FRP composites increases the maximum allowable operating pressure significantly. The available literature on the use of fiber-reinforced composites in transportation pipelines can be applied effectively to develop the market and enhance the fluids transportation process with minimal pipe failure and cutouts. Nevertheless, certain repairing types involve the use of complex procedures. The half-shell sleeves repairing technique which requires a heavy-weight installation to join the sleeve creates another technical challenge that has not yet been explored enough to earn the confidence to be applied in different field applications. High tension wrapping processes as the filament winding cannot be installed at the site to repair or strengthen the conventional transportation pipes. There is a need for a robotic repairing system with high tension winding but in a portable design. Considerable research by other researchers has been carried out on FRP composite in oil and chemical pipelines. However, there is a need to investigate different polymeric matrices' behavior in different acidic solutions and concentrations to understand each matrix type's dissolving rate clearly. The dissolving of the polymeric matrix could lead to a significant degradation in the pipeline over time. Further studies on the joining of FRP pipes, interfacial properties between the FRP layers and the conventional pipe, load transfer mechanism between the FRP composite systems layers should be conducted to increase the confidence in expanding the market using this encouraging material system.

CHAPTER 3: THE EFFECT OF SIZING OPTIMIZATION ON THE INTERFACE BETWEEN

HIGH STRENGTH STEEL AND FIBER REINFORCED COMPOSITE

3.1 Introduction

Metal pipelines are the most effective pipes for oil and gas transportation. However, they are susceptible to corrosion in the harsh working environment [137][138]. Thus, many researchers have been motivated to find effective and safe alternatives for traditional steel pipes, which are light, cost-effective, and have corrosion resistance. Previous works have shown that metal-polymer hybrids pipes are the best alternatives for steel pipes [139]. The use of metal-polymer hybrids (MPHs) represents a viable solution for weight reduction, especially in the automotive industry, where emissions and fuel consumption in transports will be limited. Researchers have attributed using MPHs in the automotive industry to their optimum weight, high load-carrying capacity, and durability. Farahani et al. classified traditional fabricating metal-polymer hybrid components into two essential procedures [140]. The main benefits of MPHs are their exceptional lifetime, impact resistance, tolerance of damage, and flame resistance compared to conventional materials and fiber-reinforced plastics [140] [141]. MPHs cope with most of the metal and polymer materials limitations. Accordingly, aluminum alloys' low thermal properties and the brittle nature of composite materials can be either glass fiber, Kevlar fibers, or graphite fibers [142], [143]. Davidson et al. investigated the consequence of sequencing on the release rate of energy in composite materials. Researchers in this field have examined the energy release rates and deflections for multidirectional and unidirectional specimens using three-dimensional finite element analyses and classical laminated plate theory-based methods. They have shown that the classical plate theory-based methods could accurately calculate both the average mode ratio and

the total energy release rate [144]. De Baere et al. experimentally studied modes I and II of a carbon fabric reinforced polyphenylene sulfide using the DCB setup and End Notch Flexure (ENF) test, respectively. They have realized an unstable crack-growth for carbon fabric reinforced polyphenylene sulfide. Hence, Linear Elastic Fracture Mechanics was used to determine the toughness during the crack initiation stage. The Compliance-Based Beam Method was employed to predict the toughness during the propagation stages [145]. Mildner [146] conducted a comprehensive study of hybrid materials. Aluminum and steel specimens were bonded to the GFRP and CFRP laminated composites to examine the effect of fiber layup. The fabricated specimens were subjected to tensile and flexural tests. The stress-strain curve for the tested specimens similarly exhibited a nonlinear behavior. Specimens with 0° fiber orientations outpaced all-steel specimens and scored the highest strength. Zhang et al. studied the failure behavior and the mechanical properties of steel/PA66 composite hybrids fabricated using injection molding technique. They subjected the prepared specimens to tensile bending loading to characterize their modes I and II fracture loads. Interface properties among steel and composite were tested using end notched flexure tests and a double cantilever beam. They stated that the multiple cracks start at the midplane surface between the steel and PA66 and lead to the complete failure [14]. Liu et al. studied the mode-I fracture toughness of interlaminar interfaces with different fiber orientation angles for T800/epoxy composite specimens using experimental technique and finite element analysis. They used the data reduction scheme established on the modified beam theory to determine the mode-I fracture toughness. They demonstrated that curved laminated composite had higher mode-I fracture toughness than straight laminated composites [147]. Delamination or interlaminar failure is a critical failure mechanism and one of the most common damages in

laminated composite materials [148], [149]. Overall, delamination may happen under three modes. These consist of the opening mode (mode I), the sliding shear mode (mode II), and the scissoring shear mode (mode III)[150] [151]. Many researchers had already studied the interlaminar failure in fiber-reinforced composites. Nevertheless, it is still an active research topic since new polymers with improved mechanical properties are established daily for fiber-reinforced composites. The materials' bonding properties depend on surface roughness and surface treatment. Many processes can be employed, including; plasma exposure, mechanical abrasion, and chemical etching [152] [143]. However, within this study, the effect of these processes on the interlaminar fracture toughness will not be considered, and the steel sheets and FRP layers will be bonded together with adhesive only without any pre-treatments other than using the sandpaper. These research results will be considered for pipeline applications. Based on the author's knowledge, most of the work in metal fiber laminates is focused on aerospace applications, and very few papers are considering the pipeline application. This paper investigates the effect of fiber type and fiber orientation on the mode I and mode II inter-laminar fracture toughness of Steel/FRP laminates, and results are presented from an experimental investigation.

3.2 Materials and Methods

3.2.1 Materials

EN10130 steel sheet with a 1.5 mm thickness was used. For fiber type's effect on the interface between steel and FRP composites, three different types of (0°/90°) woven fabrics were utilized, namely woven glass, carbon, and Kevlar fabric, as shown in Figure 38. The EL2 epoxy resin and AT30 Slow-Hardener with a density of 1.14 g/cm^3 were used as the polymeric matrix. Table 3

lists the elastic constants of the employed composites.

(a) (b) (c)
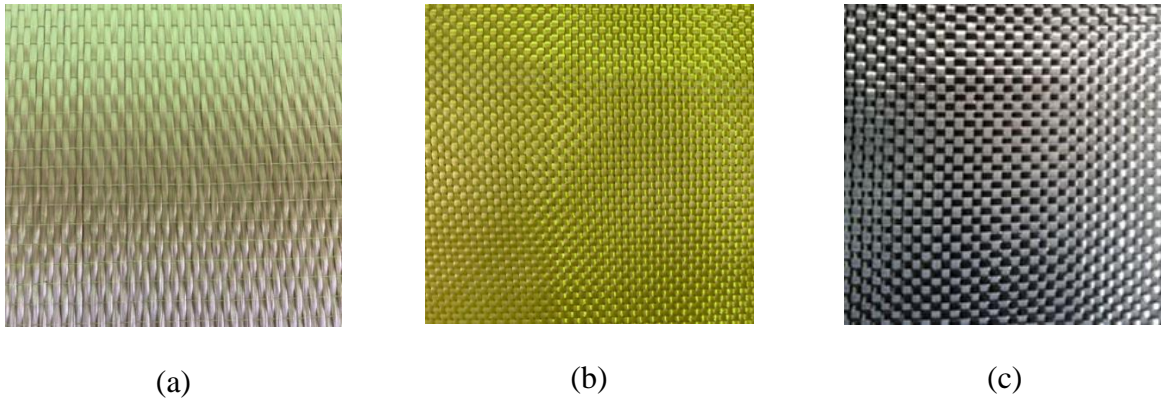
Figure 38. (a) Woven E-Glass fabric, (b) Woven Kevlar fabric, (c) Woven carbon fabric.

Table 3. Elastic constants properties for GFRP, KFRP, and CFRP composites.

	E_{11}	E_{22}	G_{12}	G_{23}	G_{13}	v_{12}	v_{23}	v_{13}
	(GPa)	(GPa)	(GPa)	(GPa)	(GPa)			
E-Glass/Epoxy	24.5	23.8	4.7	3.6	0.11	0.20	0.15	2.6
Carbon/Epoxy	77	75	6.5	4.1	0.06	0.37	0.50	5.1
Kevlar/Epoxy	29	29	18	1.8	0.05	0.11	0.05	2.2
Steel	217		82			0.28		

3.2.2 Fabrication process

In this study, the hybrid material systems consist of sheet metal and glass, Kevlar, or carbon fiber-reinforced polymer. The steel sheets and FRP are bonded to each other. According to the ASTM D5528 standard, laminates need to have an even number of plies and shall be unidirectional, with delamination growth happening in the 0° direction. Therefore, the number of layers used in the

FRP phase was 14 layers for the case of CFRP and 10 and 8 layers for GFRP and KFRP, respectively, so all the FRP layers will have a total thickness of 1.5mm. For the effect of fiber orientation on the interface between steel and FRP, seven different woven glass fabric orientations were examined as follows: 0°, 15°, 30°, 45°, 60°, 75°, and 90°. The steel sheets were cut into 20 mm × 150 mm panels, and the exact specimen dimensions were used for both DCB and ENF tests, as shown in Figure 39.

(a)

(b)
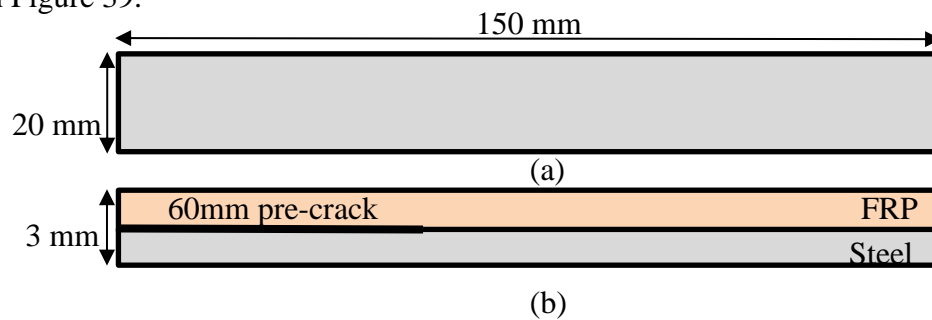
Figure 39. Dimension of the DCB and ENF test specimens, a-top view, b- side view.

According to ASTM D5528 and ASTMD7905 standards, a non-adhesive insert shall be introduced at the mid-plane of the steel/FRP hybrid laminate during layup to form an initiation site for the delamination, and a thin film made of polytetrafluoroethylene (PTFE) is recommended. Steel/FRP hybrid laminates with different fabric types and orientations tested for mode I and II were fabricated utilizing a vacuum-assisted resin transfer molding machine (Figure 40). This technique produces parts with almost no cavities and air bubbles. In this process, the vacuum bag assists the continuous flow of low-pressure infused resin from one side to the other. It also offers the benefit of not requiring an expensive autoclave. When the epoxy resin was infused into the fabric, the steel/FRP parts could cure at room temperature. Figure 41 shows a PTFE Teflon sheet of a 0.01 mm thick layer was inserted in the middle of the polymer-metal interface to simulate the pre-crack. A pair of piano hinge tabs were bonded to the end of each specimen that will be tested

for mode I to connect them to the loading arm during the test, as shown in Figure 41 and Figure 42.
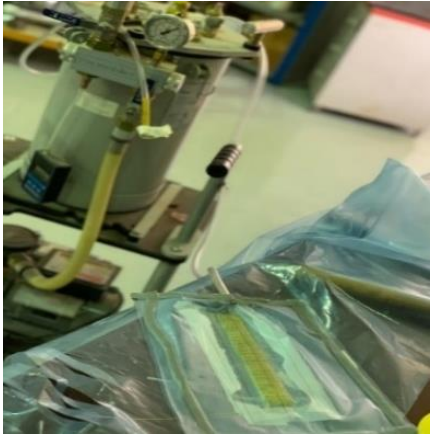
Figure 40. Vacuum-assisted resin transfer molding.

GFRP   KFRP   CFRP   Specimens with PTFE Teflon sheet
                                                                         and hinges

Figure 41. GFRP, KFRP, and CFRP specimens for mode I test.

Figure 42. Specimens with different fiber orientation angles for mode I test.

3.2.3 Laminate Stiffness

The interface bonding of composite materials is highly dependent on the laminate stiffness. Therefore, the classical lamination theory is utilized to define the relationship between resultant forces, resultant moments, mid-surface strains, and curvature as follows:

$$\begin{Bmatrix} N \\ M \end{Bmatrix} = \begin{bmatrix} A & B \\ B & D \end{bmatrix} \begin{Bmatrix} \varepsilon^0 \\ k \end{Bmatrix} \tag{1}$$

Where: $A_{ij} = \sum_{k=1}^{N}\left[\bar{Q}_{ij}\right]_k (z_k - z_{k-1})$ (2)

$B_{ij} = \frac{1}{2}\sum_{k=1}^{N}\left[\bar{Q}_{ij}\right]_k (z_k{}^2 - z_{k-1}{}^2)$ (3)

$D_{ij} = \frac{1}{3}\sum_{k=1}^{N}\left[\bar{Q}_{ij}\right]_k (z_k{}^3 - z_{k-1}{}^3)$ (4)

Where:

[A] is the extensional-stiffness matrix,

[B] is the extension-bending coupling matrix,

[D] is the bending-stiffness matrix, i and j are the matrix notation, z_k is the distance from the mid surface to the top of layer k, $\{N\}$is the resultant laminate forces,

$\{M\}$ is the resultant moment $\{\varepsilon^0\}$ is the mid-surface strains,

$\{ k \}$is the curvature, and [Q] is the stiffness matrix.

Table 4 gives the values [A], [B], and [D] matrices. At the beginning of the mode I test, the in-plane extension-stiffness matrix plays a significant role until reaching the critical force. Then, of plane extension-stiffness matrix takes over the propagation period, and it can be calculated using

the following relations.

$$\begin{Bmatrix} Q_x \\ Q_y \end{Bmatrix} = \begin{bmatrix} A_{55} & A_{45} \\ A_{45} & A_{44} \end{bmatrix}_k \begin{Bmatrix} \gamma_{xz} \\ \gamma_{yz} \end{Bmatrix}_k \qquad (5)$$

Where: $A_{ij} = c \sum_{k=1}^{N} [\bar{Q}_{ij}]_k \left\{ (z_k - z_{k-1}) - \frac{4}{3h^2}(z_k{}^3 - z_{k-1}{}^3) \right\} \qquad (6)$

Where i,j= 4,5, γ_{xz} and γ_{yz} are out of plane shear strains, Q_x and Q_y are the out of plane shear

forces, c is the shear correction factor, and for a rectangular section, c=6/5 (1.2), and the total

laminate thickness (h) is 3mm [23]. The out of plane extension-stiffness matrix A_{44}, A_{55} and A_{45}

values for each of the prepared specimens are recorded in

Table 5. They were calculated using the following relations.

$$Q_{44} = G_{23}; \quad \overline{Q_{44}} = Q_{44}m^2 + Q_{55}n^2 \qquad (7)$$

$$Q_{55} = G_{13}; \quad \overline{Q_{55}} = Q_{55}m^2 + Q_{44}n^2 \qquad (8)$$

And, $\overline{Q_{45}} = (Q_{55} - Q_{44})mn \qquad (9)$

Where: m=cosθ, and n=sinθ, and θ is the orientation angle.

Table 4. Longitudinal stiffness matrix [A] for each prepared specimen.

Specimens	In-plane Longitudinal stiffness matrix [A] $\times 10^8$(N/m)	Extension-bending coupling matrix [B] $\times 10^4$ (N)	Bending-stiffness matrix [D] $\times 10^1$ (N.m)
CFRP 0°/Steel	$\begin{bmatrix} 4.744 & 1.136 & 0.000 \\ 1.136 & 4.713 & 0.000 \\ 0.000e & 0.000 & 1.348 \end{bmatrix}$	$\begin{bmatrix} 18.20 & 7.674 & 0.000 \\ 7.674 & 18.44 & 0.000 \\ 0.000 & 0.000 & 8.838 \end{bmatrix}$	$\begin{bmatrix} 37.51 & 8.978 & 0.000 \\ 8.978 & 37.26 & 0.000 \\ 0.000 & 0.000 & 10.66 \end{bmatrix}$
KFRP 0°/Steel	$\begin{bmatrix} 3.950 & 1.074 & 0.000 \\ 1.074 & 3.950 & 0.000 \\ 0.000 & 0.000 & 1.505 \end{bmatrix}$	$\begin{bmatrix} 23.30 & 7.830 & 0.000 \\ 7.830 & 23.30 & 0.000 \\ 0.000 & 0.000 & 7.281 \end{bmatrix}$	$\begin{bmatrix} 30.42 & 8.274 & 0.000 \\ 8.274 & 30.42 & 0.000 \\ 0.000 & 0.000 & 11.59 \end{bmatrix}$
GFRP 0°/Steel	$\begin{bmatrix} 3.833 & 1.078 & 0.000 \\ 1.078 & 3.823 & 0.000 \\ 0.000 & 0.000 & 1.286 \end{bmatrix}$	$\begin{bmatrix} 23.17 & 7.490 & 0.000 \\ 7.490 & 23.25 & 0.000 \\ 0.000 & 0.000 & 8.587 \end{bmatrix}$	$\begin{bmatrix} 28.75 & 8.086 & 0.000 \\ 8.086 & 28.67 & 0.000 \\ 0.000 & 0.000 & 9.645 \end{bmatrix}$
GFRP 15°/Steel	$\begin{bmatrix} 3.810 & 1.100 & 0.03988 \\ 1.100 & 3.801 & -0.03721 \\ 0.03988 & -0.03721 & 1.308 \end{bmatrix}$	$\begin{bmatrix} 23.36 & 7.30 & -0.3245 \\ 7.30 & 23.43 & 0.3045 \\ -0.3245 & 0.3045 & 8.406 \end{bmatrix}$	$\begin{bmatrix} 28.58 & 8.253 & 2.991 \\ 8.253 & 28.51 & -2.791 \\ 2.991 & -2.791 & 9.812 \end{bmatrix}$
GFRP 30°/Steel	$\begin{bmatrix} 3.764 & 1.145 & 0.04085 \\ 1.145 & 3.759 & -0.03623 \\ 0.04085 & -0.03623 & 1.353 \end{bmatrix}$	$\begin{bmatrix} 23.74 & 6.946 & -0.3318 \\ 6.946 & 23.78 & 0.2971 \\ -0.3318 & 0.2971 & 8.042 \end{bmatrix}$	$\begin{bmatrix} 28.23 & 8.587 & 3.064 \\ 8.587 & 28.19 & -2.717 \\ 3.064 & -2.717 & 10.15 \end{bmatrix}$
GFRP 45°/Steel	$\begin{bmatrix} 3.739 & 1.167 & 0.002668 \\ 1.167 & 3.739 & 0.002668 \\ 0.002668 & 0.002668 & 1.375 \end{bmatrix}$	$\begin{bmatrix} 23.94 & 6.764 & -0.02001 \\ 6.764 & 23.94 & -0.02001 \\ -0.02001 & -0.02001 & 7.861 \end{bmatrix}$	$\begin{bmatrix} 28.04 & 8.754 & 2.001 \\ 8.754 & 28.04 & 2.001 \\ 2.001 & 2.001 & 10.31 \end{bmatrix}$

57

Specimens	In-plane Longitudinal stiffness matrix [A] $\times 10^8$ (N/m)			Extension-bending coupling matrix [B] $\times 10^4$ (N)			Bending-stiffness matrix [D] $\times 10^1$ (N.m)		
GFRP 60°/Steel	$\begin{bmatrix} 3.759 & 1.145 & -0.03623 \\ 1.145 & 3.764 & 0.04085 \\ -0.03623 & 0.04085 & 1.353 \end{bmatrix}$			$\begin{bmatrix} 23.78 & 6.946 & 0.2971 \\ 6.946 & 23.74 & -0.3318 \\ 0.2971 & -0.3318 & 8.042 \end{bmatrix}$			$\begin{bmatrix} 28.19 & 8.587 & -2.717 \\ 8.587 & 28.23 & 3.064 \\ -2.717 & 3.064 & 10.15 \end{bmatrix}$		
GFRP 75°/Steel	$\begin{bmatrix} 3.801 & 1.100 & -0.03721 \\ 1.100 & 3.810 & 0.03988 \\ -0.03721 & 0.03988 & 1.308 \end{bmatrix}$			$\begin{bmatrix} 23.43 & 7.309 & 0.3045 \\ 7.309 & 23.36 & -0.3245 \\ 0.3045 & -0.3245 & 8.406 \end{bmatrix}$			$\begin{bmatrix} 28.51 & 8.253 & -2.791 \\ 8.253 & 28.58 & 2.991 \\ -2.791 & 2.991 & 9.812 \end{bmatrix}$		
GFRP 90°/Steel	$\begin{bmatrix} 3.823 & 1.078 & 0.000 \\ 1.078 & 3.833 & 0.000 \\ 0.000 & 0.000 & 1.286 \end{bmatrix}$			$\begin{bmatrix} 23.25 & 7.490 & 0.000 \\ 7.490 & 23.17 & 0.000 \\ 0.000 & 0.000 & 8.587 \end{bmatrix}$			$\begin{bmatrix} 28.67 & 8.086 & 0.000 \\ 8.086 & 28.75 & 0.000 \\ 0.000 & 0.000 & 9.645 \end{bmatrix}$		

Table 5. A_{44}, A_{55} and A_{45} values for each of the prepared specimens.

Specimens	$A_{44} \times \times 10^6$ (N/m)	$A_{55} \times 10^6$ N/m)	$A_{45} \times 10^6$ (N/m)
Fiber type			
CFRP 0°/Steel	7.57	9.42	0
KFRP 0°/Steel	3.69	4.51	0

Specimens	$A_{44} \times \times 10^6$ (N/m)	$A_{55} \times 10^6$ N/m)	$A_{45} \times 10^6$ (N/m)
GFRP 0°/Steel	6.47	4.67	0
Fiber Orientation			
GFRP 0°/Steel	6.47	4.67	0
GFRP 15°/Steel	6.35	4.80	-0.40
GFRP 30°/Steel	6.02	5.12	-0.40
GFRP 45°/Steel	5.57	5.57	0
GFRP 60°/Steel	5.12	6.02	0.40
GFRP 75°/Steel	4.80	6.35	0.40
GFRP 90°/Steel	4.67	3.2	0

3.2.4 Testing Procedures

Effects of fiber orientation and fiber type on the interface bonding between steel and fiber-reinforced composite were examined, and the fracture loads for modes I and II were computed. Double cantilever beam (DBC) and end-notched flexure (ENF) tests were applied to characterize mode I and mode II interlaminar fracture toughness, respectively. The unidirectional woven fabric laminates consist of 10 and 8 layers for GFRP and KFRP, respectively, and 14 layers for carbon fiber.

3.2.4.1 Double Cantilever Beam (DCB) Test

A double cantilever beam (DCB) test was applied to characterize mode I, the crack-opening mode, in which the delamination faces open away from each other. Figure 42 shows a schematic illustration of the DCB sample of steel/composite hybrids. During the test, the crack progress and the initiated forces leading to delamination are measured.
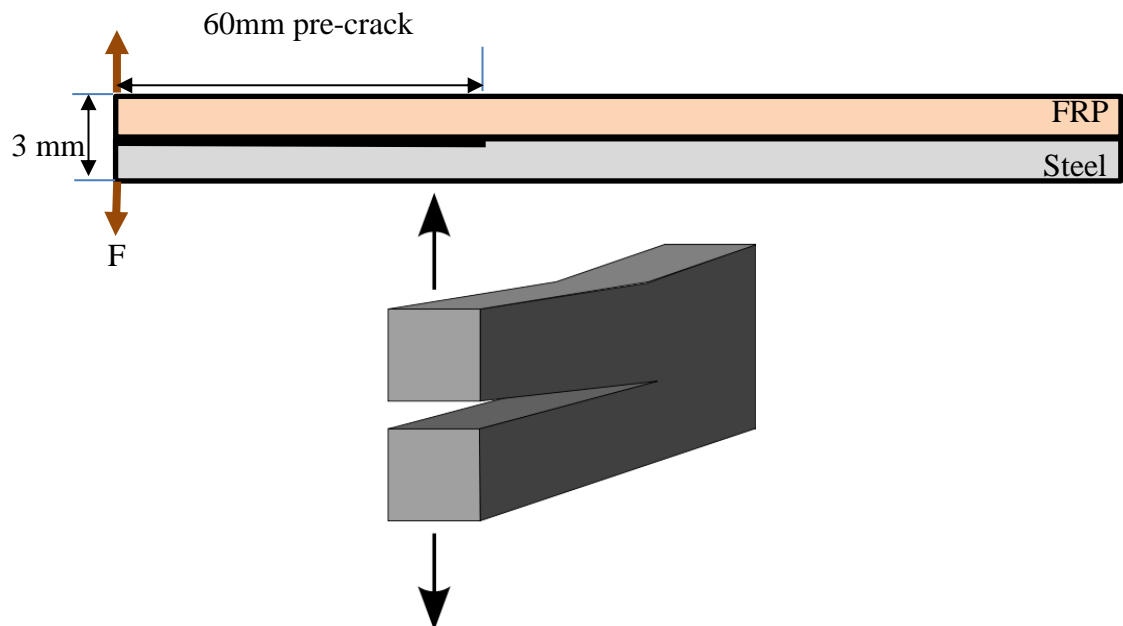
Figure 43. Schematic illustration of the DCB sample of steel/composite hybrids.

Three identical specimens were tested from each fiber type and fiber orientation to assure that the results are reliable. The load was subjected vertically to the crack plane utilizing an INSTRON universal materials testing machine. The crosshead was moving at a speed of 2.5 mm/min. Cracks initiated in a stable mode, followed by some fluctuations and cracking in the matrix. The optical crack length measurement method was applied during the test, where high-quality videos were recorded for the entire test to assist the optical crack length measurement. The strain energy release rate (G_C) is the energy lost in the test specimens per unit of sample width for a tiny increase in delamination length for delamination growing self-similarly under a stable displacement. It is the best material property that represents the resistance to delamination. Figure 43 shows the DCB sample, including the application of force and the crack opening progress.
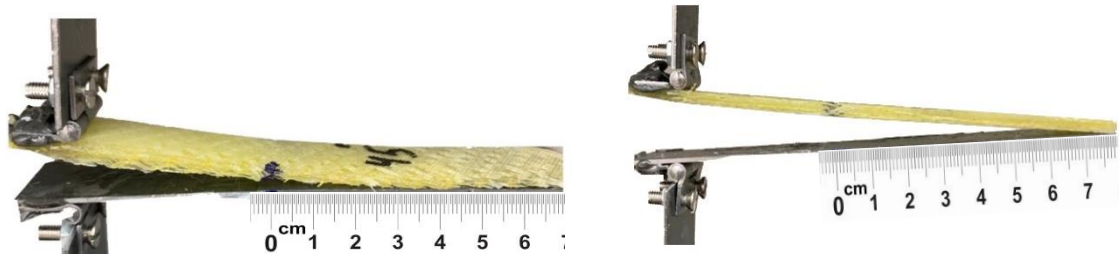
Figure 44. Crack opening progress for the DCB test.

The rate of G_{IC} can be determined using the Modified beam theory based on ASTM D5528, as shown in the following equation.

$$G_{IC} = \frac{3F\delta}{2ba}$$
(10)

Where: a is the crack progress length [m]

b is the sample width [m]

F is the critical load at [N]

δ is the corresponding displacement [m]

3.2.4.2 End Notched Flexure (ENF) Test

The FRP/steel specimens were loaded by shear forces in the crack initiation zone to define the energy release rate G_{IIC} under the load according to mode II. The specimens were exposed to a 3-point bending load condition until crack propagation. The ENF test enables the shear loading of the pre-cracked specimen by compressing the mid-span of the assembly, where the shear stress is always maximum at the mid-plane, which is the location of the pre-crack in the tested specimens. Figure 44 shows a schematic illustration of the ENF set of steel/composite hybrids.
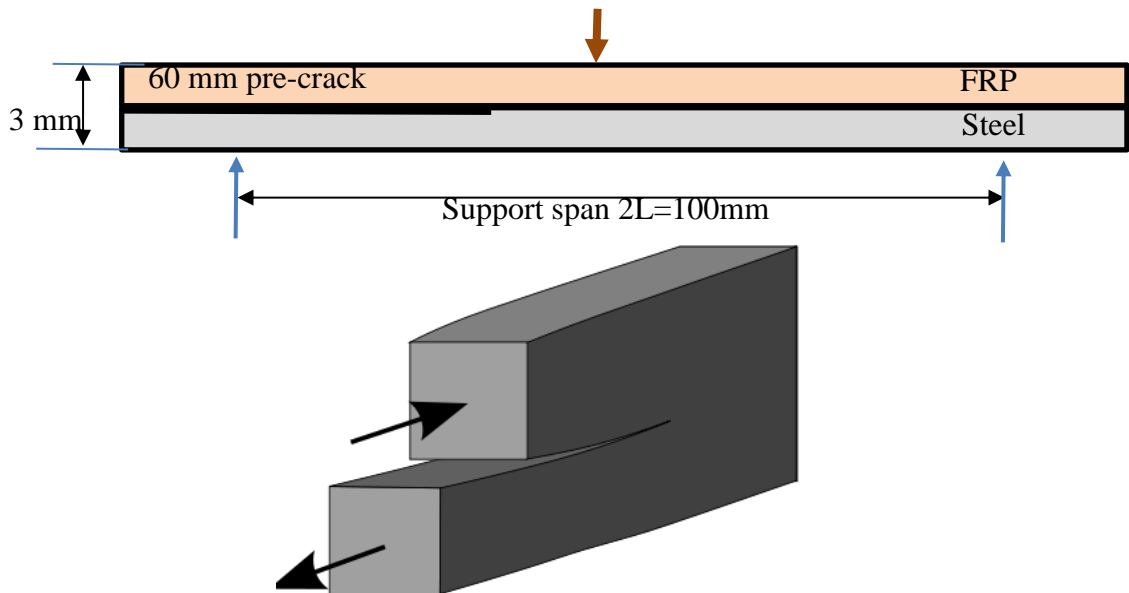
Figure 45. Schematic illustration of the ENF set of steel/composite hybrids.

The load was applied to the specimens at a constant crosshead rate of 1.5 mm/min, where the applied displacement generated shear mode loading at the crack front. The crack length was measured similarly as in DCB tests using the optical measurement method. Figure 46 shows the ENF sample, including force and the Bending progress. According to ASTMD7905, one can determine the energy release rate G_{IIC} using Equation 11.

$$G_{IIC} = \frac{9F\delta a^2}{2b(2L^3 + 3a^3)}$$ (11)

Where: $2L$ is the span length.
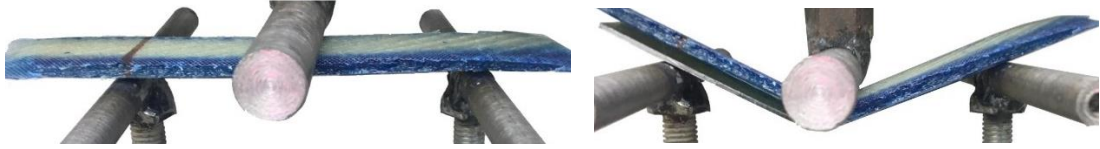
Figure 46. Bending progress for the ENF test.

According to ASTMD7905, the cylindrical loading surface must have a radius, r_1, in the range of 4.7 to 9.6 mm. A steel cylinder with a radius of 8mm was used for loading. The cylindrical supporting surfaces shall have the same radius, r_2, which shall be in the range of 3.0 to 6.4 mm. So, steel cylinders with a radius of 5mm were used as the supports. The loading surface shall be centered between the two supporting surfaces.

3.3 Results and Discussion

3.3.1 Interface Properties

3.3.1.1 Double Cantilever Beam (DCB) Test (Mode I)

The DCB fracture test's load-extension curves for the FRP/steel specimens with different fabric types are presented in Figure 47. The average of each three identical specimens is plotted in the graph. It could be observed that all the specimens have almost the same behavior. The curves show that the specimens have a linear behavior until the critical force values were reached. Those force values were used to determine the initial interlaminar fracture toughness using Equation 10. After which, the curves showed a stable behavior with minimal fluctuations. These fluctuations are caused by fracture resistance and are associated with decreased strength. CFRP part handled the highest force value, by around 420 N, followed by KFRP parts and the GFRP parts.
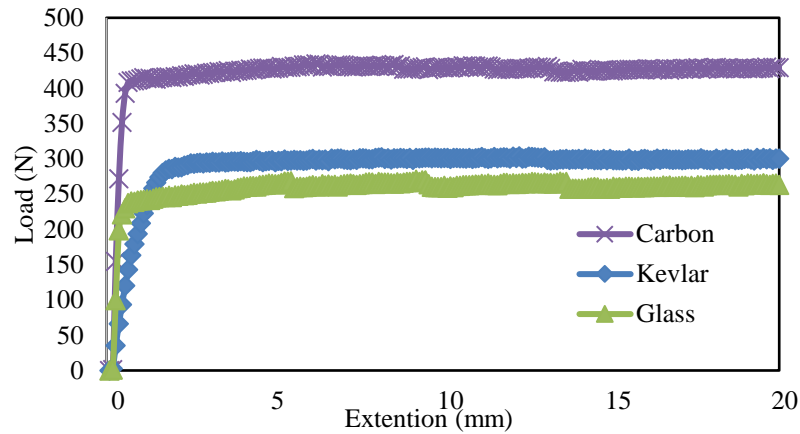
Figure 47. Force-displacement curves of the DCB specimens with different fabric types.

Table 6 shows the effect of using different fabric types on mode I interlaminar fracture toughness G_{IC}. The average values for different fabric types were presented with the coefficient of variation (CoV), which is the standard deviation ratio to the mean. Three identical specimens were tested for each fabric orientation, and the recorded G_{IC} values for each group indicated that the test results are reliable where the force-displacement curves of the identical specimens were overlapping each other well.

It was shown that the specimens made of Steel-CFRP were the specimens that had the highest fracture toughness, where G_{IC} initial and propagation values reached more than 395 and 7800 J/m^2 respectively. This finding is due to the high bonding strength in Steel-CFRP specimens. It was proved from the calculations in Table 4 that the Steel-CFRP specimens have the highest A_{11} values, followed by the Kevlar and then glass fibers, which supports the experimental results. Figure 48 shows a comparison between the initial and propagation fracture toughness for specimens with different fabric types.

Table 6. Mode I interlaminar fracture toughness G_{IC} for different fabric types.

Fabric Type	G_{IC} initial value [J/m^2]	G_{IC} propagation value [J/m^2]
CFRP	395.35± 1.44%	7875.56± 1.67%
KFRP	369.45± 1.11%	5625.42± 1.24%
GFRP	177.75± 1.98%	4856.25± 1.85%
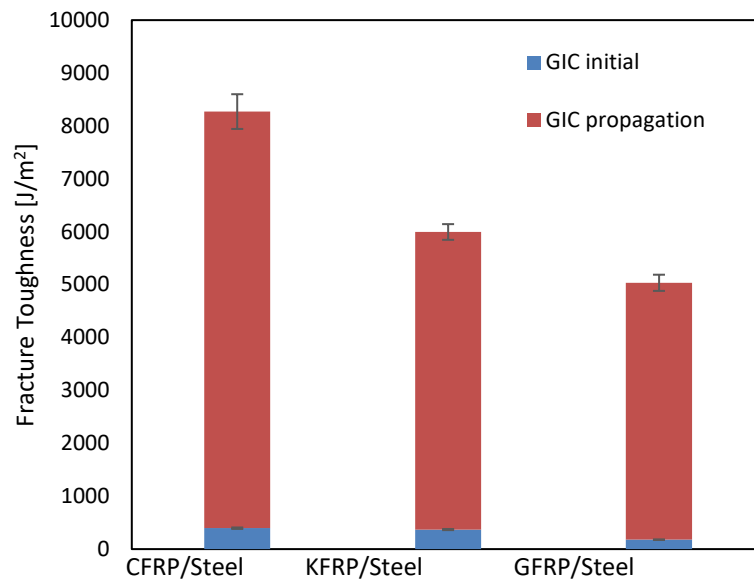
Figure 48. Mode I's initial and propagation fracture toughness for specimens with different fabric types.

Figure 49 shows the DCB fracture test's load-extension curves for the GFRP/steel specimens with different fabric orientations. It can be seen from the graph that before the onset of delamination growth, the load increases linearly with applied displacement. Upon reaching the critical force point, which differs from one specimen to another, the load rises slowly as the crack progresses, demonstrating that long path crack propagation occurs. Specimens with 0° fiber orientation reached the highest forces values (around 270 N).
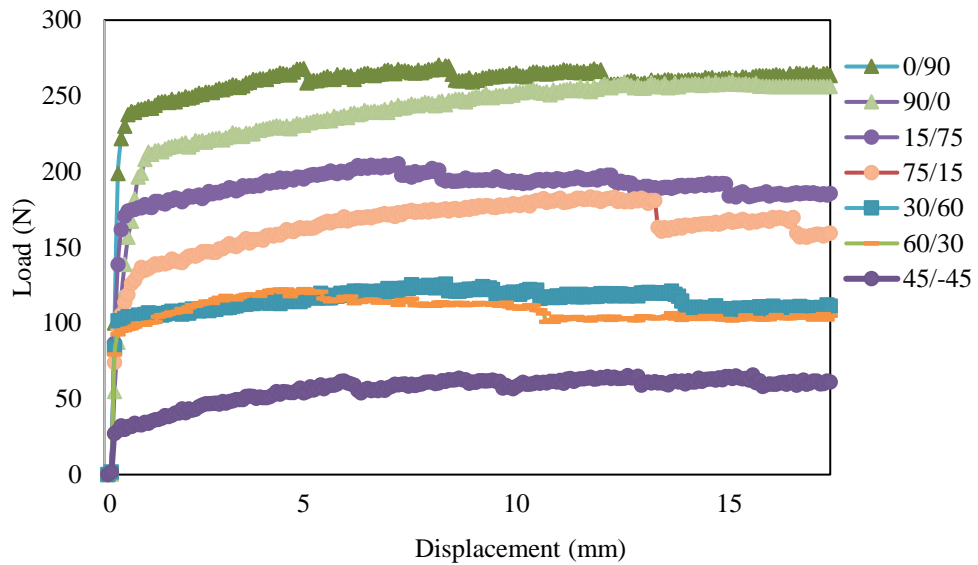
Figure 49. Force-displacement curves of DCB specimens with different fabric orientations.

Table 7 demonstrates the effect of using different fabric orientation angles on mode I interlaminar fracture toughness G_{IC} of the mode I fracture specimens. Mode I interlaminar fracture toughness G_{IC} average values for different fabric orientation angles were computed and presented with CoV.

Three identical specimens were tested for each fabric orientation, and the recorded G_{IC} Values for each group indicated that the test results are reliable. It shows that the specimens with 0° fabric orientation were the specimens that had the highest fracture toughness where the initial and propagation fracture toughness values reached more than 177 and 4850 J/m², respectively. This finding shows that using a 0° fabric orientation results in high bond strength of Steel/GFRP specimens. Figure 50 shows a comparison between the mode I initial and propagation fracture toughness for specimens with different fabric orientations.

Table 7. Mode I interlaminar fracture toughness G_{IC} for different fabric orientations.

	G_{IC} initial value [J/m^2]	G_{IC} propagation value [J/m^2]
0°	177.75± 1.98%	4856.25± 1.85%
15°	139.62± 2.31%	3562.53±2.24%
30°	54.10± 5.35%	2137.52±4.89%
45°	8.67± 4.19%	1050.43±3.68%
60°	50.35± 1.94%	2043.75±1.73%
75°	129.75± 2.20%	3112.51±2.51%
90°	172.28± 1.24%	4537.50±1.36%
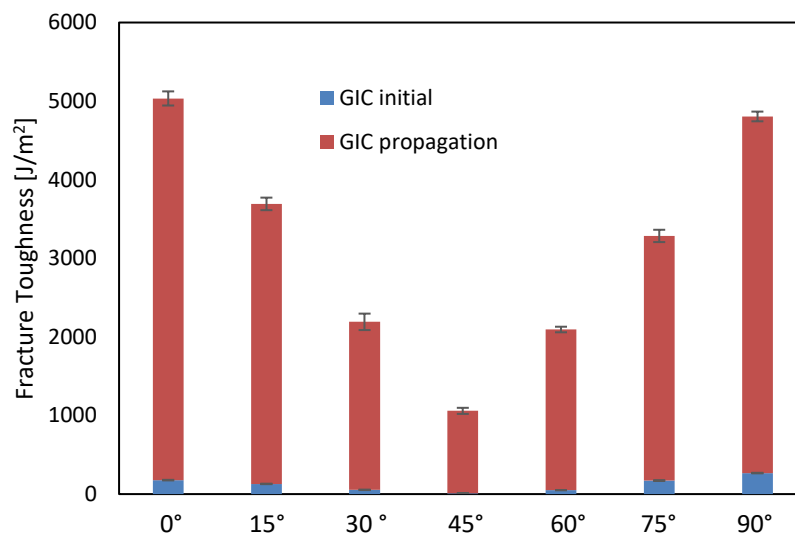
Figure 50. Mode I's initial and propagation fracture toughness for specimens with different fabric types.

The above experimental data of the DCB fracture test matches the classical lamination theory results in section 2.3. Based on the classical lamination theory, extensional stiffness affects the composite materials' response to the applied load. One can conclude that the CFRP/steel laminate will have a minimal mid-plane strain for a given resultant

force since the elements of its [A] matrix were the highest when compared to other laminate matrices. Terms A_{16} and A_{26} couple shear and expected responses of the laminate. It could be noticed from Table 4 that all GFRP/steel laminates with an orientation other than 0° have nonzero values for A_{16} and A_{26}. Therefore, a resultant extensional force on those laminates will generate extensional strain and shear strain. Second, when the Extension-bending coupling matrices are analyzed, it could be noted that all [B] matrices are nonzero since all the laminates are not symmetric, knowing that this matrix couples extensional response to the bending response of the laminate. The nonzero [B] matrix means that all the above laminates will experience extension and shear deformations and bending–twisting curvatures in mode-I when subjected to the normal force.

3.3.1.2 ENF Test

Figure 51 shows the force-displacement curves of the ENF specimens with different fabric types. As can be seen, the FRP/steel specimens with different fabric types show an overall linear response in the first portion of the graph until reaching the critical force's values, where those values were used to determine the initial interlaminar fracture toughness using equation 11. Then the curves continued rising until the peak loads were recorded. CFRP parts reached the higher forces values by around 2000 N. Then, a clear and sudden load drop was observed. This is expected behavior since the mid-plane surfaces slide over each other, leading to fast crack growth and sudden load drop when subjected to an in-plane shear loading. KFRP and GFRP parts behavior were slightly different. The load values kept fluctuating and decreasing gradually until failure, indicating much slower crack growth with more stable loading responses during the test.
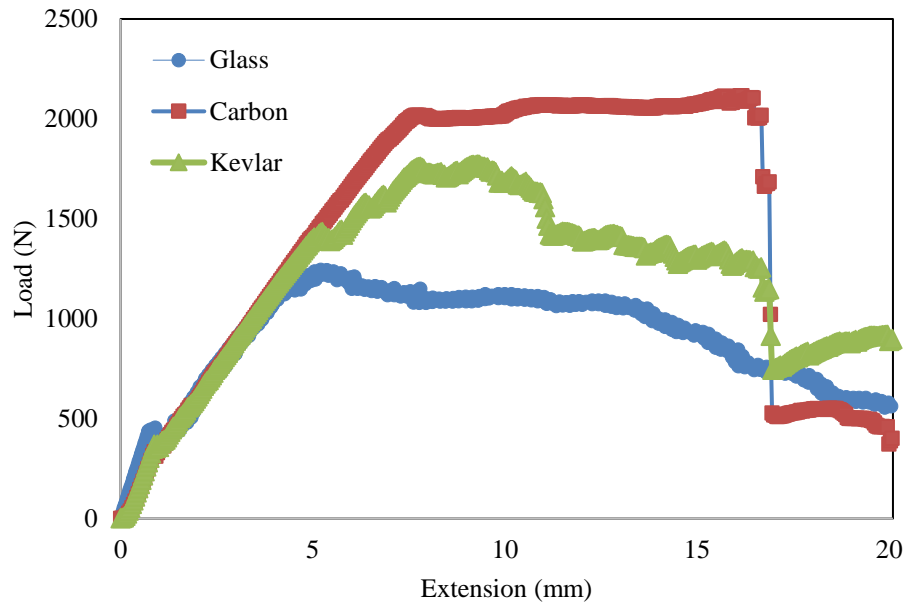
Figure 51. force-displacement curves of the ENF specimens with different fabric types.

Table 8 demonstrates the effect of using different fabric types on the total energy absorbed during testing mode II interlaminar fracture specimens. The force-displacement curves of the identical specimens overlapped each other well, which proves that the results are reliable. It was shown that the specimens made of steel-CFRP were the specimens that had the highest fracture toughness, where G_{IIC} initial and propagation values reached more than 290 and 20000 J/m^2 respectively. This fact reveals that Steel-CFRP specimens have good interface properties. Figure 52 shows a Comparison between the mode II initial and propagation fracture toughness for specimens with different fabric types.

Table 8. Mode II interlaminar fracture toughness G_{IIC} for different fabric types.

Fabric Type	G_{IIC} initial value [J/m^2]	G_{IIC} propagation value [J/m^2]
CFRP	294.80± 2.41%	20189.03± 2.89%
KFRP	254.46± 3.55%	18544.23± 3.12%
GFRP	239.48± 2.25%	14125.87± 2.47%
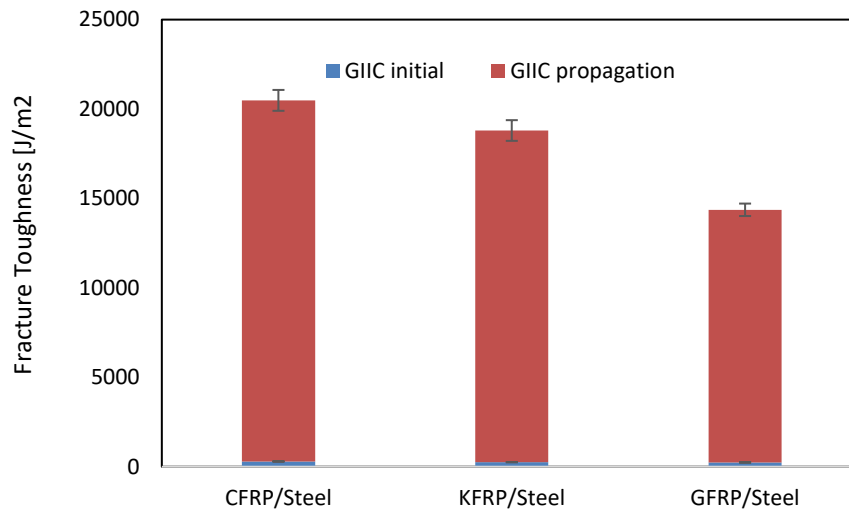
Figure 52. Comparison of the mode II initial and propagation fracture toughness for specimens with different fabric types.

The mode II loading behavior of the FRP/steel specimens with different fabric orientations is plotted in Figure 53. All the ENF specimens display similar and consistent responses, as shown in their load-displacement curves. The specimens reveal an early linear behavior followed by a nonlinear curve up to the peak load. A slow load decrease can be noticed until the test end, where the gradual decrease in force is associated with a decrease in strength. When a decrease in the load rate is noticed, the specimen's stiffness decreases. Specimens with 0° fiber orientation reached the highest forces values (around 1200 N).
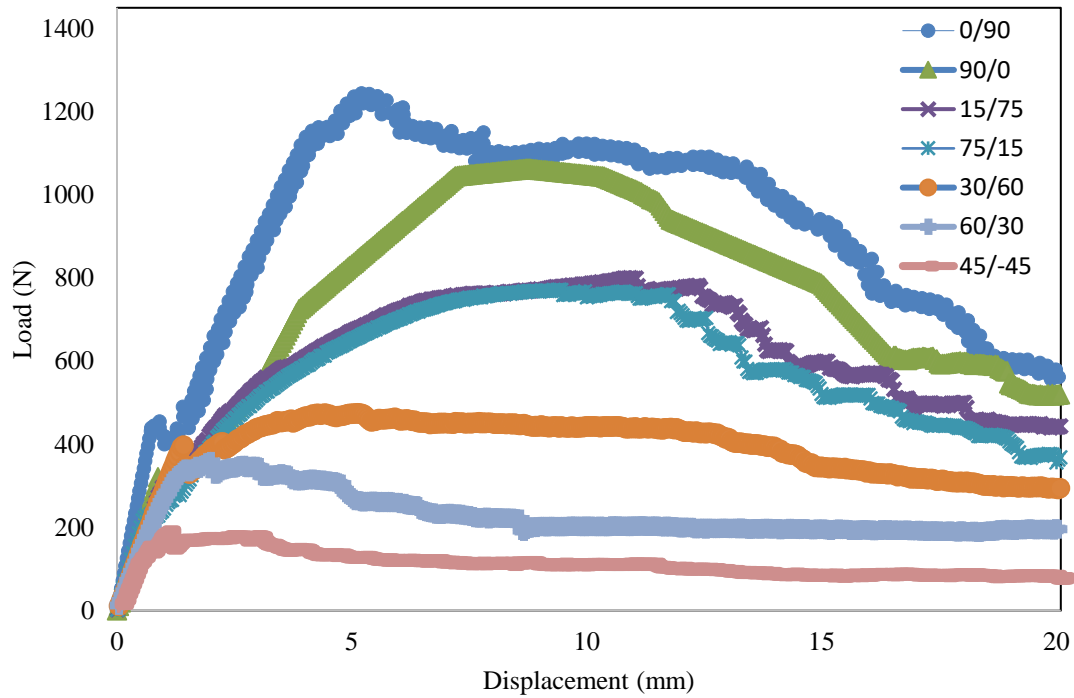
Figure 53. Load-displacement curves of the ENF specimens with different fabric orientations.

Table 9 demonstrates the effect of using different fabric orientation angles on the overall energy absorbed throughout mode II inter-laminar fracturing. G_{IIC} average values for different fabric types were computed and presented with CoV. It was shown that the specimens with 0° fabric orientation had the highest fracture toughness in which the G_{IIC} initial and propagation values reached more than 230 and 14000 J/m^2 respectively. This finding shows that using 0° fabric orientation results in high bond strength of Steel/GFRP specimens. Figure 54 shows a comparison between the mode II initial and propagation fracture toughness for specimens with different fabric orientations.

Table 9. Mode II interlaminar fracture toughness G_{IIC} for different fabric orientations.

Orientation Angle	G_{IIC} initial value [J/m^2]	G_{IIC} propagation value [J/m^2]
0°	239.48± 2.25%	14125.87± 2.47%
15°	224.94± 2.40%	9868.75± 3.45%
30°	194.11± 3.84%	6434.04± 2.16%
45°	81.23± 2.02%	1806.04± 1.89%
60°	161.39± 1.60%	3773.34± 2.76%
75°	198.79± 3.84%	9578.49± 1.57%
90°	229.98± 2.27%	12593.95± 1.48%
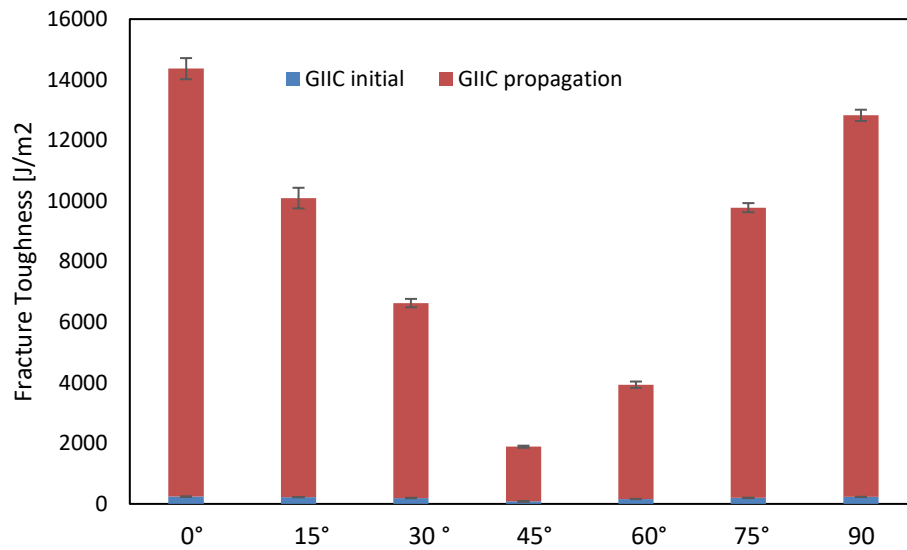
Figure 54. Comparison of the mode II initial and propagation fracture toughness for specimens with different fabric orientations.

The above experimental data of the ENF fracture test matches the classical lamination theory results in section 2.3. All the extension-bending coupling matrices for all specimens in Table 4 are nonzero since no laminates are symmetric. This means that

all the laminates will create bending and twisting curvatures and extension-shear deformations in mode II when subjected to bending moment. Furthermore, looking at the bending-stiffness matrices in Table 4, this matrix influences a laminate's bending response. It could be concluded that the CFRP/steel laminate will generate less curvature when subjected to bending moment since it has the most considerable magnitude of [D] matrix. Terms D_{16} and D_{26} coupled bending and twisting responses of the laminate. It is observed that all GFRP/steel laminates with an orientation other than 0° have nonzero values for D_{16} and D_{26}. Thus, the pure bending moment will generate bending curvature and twist curvature in all of the previously mentioned laminates. Likewise, by analyzing the data in

Table 5, it could be observed that CFRP/steel laminate has the highest A_{44} and A_{55} values, which predicts that when subjected to shear forces, minimal out-of-plane shear strains will be generated while KFRP/steel laminates will have the highest plane shear strain values. Based on experimental data, the results indicate that when the laminates are subjected to loading, it fails earlier in Mode-I load compared to Mode-II loading.

3.3.2 Stress Intensity Factor

Prediction of composite materials' delamination is one of the main challenges to promote the interface between composite and other materials. One useful technique to examine the interlaminar cracks in composite materials is the linear elastic fracture mechanics (LEFM) [19]. The FRP specimens are assumed to be made of an orthotropic material. Therefore, the strain-stress relation is defined using the generalized Hooke's law as follows:

$$
\begin{Bmatrix} \varepsilon_x \\ \varepsilon_y \\ \varepsilon_z \\ \gamma_{yz} \\ \gamma_{xz} \\ \gamma_{xy} \end{Bmatrix} = \begin{bmatrix} a_{11} & a_{12} & a_{13} & 0 & 0 & 0 \\ a_{21} & a_{22} & a_{23} & 0 & 0 & 0 \\ a_{31} & a_{32} & a_{33} & 0 & 0 & 0 \\ 0 & 0 & 0 & a_{44} & 0 & 0 \\ 0 & 0 & 0 & 0 & a_{55} & 0 \\ 0 & 0 & 0 & 0 & 0 & a_{66} \end{bmatrix} \begin{Bmatrix} \sigma_x \\ \sigma_y \\ \sigma_z \\ \tau_{yz} \\ \tau_{xz} \\ \tau_{xy} \end{Bmatrix}
\tag{12}
$$

In which one can write the engineering elastic constants as follows:

$$
\begin{aligned}
a_{11} &= \frac{1}{E_x}, & a_{12} &= -\frac{\vartheta_{yx}}{E_y}, & a_{13} &= -\frac{\vartheta_{zx}}{E_z} \\
a_{21} &= -\frac{\vartheta_{xy}}{E_x}, & a_{22} &= \frac{1}{E_y}, & a_{23} &= -\frac{\vartheta_{zy}}{E_z} \\
a_{31} &= -\frac{\vartheta_{xz}}{E_x}, & a_{32} &= -\frac{\vartheta_{yz}}{E_y}, & a_{33} &= \frac{1}{E_z} \\
a_{44} &= \frac{1}{G_{yz}}, & a_{55} &= \frac{1}{G_{xz}}, & a_{66} &= \frac{1}{G_{xy}}
\end{aligned}
\tag{13}
$$

$$
\frac{1}{E_x} = \frac{m^4}{E_1} + \left(\frac{1}{G_{12}} - \frac{2\vartheta_{12}}{E_1}\right) m^2 n^2 + \frac{n^4}{E_2}
\tag{14}
$$

And, $\quad \dfrac{1}{E_y} = \dfrac{n^4}{E_1} + \left(\dfrac{1}{G_{12}} - \dfrac{2\vartheta_{12}}{E_1}\right) m^2 n^2 + \dfrac{m^4}{E_2}$ $\tag{15}$

$$
\frac{1}{G_{xy}} = 2m^2 n^2 \left(\frac{2}{E_1} + \frac{2}{E_2} + \frac{4\vartheta_{12}}{E_1} - \frac{1}{G_{12}}\right) + \frac{(n^4 + m^4)}{G_{12}}
\tag{16}
$$

Where xyz is the global directions, 123 are the principal material directions, m=cosθ, and n=sinθ. The values for E_1, E_2, G_{12} and υ_{12} were listed in Table 3. The calculated engineering elastic constants are listed in Table 10. The relationships for an orthotropic material's energy release rates will be utilized to define the stress intensity factors for mode I and mode II of each specimen [153]. The stress intensity factor depends on specimen geometry, the crack's size and location, and the magnitude and distribution of loads on the material [154].

$$
G_I = \frac{K_I^2}{E_I}, \qquad G_{II} = \frac{K_{II}^2}{E_{II}}
\tag{17}
$$

Where E_I and E_{II} are the effective moduli for modes I and II, one can calculate the

effective moduli as follows:

$$E_I = \sqrt{\frac{2}{a_{11}a_{22}}} \frac{1}{\sqrt{\sqrt{\frac{a_{22}}{a_{11}}} + \frac{2a_{12}+a_{66}}{2a_{11}}}} \quad , \qquad\qquad E_{II} = \frac{\sqrt{2}}{a_{11}} \frac{1}{\sqrt{\sqrt{\frac{a_{22}}{a_{11}}} + \frac{2a_{12}+a_{66}}{2a_{11}}}} \quad (18)$$

K_I and K_{II} are stress intensity for modes I and II, respectively [155].

G_I and G_{II} are the fracture toughness for modes I and II, respectively.

Table 11 lists the calculated effective moduli and stress intensity factors using Equations (17) and (18). So as K_I and K_{II} values increase, the resistance to fracture will also increase. One can notice that CFRP/Steel specimens have the highest resistance to fracture than the other tested fabric types. While for the different orientation angles in GFRP/Steel, the specimens with 0° and 90° orientation angles have the highest resistance to modes I and II, respectively.

Table 10. Apparent Engineering constants and engineering elastic constants for each specimen.

Specimens	E_x (GPa)	E_y (GPa)	G_{xy} (GPa)	v_{xy}	v_{yx}	a_{11} (GPa)	a_{22} (GPa)	a_{12} (GPa)	a_{66}(GPa)
CFRP 0°/Steel	121.2	119.3	19.97	0.161	0.158	0.0083	0.0084	-0.00132	0.0501
KFRP 0°/Steel	68.95	68.95	34.47	0.168	0.168	0.0145	0.0145	-0.00244	0.0290
GFRP 0°/Steel	62.70	61.79	17.38	0.205	0.202	0.0159	0.0162	-0.00327	0.0575
GFRP 15°/Steel	58.33	57.64	18.93	0.26	0.256	0.0171	0.0173	-0.00444	0.0528
GFRP 30°/Steel	51.16	50.86	23.05	0.348	0.346	0.0195	0.0197	-0.00680	0.0434
GFRP 45°/Steel	48.12	48.12	25.86	0.384	0.384	0.0208	0.0208	-0.00798	0.0387
GFRP 60°/Steel	50.86	51.16	23.05	0.346	0.348	0.0197	0.0195	-0.00680	0.0434
GFRP 75°/Steel	57.64	58.33	18.93	0.256	0.26	0.0173	0.0171	-0.00446	0.0528
GFRP 90°/Steel	61.79	62.70	17.38	0.202	0.205	0.0162	0.0159	-0.00327	0.0575

Table 11. Stress intensity factors, Modes I and II, effective moduli.

Specimens	E_I (GPa)	E_{II} (GPa)	G_I initial	G_{II} initial	K_I (MPa$\sqrt{m}$)	K_{II} (MPa$\sqrt{m}$)
Effect of Fiber types						
CFRP 0°/Steel	169.00	171.0	395.35	294.8	8.18	7.09
KFRP 0°/Steel	97.50	97.5	369.45	254.46	6.00	4.98
GFRP 0°/Steel	87.70	88.3	177.75	239.48	3.95	4.59
Effect of Fiber Orientation						
GFRP 0°/Steel	87.70	88.30	177.75	239.48	3.95	4.59
GFRP 15°/Steel	81.80	82.20	139.62	224.94	3.38	4.30
GFRP 30°/Steel	72.00	72.20	54.10	194.11	1.97	3.74
GFRP 45°/Steel	68.10	68.10	8.67	81.23	0.77	2.35
GFRP 60°/Steel	72.20	72.00	50.35	161.39	1.91	3.40
GFRP 75°/Steel	82.20	81.80	129.75	198.79	3.27	4.03
GFRP 90°/Steel	88.30	87.70	172.28	229.98	3.90	4.49

3.3.3 Failure Surfaces of Mode I and Mode II Interlaminar Fracture

All modes of failure and the interlaminar fracture surfaces were identified using the SEM. All the failure modes of the modes I and II interlaminar fracture specimens were classified and presented in Figure 56, Figure 57, Figure 58, and Figure 60, respectively, with three different scales (1400 µm, 700 µm, and 180 µm) using the microscopic investigations via scanning electron microscopy. The fractured surfaces were coated with Gold palladium/platinum coating in the fine auto coater to make the polymer surface conductive.

3.3.3.1 Mode-I Interlaminar Failure Surfaces

Figure 55 shows post-failure images for the specimens that were tested for mode I; some specimens experienced total separation between the steel and composite layer without any breakage, while other specimens experienced complete separation in the area of the Teflon layer. The composite layer then starts to break completely in the area where the adhesion between layers is vital, as shown in the following images.

Figure 55. Illustration of typical macroscopic post-failure mode for the KFRP composites with fiber orientation of 90°.

For mode-I fracture, the SEM specimens were taken from the crack initiation area beyond the pre-crack insert film. The fractography of all the steel-composite specimens tested for mode I reveal that they have established some cracking, fiber-matrix

debonding, and peeling off for the resin matrix layer in some sheet areas; some fiber failure and breakage of the applied tensile loads were detected using SEM. The SEM images of fractured surfaces of GFRP specimens with different fabric orientations were observed; each fracture type was labeled in the figures. The surface shows the broken fibers, pull-out, and matrix peeling caused by Mode-I loading. Usually, throughout delamination, matrix shear yielding happens in resin-rich areas by stretching the neighboring fibers causing a higher energy absorption [150]. This failure mechanism was detected in many specimens.
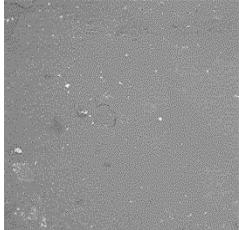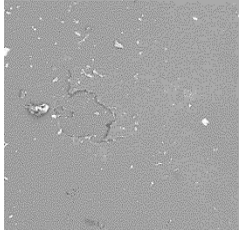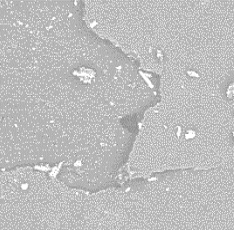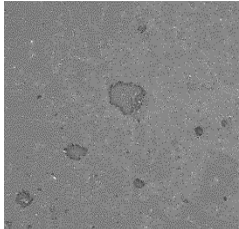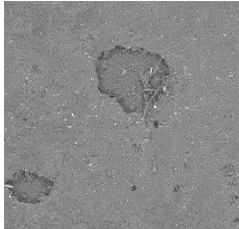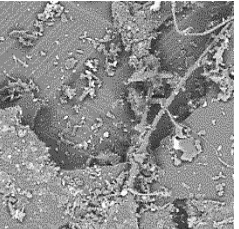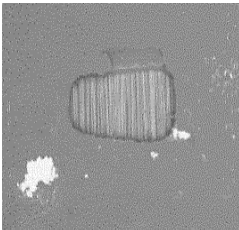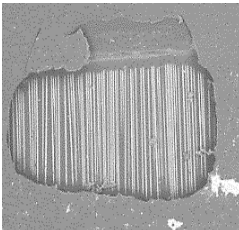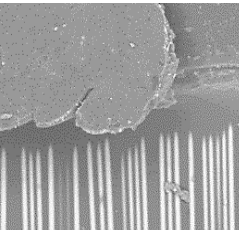
Fiber type	1400 µm	700 µm	180 µm
CFRP			

For CFRP, the failure mode is dominated by only matrix cracks.

| KFRP | | | |

For KFRP, the failure mode is dominated by multiple matrix cracks and fiber debonding.

| GFRP | | | |

For GFRP, the failure mode is dominated by multiple matrix cracks and progressive fiber debonding.

Figure 56. SEM images for mode I test specimens with different fabric types.

Orientation angle	1400 µm	700 µm	180 µm
0°			
15°			
30°			
45°			
60°			
75°			
90°			

Figure 57. SEM images for mode I test specimens with different orientation angles.

The domination failure mode is associated with multiple matrix cracks, progressive fiber debonding, and fiber breakage.

3.3.3.2 Mode-II Interlaminar Failure Surfaces

Figure 59 shows post-failure images for the specimens tested for mode II. All steel-composite specimens tested for mode II have caused multiple matrix cracks and debonding between the fiber and the matrix, accompanied by fiber fracture attributed to the flexural loads, which was also examined using SEM. One can observe that the fiber breakage region was located near the point flexural load, as shown in Figure 58 and Figure 60.
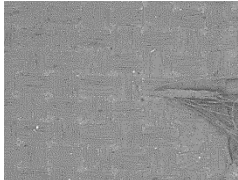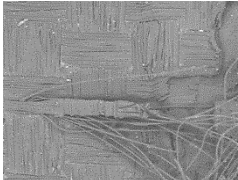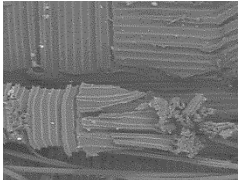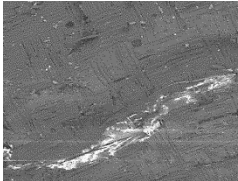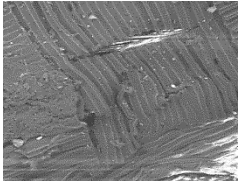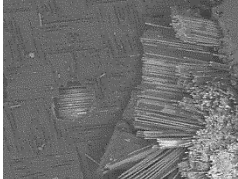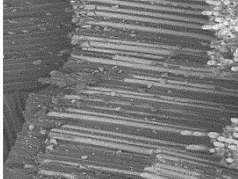
Fiber type	1400 µm	700 µm	180 µm
CFRP			
KFRP			
GFRP			

Figure 58. SEM images for mode II test specimens with different fabric types.

The failure mode is dominated by matrix cracks, fiber debonding, delamination, and fiber breakage for CFRP. For KFRP, the failure mode is dominated by multiple matrix cracks and fiber kinking. For GFRP, the failure mode is dominated by multiple matrix cracks, progressive fiber debonding, delamination, and progressive fiber breakage.

(a)   (b)
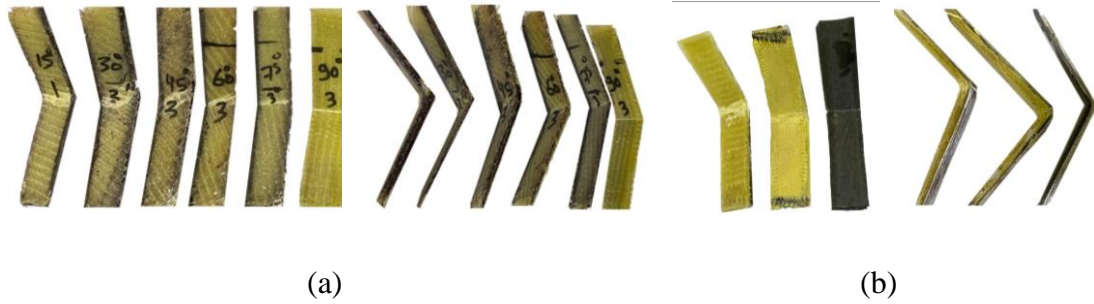
Figure 59. Post failure images for mode II test specimens a- different orientation angles, b- different fabric type.

Scanning electron microscopy images of the fracture area near the mode-II GFRP specimen's crack tip with different fabric orientations are shown in Figure 60. All over the specimens' fracture surface, broken fibers were observed following the fiber-matrix debonding in the vicinity of the series of matrix cracks. It is also interesting to note that progressive debonding between fiber and matrix failures is in areas of the matrix deformation among adjacent fibers that are elevated parallel to one another and tend to incline in the same direction over the whole surface. Similar failure modes are identified by other researchers [24, 25].

Orientation Angle	1400 μm	700 μm	180 μm
0°			
15°			

30°			
45°			
60°			
90°			
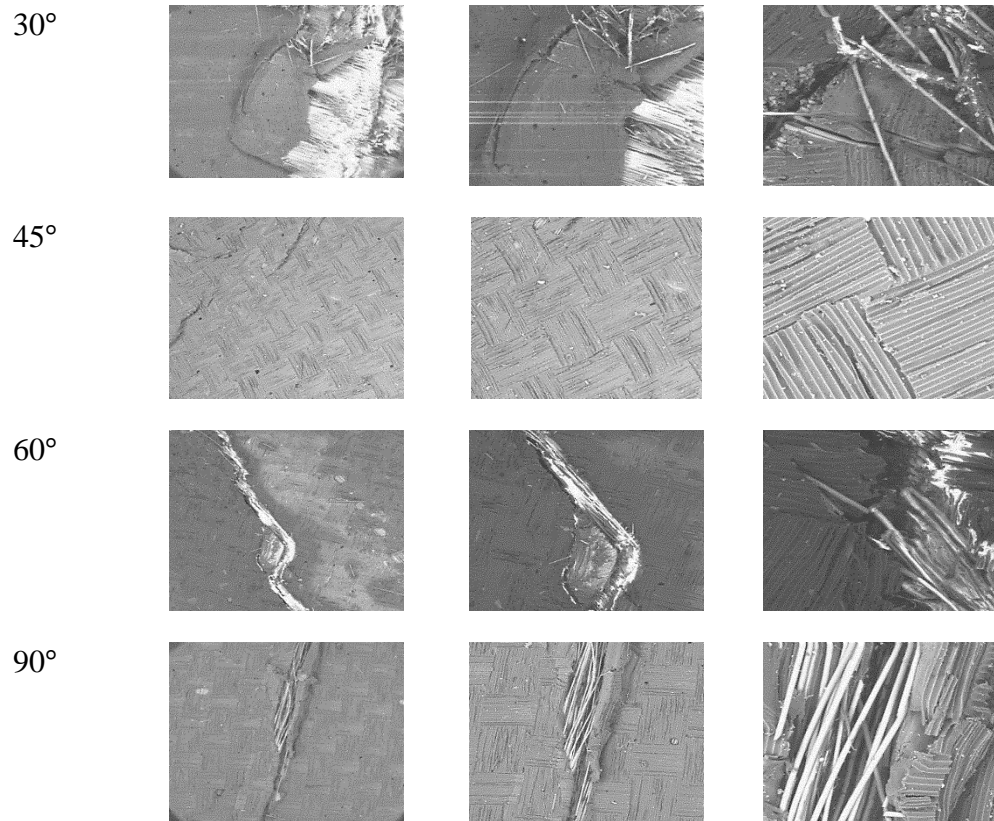
Figure 60. SEM images for mode II test specimens with different orientation angles. The failure mode is dominated by multiple matrix cracks, progressive fiber debonding, delamination, and progressive fiber breakage.

3.4 Summary

The present chapter investigates the fiber type and fiber orientation's effects on the interface bonding between steel and fiber-reinforced composites. The fracture loads for modes I and II were computed using DCB and ENF tests. The outcomes of this study are listed below:

1. The interface bonding between the steel and fiber-reinforced composite and the modes I and II fracture toughness had been significantly affected by fiber orientation and fiber types.

2. For both modes I and II tests, the CFRP/steel interface exhibited the highest toughness when comparing the different tested fabric types. However, when comparing the effect of fiber orientations, the 0° GFRP/Steel interface had the maximum toughnesses for mode I and mode II tests.

3. It is well observed that all specimens' delamination response strongly depends on the loading condition. The shearing-mode (mode II) fracture toughness is larger than the opening-mode (mode I) fracture toughness in all the tested specimens, proving that the interface between FRP and steel layer is stronger in mode II than in mode I due to the compaction process during the bending loading. While in mode I, the loading process is opening.

4. All steel-composite specimens tested for mode I have established some cracking and peeling off for the resin matrix layer in some sheet areas, followed by some fiber failure and breakage because of the applied tensile loads.

5. All steel-composite specimens tested for mode II have experienced matrix cracks and fiber-matrix debonding followed by fiber failure and breakage due to the applied bending loads, which was observed using SEM.

CHAPTER 4: THE USE OF COMPOSITE TO ELIMINATE THE EFFECT OF

WELDING ON THE BENDING BEHAVIOR OF METALLIC PIPES

4.1 Introduction

Welded pipes are exposed to high internal fluid pressure and harmful environmental conditions [32], [156]–[159]. The most appropriate materials regarding oil & gas pipeline production necessities are High-strength low-alloy steels (HSLA) [160]. As stated by the American Petroleum Institute (API), pipeline materials are made from two specification levels, recognized as Product Specification Level (PSL 1) and (PSL 2) [161]. Thermal cycles and cooling rates of welding perform a significant role in microstructure changes [162]. Welding repair for pipes and plates is acceptable in the PSL1 pipes grade only while forbidden in the cases of PSL2 pipes grade [163]. Many researchers and experts have inspected the failure in pipelines to discover their probable source, where it was found out that the failure locates in four different locations. The first location is the weld metal due to erosion, corrosion, and crack infusion zone, fatigue crack in a weld, and weld defects [164]–[167]. The second location is in the heat-affected zone (HAZ), mainly due to the hydrogen embrittlement [168]. When hydrogen gas deceives in the molten steel throughout welding, it results in hydrogen embrittlement. It could be noticed as a crack that occurs after the weld is cooled and solidified, thus recognized as hydrogen-induced cold cracking. A desirable location for this type of crack is at the HAZ or the crossing point between the weld and HAZ [169]. The third location is at the weld and HAZ interface due to the disarrangement of the external surface welds and the internal welds and due to cracks in the sideways of the weld because of the transit fatigue [170], [171]. The fourth location is in the main body of the pipe due to mechanical damage [172]. It was concluded that in welded structures,

the most vulnerable failure locations are weld metal and HAZ, where HAZ are regions of parent metal nearby the welded metal that stands a high welding temperature related to differences in temperature peak (TP). Throughout welding, the HAZ experiences microstructural fluctuations without being melted. When the spacing from the line of fusion is as far as possible, the TP drops. This thermal change in HAZ offers inhomogeneity and microstructural changes all over its width [173]. HAZ life estimation is so challenging since it is complicated to predict the effect of material structure changes throughout the welding procedure [174]. The main reasons for the failure in pipelines are hydrogen embrittlement, corrosion, and wrong welding. Harmful environmental properties and welding heat could be reduced, but it will not always be economically functional [175]. Corrosion happens in several ways like galvanic couples, weld decay, pitting, and stress-corrosion cracking [176]. The welded joints are liable to corrosion because of several causes. Generally, it is due to the change in chemical composition, metallurgical structure, and residual stress levels inside the welded structure [177]. Several rates of cooling for the HAZ and welded metal produce several amounts of residual stresses in many segments of a welded structure. Residual stresses raise the degree of deterioration by creep and fatigue. Throughout the welding process, compressive yielding happens nearby the molten material because of the high temperature and enlargement of the welded material [178]. On the other hand, a longitudinal tensile residual stress of the weld is brought while the welded material is being cooled. If the value of tensile residual stresses goes above the yielding boundary for material, it will distort causing deformed structure. Protective actions, which apply to reduce the corrosion phenomena, are; avoidance of defect creation, use of passivation treatment, and elimination of hydrogen sources [179]. Two decisions could be taken in case of failure, either to repair or to replace. Maintenances of welds at the same position

regularly happens. However, studies indicate that more thermal changes lead to opposing influence on the material properties [180]. Researchers and specialists are always promoting new techniques to enhance the durability of the welded pipes. Up-to-date improvement for better microstructure and welding properties, generally are; the addition of alloying elements; improvement of filler materials and welding systems. Researchers and specialists are working on new techniques for weld testing and investigation to be capable of evaluating the capability of a welded pipe. In this study an FRP composite system is proposed to be overwrapped the welded and heat-affected zone areas, this will give more strength for the heat-affected areas as well as eliminate the possibility of corrosion occurrence. Fiber-reinforced composites are extensively employed in the aerospace industry because of their excellent stiffness and strength to weight ratio [181]. Moreover, recently, they were being used as a repair system for oil and gas transmission pipelines [87], [182]–[185]. The use of FRP composite materials results in many advantages; it is cheap, quick procedure that does not need much time, corrosion resistance, gives extra strength to the welded region and the fluid transmission will not stop during overwrapping [119]. Also, specific strength and specific modulus of FRP materials are high compared with the other repair systems. FRP materials can resist fatigue; it is also an excellent electrical insulator, and an easily designable material [186]. To evaluate the effectiveness of the composite overwrapped welded and heat-affected areas; firstly, welded steel pipe specimens were prepared. Secondly, the welded regions were overwrapped with a composite material (i.e., glass fiber and epoxy resin) using 5-axes filament winding machine, and finally, the fabricated specimens have been tested using three-point and four-point bending tests, and the results were presented and discussed.

4.2 Materials and Methods

4.2.1 Materials

Welded carbon steel pipe specimens were prepared according to the EN10210 standard, as shown in Figure 61-a and b, and the specifications are listed in Table 12. Then the welded regions were overwrapped with a GFRP composite (See Figure 61-c). The polymeric matrix is composed of epoxy resin (EL2) and hardener (AT30). The properties of the epoxy resin matrix are listed in Table 13.

Table 12. The specifications of the EN10210 S355J2H steel pipe.

Geometry		Mechanical Properties			Chemical Composition				
Diameter (mm)	Wall Thick. (mm)	Kg/m	Yield Strength (MPa)	Tensile Strength (MPa)	C max (%)	Si max (%)	Mn max (%)	P max (%)	S max (%)
114	4	10.9	355	470	0.22	0.55	1.6	0.03	0.03

Table 13. Physical properties of epoxy resin and hardener.

Material	Viscosity @ 25°C (mPa.s)	Density @ 20°C (g/cm³)
EL2 Resin	1200 - 1800	1.13 - 1.17
AT30 Slow-Hardener	5-20	0.90-0.95

4.2.2 Fabrication of GFRP Composite Overwrapped System

The 5-axes filament-winding machine was used to overwrap the welded steel pipes with the FRP material. A filament winding machine in overwrapping steel pipes is the most appropriate fabrication process [187]. The matrix comprises 100 parts mass of the epoxy resin (EL2) and 30 parts mass of curing agent (AT30). Since the overwrapped area is limited to the heat-affected zone, the fiber orientation angle for all the samples was chosen to be at 90° (Figure 61-c). The average thickness of the composite

overwrapped system in all the specimens was 3.5mm± 0.5, consisting of 8 FRP layers.

a-

b-

c- Hoop winding

d-
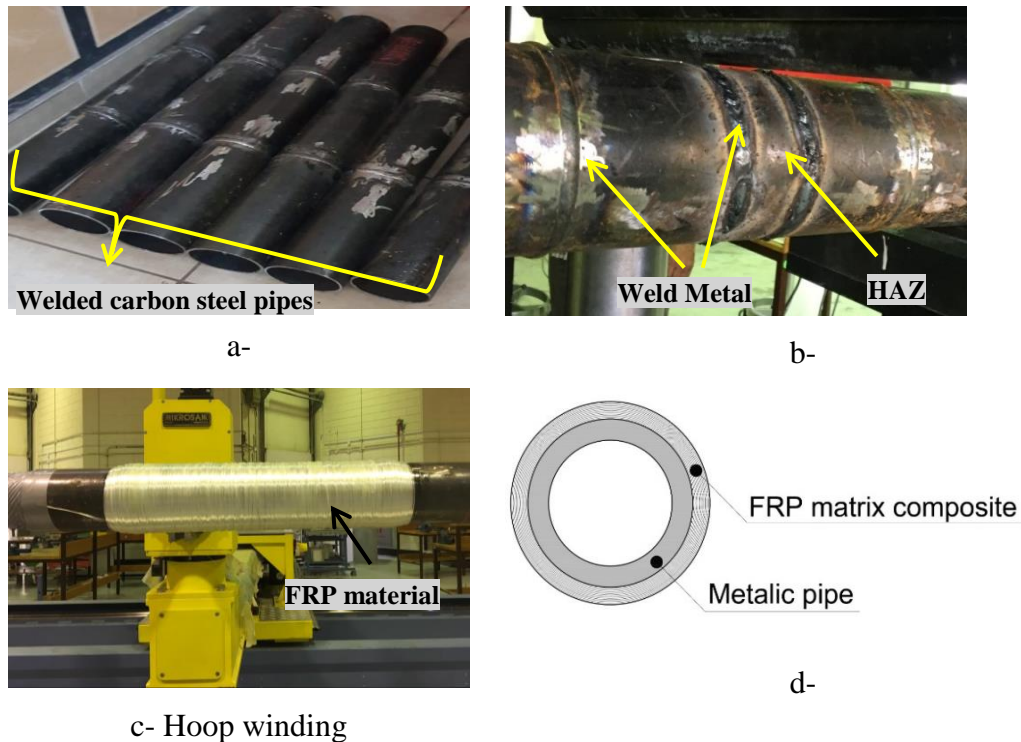
Figure 61. Steel pipe specimen; a- welded steel pipes with two welding lines, b- welded steel pipes with four welding lines, c- welded steel/composite pipe, d- side cross-section of the steel-composite pipe.

4.2.3 Flexural Test

During pipe bending, the bending moment leads to changes in shape. Besides compressive and tensile stresses, shear stress also happens. The deformation results from combined stresses in the pipe cross-section. Previous studies show that an appropriate way of determining the effect of the mentioned stresses during bending is to apply 3-point and 4-point bending [188]. Therefore, three-point and four-point bending tests of the composite pipe specimens were conducted to study the tensile failure and measure the material's ductility and bending stiffness. These tests' objective is to determine flexure strength, the material modulus in specific directions, and interlaminar shear properties for the composite material. Figure 62 depicts the shear

and bending moment diagrams of the three points and four points bending tests. The maximum elastic deflection at the middle of the beam during the three points bending and four points bending can be calculated using the below equations, respectively [189].

$$Y_{max} = -\frac{Fl^3}{48\,E_x\,I_x} \qquad\qquad (19)$$

$$Y_{max} = \frac{Fa}{24\,E_x\,I_x}(4a^2 + 3l^2) \qquad (20)$$

Where:

F = Force acting on the beam

l = Length of the beam between the supports (780mm)

E_x = Modulus of Elasticity

I_x = Area Moment of Inertia

a = Distance from the load to the closest support (237.5 mm)

x stands for the fusion zone, HAZ, or parent material zone.

It is well known that modulus of elasticity varies through various regions of welded pipe, as the fusion zone, HAZ, and parent material, as shown in Figure 62. The strength values decrease away from the weld while the level of generated strain increases, which means the weld's strength is higher than the parent material. This is due to plastic deformation of the parent material generated by the thermal expansion and contraction processes associated with each weld pass [190]. The relation between the strength and modulus of elasticity is proportional, which means that the area of fusion will be having the highest value of Young's modulus and the highest moment of inertia. While for the HAZ, due to the thinning in that area resulting from the plastic deformation, its mechanical strength and stiffness will decrease; therefore, Young's modulus and

moment of inertia will also decrease.
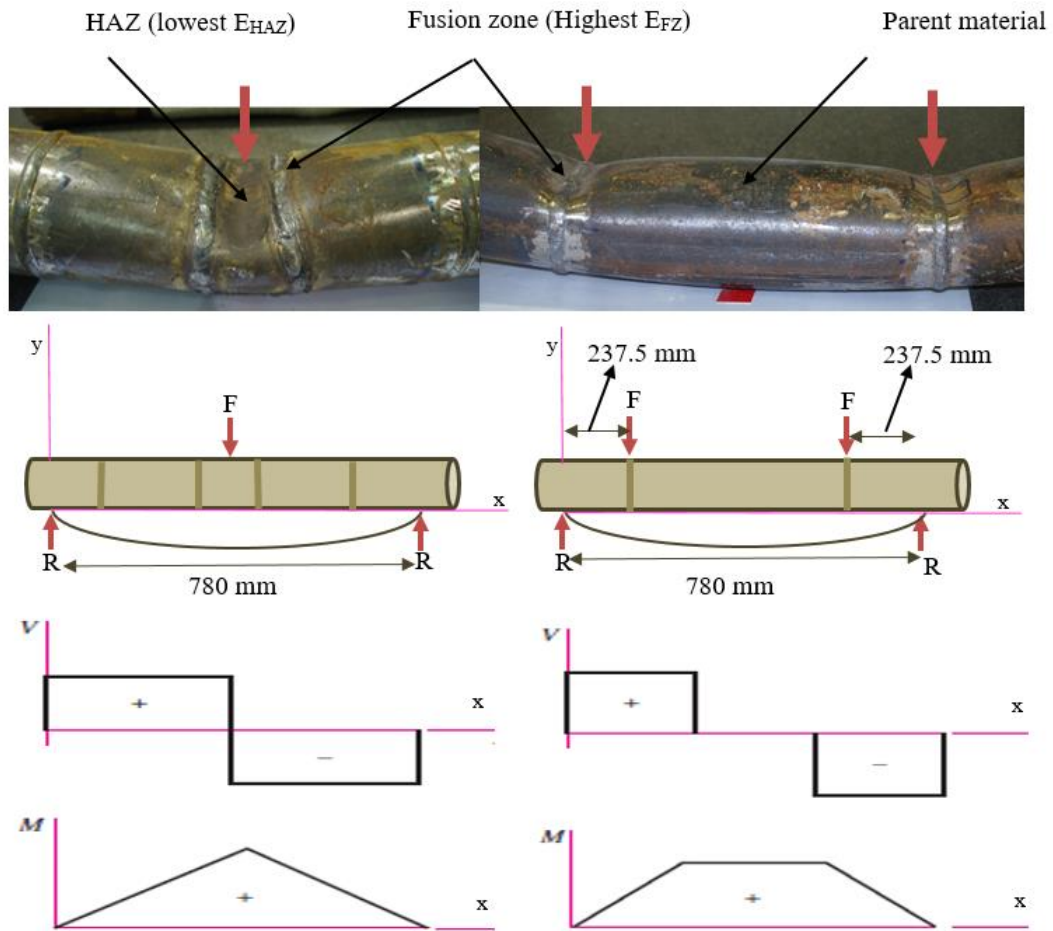
Figure 62. Shear and bending moment diagrams of three- and four-points bending tests.

A schematic view of the three-point and four-point bending tests performed on the hybrid pipes is illustrated in Figure 63, while Figure 64 shows the locations of the load head before tests. The location of the load head was precisely selected to concentrate the load at or near the HAZ. The tests were conducted using an Instron 1500 HDX-SPL bending machine designed for the high-capacity bend/flex testing with a frame capacity of 1500 kN. For measurement accuracy, the machine meets the ASTM E290 standard that describes the requirements for bend testing for ductility of metallic materials. The samples were preloaded with a load of 1.0 kN, then they were loaded to failure under a

constant displacement rate of 2.5 mm/min, and the test stopped when the displacement

reached 90 mm. The test was repeated three times on three different specimens for each

case where the peak loads obtained were consistent for all tests.
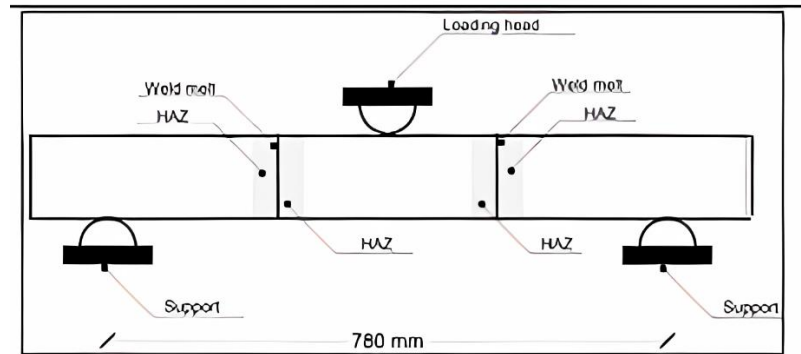
a
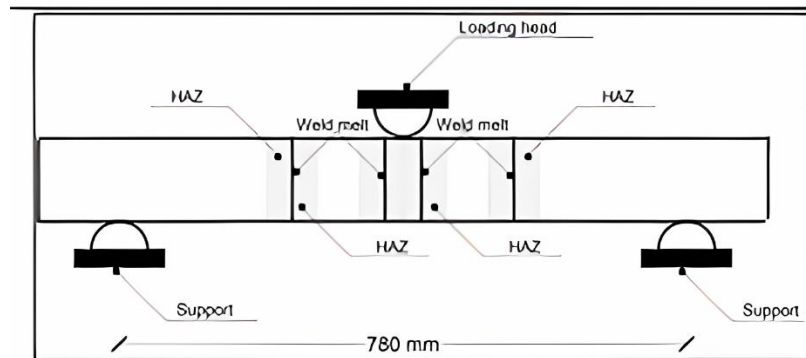
b
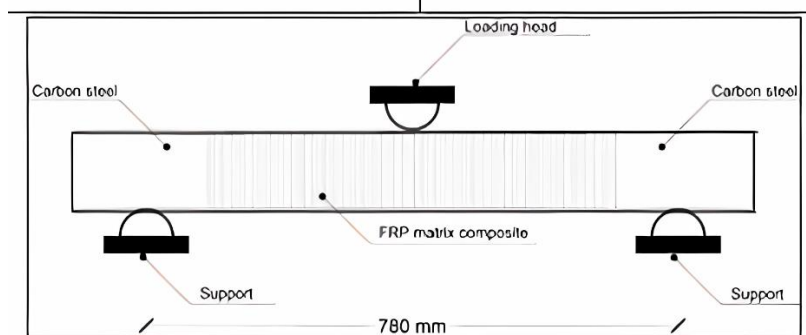
c
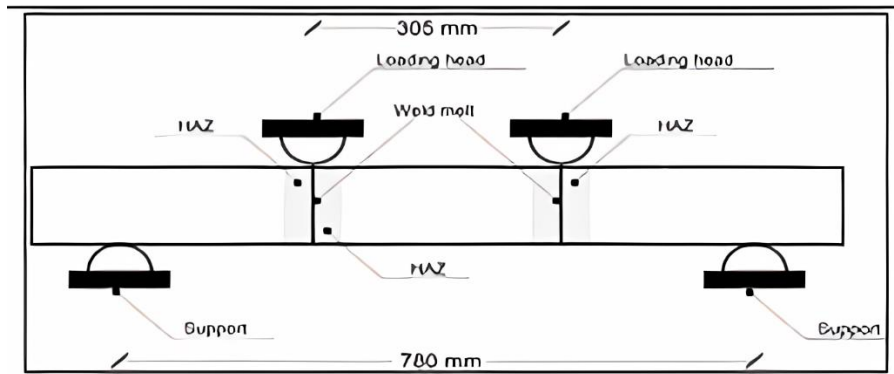
d
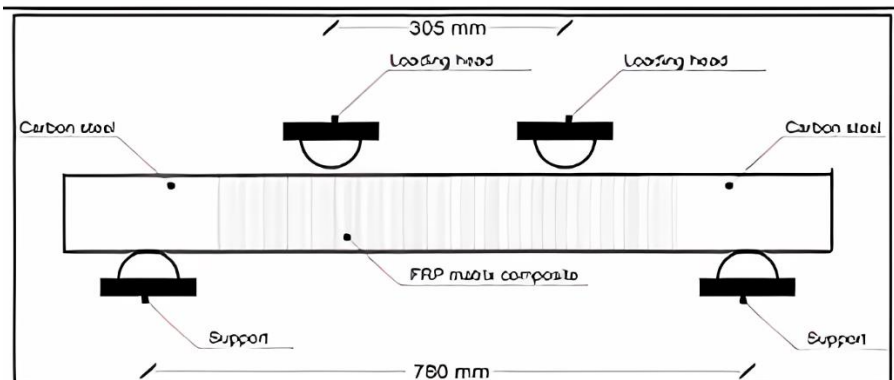
e

Figure 63. Schematic view of; a- 3-point bending of steel pipe with two welding lines, b- 4 welding lines, c- steel-composite pipe, d- 4-point bending of steel pipe with two welding lines, e- steel-composite pipe.

In the case of three-point bending tests, the top load head was consistently applied to the middle of the pipe, where it is the region of HAZ in pipes with four welding lines (Figure 62-b). The distance between the bottom supports (support span SS) was equal to 780 mm in all tests. Complete contact between the top roller and the pipes was achieved because of the smooth top surface of the pipes. While in the case of four-point bending tests, there were two loading heads, where each of them was located precisely above the line of welding (Figure 63-d), with a loading span (LS) of 305 mm and SS of 780mm.
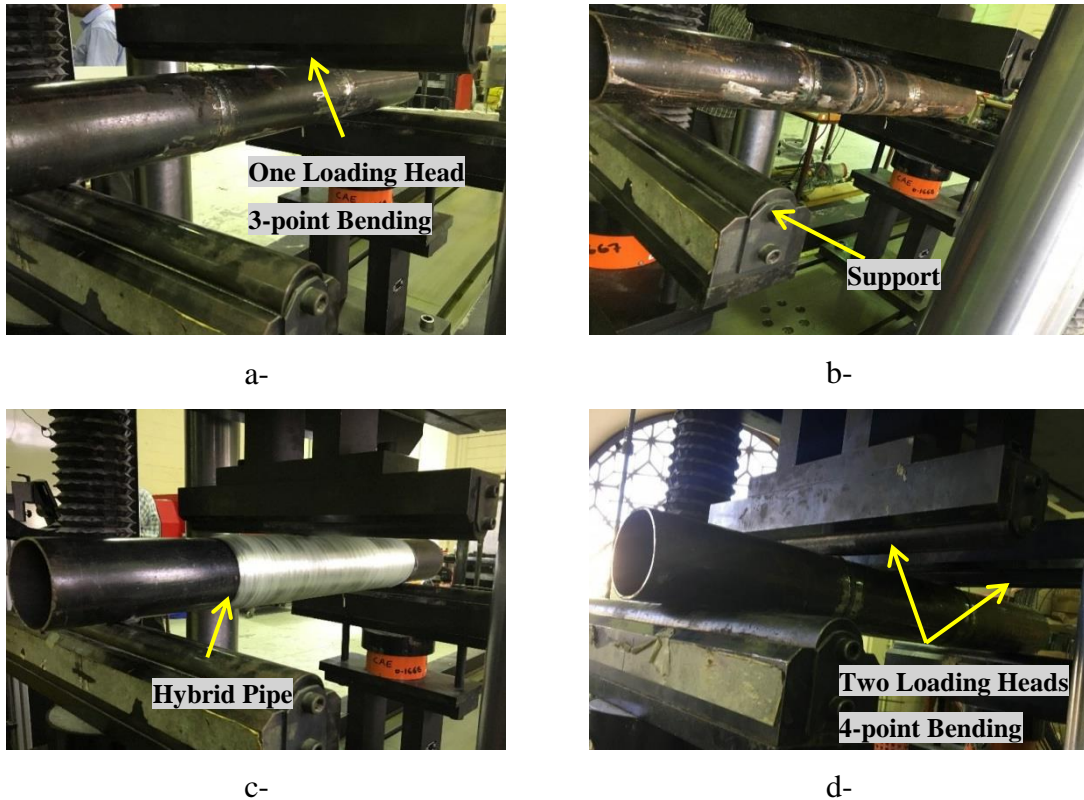
Figure 64. 3-point bending for; a- steel pipe with two welding lines, b- 4 welding line c- steel-composite pipe, and d- 4-point bending for a steel pipe with two welding lines.

4.3 Results and Discussion

The flexural force-deflection curves are shown in (Figure 65), (Figure 66), and (Figure 67) for three-point and four-point bending test results, respectively. The differences in peak load between the cases of wrapped and unwrapped welded steel pipes were quite substantial. It can be noticed that with the use of the FRP composite overwrap system, the maximum flexure load increased when comparing it to the conventional case. An increase of 16.94 kN was achieved in three-point bending with two welding lines along the pipe, 10.35 kN in three-point bending with four welding lines along the pipe 26.8 kN in the case of four-point bending.
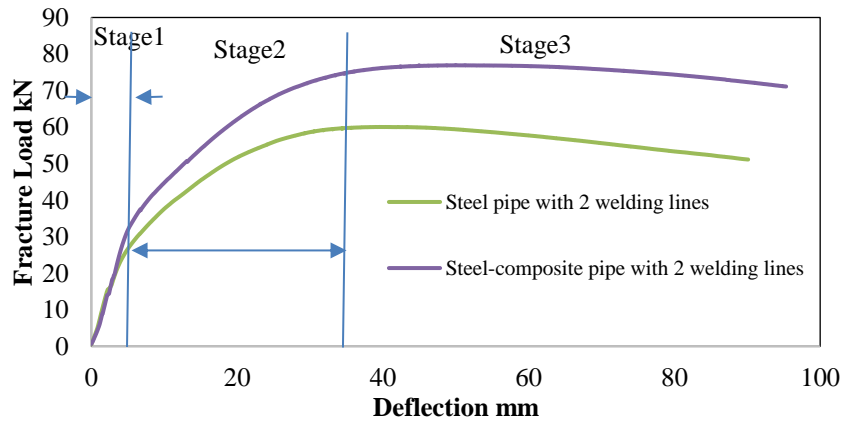
Figure 65. Three-point bending tests for the pipes with two welding lines.
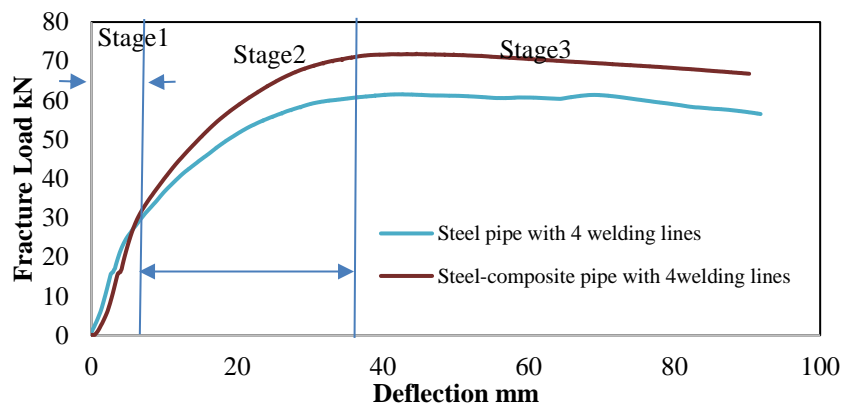
Figure 66. Three-point bending tests for the pipes with four welding lines.
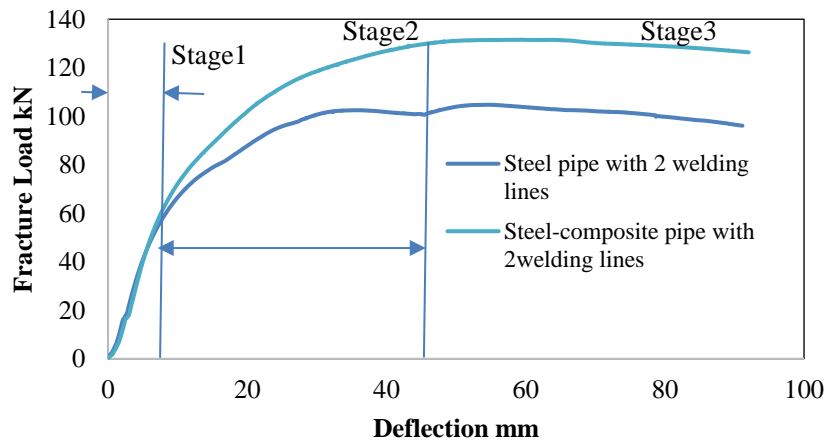
Figure 67. Four-point bending tests.

4.3.1 Bending Behavior of Unwrapped Welded Steel Pipes

When the steel pipes were subjected to bending moment, they went through three stages to increase the applied bending load. The first stage is the elastic stage until the applied

95

load exceeds the yield strength of the bent specimen. This stage had a linear relationship between the fracture load and deflection, as shown in the first portion of the curves in Figure 65, Figure 66, and Figure 67. The second stage is when the circular cross-section starts to form an oval shape. In this stage, the bending load exceeds the ultimate strength. Then the third stage will start immediately after the ultimate bending strength, which is the failure stage since the ultimate strength was exceeded, leading to a gradual decrease in the bending rigidity of the specimen.

4.3.2 Bending Behavior of Wrapped Welded Steel Pipes

In the case of steel-composite samples bending, the first failure mode was the matrix cracking which could be heard during the bending test, and it could be recognized as a slight movement in the load-deflection curve (Figure 65, Figure 66, and Figure 67). Then when the compressive strain exceeded the maximum strain supported by the composite laminate, the crushing of layers started. Moreover, when the compression stress that acts on the composite exceeded the crushing strength of the fibers, the fibers started to break down, which led to the failure of the steel-composite specimen.

4.3.3 Failure Modes

A three-point and four-point bending post-failure images of the pipe specimens were presented and analyzed. Figure 68-a, b, and c show the three-point bending post-failure images of pipes with two welding lines, four welding lines, and when wrapped with composite layer, respectively. Figure 69-a and b show the four-point bending post-failure images of pipes with two welding lines and when wrapped with a composite layer.
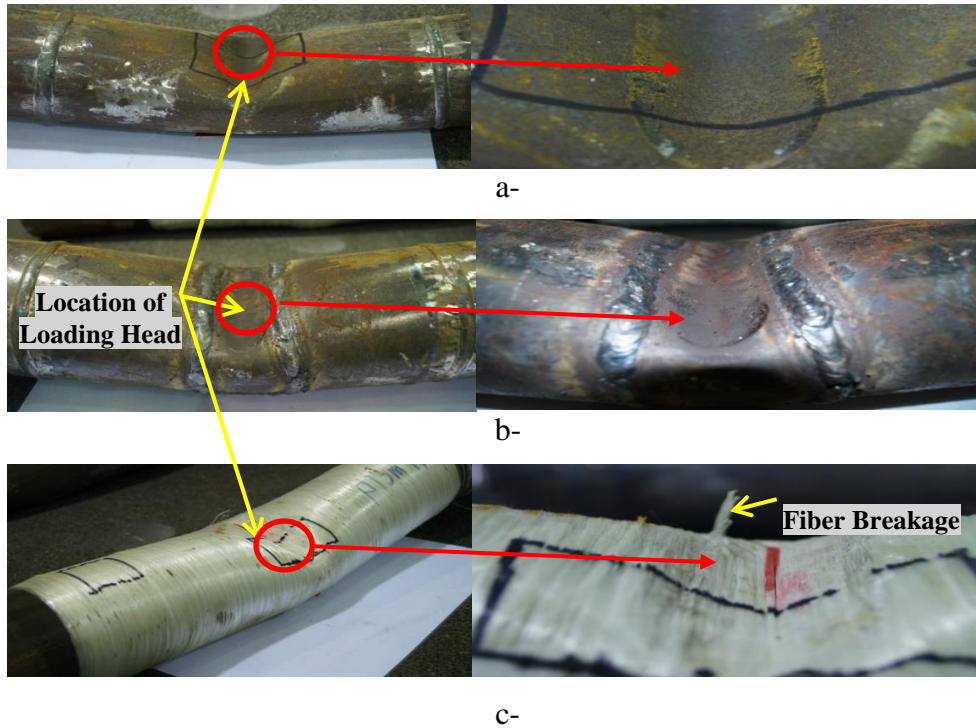
Figure 68. Three-point bending post-failure images; a- steel pipes with two welding lines, b- four welding lines, c-wrapped with composite layers.
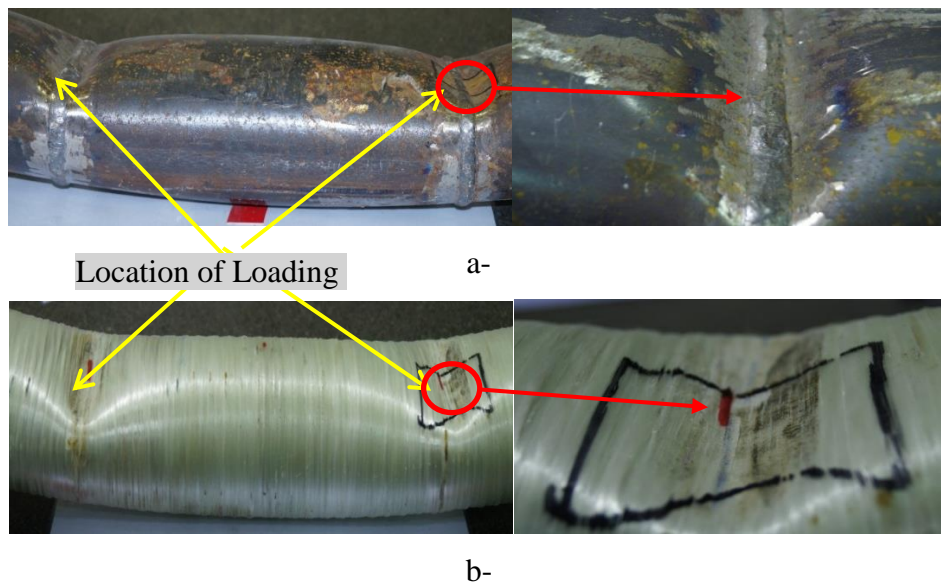
Figure 69. Four-point bending post-failure images; a- steel pipes with two welding lines, b- wrapped with the composite layer.

All steel-composite samples have established matrix cracking and fiber-matrix debonding followed by fiber failure and breakage because of the applied bending loads.

This was observed using scanning electron microscopy (SEM). SEM produced the bent samples that were cut into 1cmx1cm square specimens by scanning the surface with a focused beam of electrons. It could be noticed that the fiber fracture region was mainly positioned in the contact area near the top-loading head. All the failure modes of the fiber-reinforced polymer composite and steel specimens were classified and presented in Figure 70 and Figure 72, respectively, using the microscopic investigations performed on the cut specimens via scanning electron microscopy.

a-

b-

c-
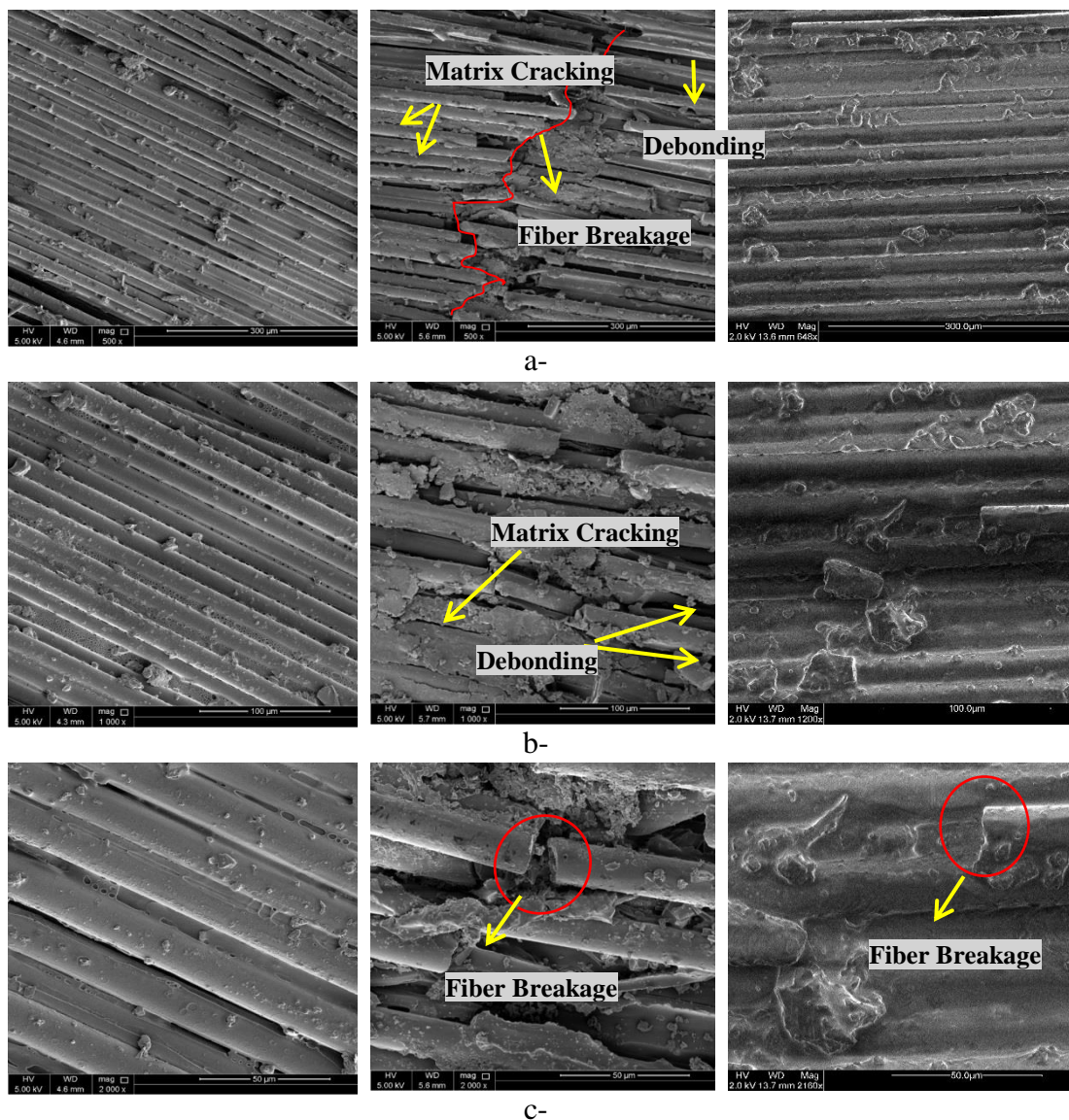
Figure 70. SEM images for the steel-composite specimens a- before bending, b- area on top under bending, c-area on the bottom under tension.

To describe the sequence of events that dominate each failure mode for the steel and steel-composite specimens (Figure 70 and Figure 72); first, all failure criteria are to be expressed in differentiating between different failure mechanisms on the lamina level for the steel-composite specimens (Figure 70). Matrix fracture is mainly produced by the stresses applied to the fracture plane, and its failure criteria involve three stress components, specifically one normal stress and two shear stresses [191]. Therefore, Because of the bending forces acting on each layer, the fractures are disposed to display transverse micro cracks. When the crack in the fiber/matrix interface grows, this will generate the fracture process. The crushing of the layers happens when the compressive strain exceeds the maximum strain supported by the composite laminate. Fiber-matrix debonding is induced because of different reasons but mainly due to voids that result from the manufacturing procedure. Fiber crushing failure mode occurs when the compression stress that acts on the composite exceeds the crushing strength of the fibers, knowing that the fiber strength is a statistical distribution and not just one value. The fibers tend to fail at changing load levels. Therefore, in fiber crushing failures, the fracture happens at various planes since the cracks detach the fibers into isolated structures. To explain the interface between matrix and fiber failure modes, it should be mentioned that some fibers break previously to the existence of macroscopic fiber breakages.

The microfibre Breakages will most likely generate local damages as fiber-matrix debonding and micro-cracks at the neighboring matrix. For the steel specimens, it was shown from the SEM images that the grain size of the HAZ is much coarser than that of the base metal (Figure 71), where a typical microstructure of base metal is composed of ferrite and small regions of pearlite. So, special attention was given to examine the microstructure of the HAZ effect on the bending behavior of the welded pipes, as shown

in Figure 71. Martensitic coarse grain is formed in the heat-affected zone, which is caused by the welding process. It is also observed that the welding process could change the local hardness and adjust the grain structure of the parent material. However, the HAZ of the parent metal next to the weld experienced high temperature throughout welding, followed by air cooling, the coarse grain size was produced. And because of its coarse grain size, it became less ductile, increasing the risk of cracking [192].

a-   b-
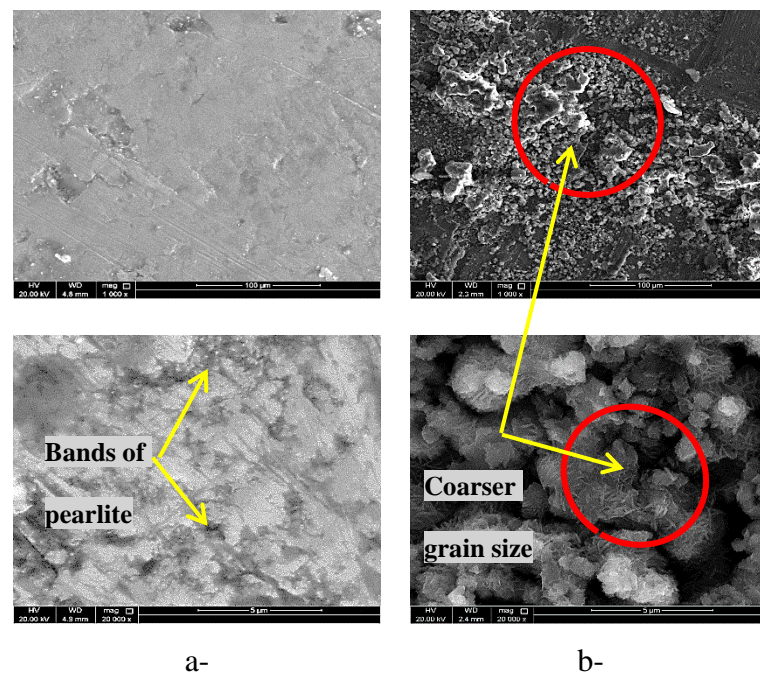
Figure 71. SEM images for the steel specimens a- base metal, b- HAZ.

Some microstructure changes appeared in the high heated area (HAZ), where crystal grains coarsen during the heating since the material contains enough carbon and other elements that increase hardness. Microscopic defects that arise from the manufacturing processes can grow and spread in the material under combined loading and environmental conditions where catastrophic failure may occur. The sequence of events leading to the failure was described to analyze the failure criteria in bent steel specimens (Figure 72). While bending the area on the top of the pipe is exposed to the compression load, the area on the bottom of the pipe is under tension. Strain localization occurred

by the initiation of shear bands or strain localization. With the constant activity of shear bands, there was a growth of notches at the surface of the specimen. Void initiation in highly strained areas caused the formation and growth of cracks. Those cracks appear since the bending load exceeded the ultimate strength, leading to a gradual decrease in the bending rigidity of the specimen. Cracks in welded joints occur at the weld toe where a coarse grain HAZ exists. It can be concluded that increasing stress concentration due to welding defects will sharply reduce fracture strength due to the decrease in yield strength and consequently the increase in plastic deformation.
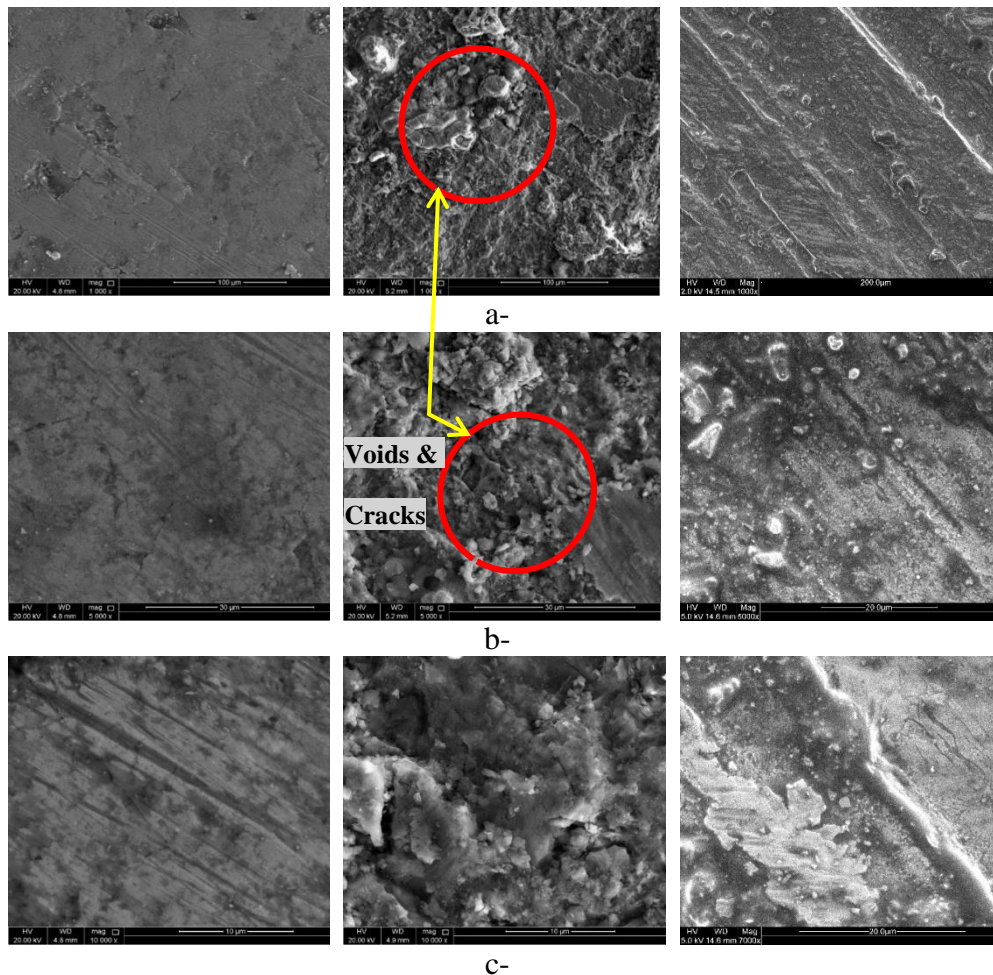
Figure 72. SEM images for the steel specimens (a-) before bending, (b-) area on top of the pipe under compression, c-area on the bottom of the pipe under tension.

4.3 Summary

This chapter aimed to introduce a cost-effective FRP composites overwrap system, give more strength for the welded regions, and eliminate the effect of weld metal and heat-affected zone. When comparing it with the conventional steel pipe, the maximum flexure load increased significantly. Moreover, the plastically deformed steel specimens, which have been taken from HAZ, revealed that they experienced three stages with the increase of the applied bending load; the elastic stage, ovalization stage, and failure stage after exceeding the ultimate strength of the specimen.

CHAPTER 5: INTERNAL PRESSURE CAPACITY OF HYBRID COMPOSITE/STEEL/COMPOSITE PIPES

5.1 Introduction

Many researchers investigated the use of FRP in pipeline failure pressure studies [10] [11] [12]. FRP Composite materials proved to be reliable for repairing damaged pipes, increasing burst pressure, and reducing strain. Singh et al. analyzed a repaired steel pipe's strength using Glass-Carbon Textile Tape numerically and experimentally [52]. The burst pressure was higher by 20%, verified by hydrostatic pressure tests for high-pressure crude transportation. Another application of FRP in steel pipelines is fabricating an overwrapped FRP/steel pipe using filament winding to gain extra strength and be protected from any possible corrosion attack. In the last decades, many researchers investigated the effect of winding angle on the pipe's mechanical integrity [66][67]. Experimental and numerical simulation data indicated that deformation and failure mechanisms depend on the winding angle. In the closed-end testing mode, maximum axial and hoop stresses occurred at a winding angle of 55 ° when comparing specimens with pure angle-ply lay-ups [68]. However, multi-angle lay-ups, Multi-angle wound structures were more advantageous than pure angle-ply lay-ups in damage resistance under different load conditions [69].

It should be noted that optimum winding angles depend on loading modes. Hamed et al. found that for hoop pressure loading (mode I), the winding is optimum at 55°, for biaxial pressure loading (mode II), the winding is optimum at 75°, and for biaxial pressure with axial compressive loading (mode III), the winding is optimum at 85° [70]. In recent research, Colombo et al. carried out an optimization study on composite pipes' winding parameters based on the long-term mechanical reliability [71]. The critical

optimization parameters were pipe wall thickness, fiber type, fiber volume fraction (reported optimal between 40 to 60%), and winding angle (reported optimal between ±44.5° to ±52.5°) – about internal pressure and axial loading. The optimized parameters and minimum wall thickness were obtained from the internal pressure testing, and failure criteria before a recent ISO were implemented for a combined pressure and axial loading. Mahdi et al. studied the internal pressure behavior of repaired damaged metal pipes for onshore application by wrapping fabric carbon-epoxy systems at ±47° and 0°/90°orientations [119]. Pipes with ±47° orientation had higher internal pressure capacity than the hoop 90° wound pipe, observed to fail from axial strain in association to transverse stiffness, dominated by the matrix more than the fiber. This chapter proposes a corrosion-free hybrid pipe, which will improve the pipeline's pressure capacity and eliminate internal and external corrosion. The internal pressure capacity of hybrid composite/steel/composite pipes was tested, and results were compared to conventional steel pipes according to an experimental investigation. The novelty is the internal reinforcement, where an elastic mandrel was used for this purpose.

5.2 Materials and Methods

5.2.1 Materials

ASTM-A-53 Grade B Carbon steel pipe was used for the internal pressure testing. Specimens of 6 cm diameter and 1.5 mm thickness were cut into 40 cm in length each, and they had solid end closures on both sides of the pipe, keeping a small opening that was connected to the fitting of the pressure machine to allow pressurizing the hydraulic fluid inside the pipe while testing as shown in Figure 73. Then they were overwrapped by a composite material that consists of glass fiber filaments and epoxy resin. The chemical composition and mechanical properties of the base material are presented in

Table 14 and Table 15.

<div align="center">(a)   (b)</div>
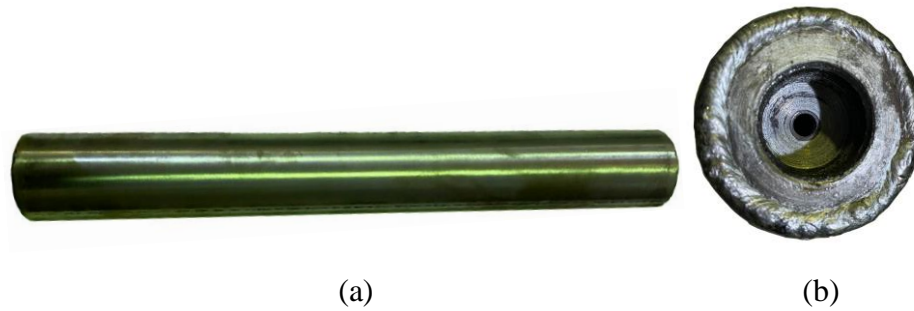
Figure 73. (a) Carbon steel specimen prepared for internal pressure testing, (b) pipe end closure.

Table 14. Chemical composition (wt%) of ASTM-A-53 Grade B carbon steel alloy.

Iron	Carbon	Manganese	Phosphorus	Sulfur	Copper	Nickel	Chromium	Molybdenum	Vanadium
96.9	0.3	1.2	0.05	0.04	0.4	0.4	0.4	0.15	0.08

Table 15. Mechanical properties of ASTM-A-53 Grade B carbon steel alloy.

Yield Strength (MPa)	Tensile Strength (MPa)	Elongation in 50mm Min. (%)	Hardness (HRB)
240	415	21	241

5.2.2 Fabrication Process

Two different specimen types with different winding angles for the external GFRP composite layers were tested. The first specimens were prepared by winding helical layers at an angle of $\pm\,55°$. The second specimens were prepared by hoop windings at an angle of 90° using a computerized 5-axes filament winding machine (Figure 74). The windings were continued over the end closures since it is typical practice to design the ends to be more vital to force the pipe's ultimate rupture or failure to take place in the middle away from the testing fixtures. The polymeric matrix is composed of epoxy

resin (EL2) and hardener (AT30). The matrix comprises 100 parts mass of the epoxy resin (EL2) and 30 parts mass of curing agent (AT30). The average thickness of the composite overwrapped system in all the specimens was 1 mm ± 0.2, consisting of two FRP layers.

(a)   (b)
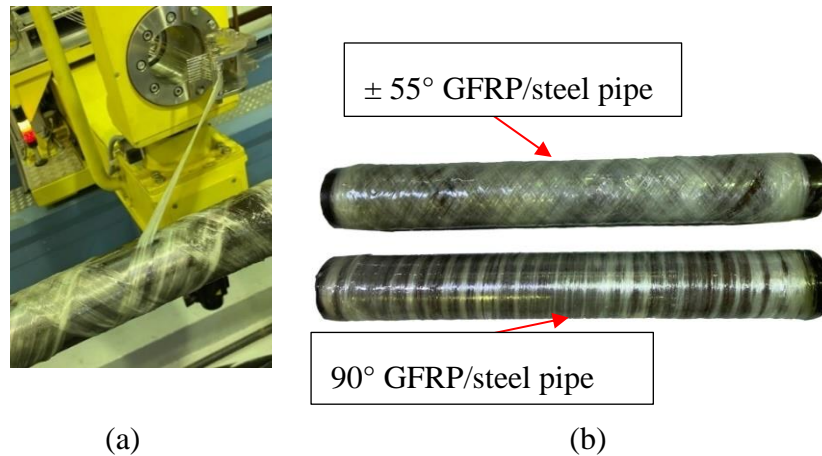
Figure 74. (a) Fabrication of ± 55° FRP layer using 5-axes filament winding machine, (b) ± 55° and 90° FRP/steel pipes.

The layers of glass/epoxy composites were wrapped over the elastic mandrel for the internal reinforcement layer. After being wrapped, the elastic mandrel and the composite layers were inserted inside the pipe and pressurized until perfect bonding between the internal composite and the metallic was achieved (Figure 75). The pipe was then left to cure at room temperature, and when it was cured, the air was released, and the mandrel was pulled from the inside of the pipe.

Figure 75. Steps of fabricating the internal reinforcement layer.

5.2.3 Failure Pressure Prediction Using the Analytical Solution

First, to predict the First-Ply Failure (FPF) pressure of a multi-layered laminated composite/steel pipe, the stresses and strains throughout the laminate must be determined using Classical Lamination Theory (CLT). The result of the stresses and strains obtained is used in the most communal failure theories to predict the overall composite strength. The analysis is carried out to predict the stresses and strains for liner (steel pipe) and composite overwrap and how to relay the pipe's strains to the pressure loading. It is also of interest to calculate the interface pressure P_{if} between the steel pipe and the GFRP layer, the pressure required to cause initial yielding of the liner, P_{yield} and the most important is to calculate the rupture pressure, P_r which is the pressure when the pipe starts to leak or also known as First Ply Failure (FPF) pressure.

Hooke's law, as well as plane stress condition, could be used to relate the stress-strain matrix for the isotropic liner as:

$$\begin{Bmatrix} \sigma_x \\ \sigma_h \\ \tau_{xh} \end{Bmatrix} = [Q_l] \begin{Bmatrix} \varepsilon_x \\ \varepsilon_h \\ \gamma_{xh} \end{Bmatrix} \qquad (21)$$

Where the subscripts x and h stand for the axial and hoop directions, respectively, and

$$Q_l = \begin{bmatrix} \dfrac{E}{1-v^2} & \dfrac{vE}{1-v^2} & 0 \\[2mm] \dfrac{vE}{1-v^2} & \dfrac{E}{1-v^2} & 0 \\[4mm] 0 & 0 & G \end{bmatrix} \quad (22); \qquad G = \dfrac{E}{2(1+v)} \quad (23)$$

While for the FRP composite material in chapter3, Equation (13). The loads on the entire pipe wall can be calculated from the usual thin-walled cylinder equilibrium equations $N_x = pr/2, N_h = pr, N_{xh} = 0$ (24). The strains than can be calculated from:

$$\begin{Bmatrix} \varepsilon_x \\ \varepsilon_h \\ \gamma_{xh} \end{Bmatrix} = A^{-1} \begin{Bmatrix} pr/2 \\ pr \\ 0 \end{Bmatrix} \quad (25)$$

Where A is the extensional-stiffness matrix, $A_{ij} = \sum\limits_{k=1}^{N} \left(\overline{Q}_{ij}\right)_k \left(h_k - h_{k-1}\right)$ (26)

$\overline{Q}$ is the transformed, reduced stiffness matrix and $(h_k - h_{k-1})$ is layer position concerning the middle plane surface. While the stresses in the fiber directions in the

composite layers have been given as $\begin{Bmatrix} \sigma_1 \\ \sigma_2 \\ \tau_{12} \end{Bmatrix} = [Q]\begin{Bmatrix} \varepsilon_1 \\ \varepsilon_2 \\ \gamma_{12} \end{Bmatrix} = [Q][R][T][R^{-1}]\begin{Bmatrix} \varepsilon_x \\ \varepsilon_y \\ \gamma_{xy} \end{Bmatrix}$ (27),

Where the x and y directions are replaced by the x and h direction strains.

[T] is the transformation matrix that relates the local and global stresses to each other,

and it is defined as: $\begin{bmatrix} c^2 & s^2 & 2sc \\ s^2 & c^2 & -2sc \\ -sc & sc & c^2 - s^2 \end{bmatrix}$ (28); where c= cos(θ) and s=sin(θ).

Furthermore, [R] is the Reuter matrix, and it is defined as: $\begin{bmatrix} 1 & 0 & 0 \\ 0 & 1 & 0 \\ 0 & 0 & 2 \end{bmatrix}$ (29)

The interface pressure P_{if} between the liner and the composite can be found by noting

that the liner's stresses (steel pipe) result from the pressure drop across the liner, which is the difference between the internal pressure P and the interface pressure P_{if}. As a ratio to the internal pressure , the interface pressure can be obtained from the hoop stress calculated for the liner.

$$\sigma_h 2t = (p - p_{if})2r \qquad (\,30) \qquad \text{or} \qquad \frac{p_{if}}{p} = 1 - \frac{\sigma_h t}{pr} \qquad (\,31)$$

The yield and burst pressure for the steel could be calculated using Barlow's formula.

$$(P_y = \frac{2 \times S \times T}{OD}) \qquad (\,32)$$

Where: P_y= minimum internal yield pressure (MPa)

S= minimum yield strength (MPa)

T= wall thickness (mm)

OD= outside diameter of the pipe (mm)

5.2.4.1 Pressure at Failure

The rupture pressure is the value of the pressure at which the composite over wrap fails and, in this case, known as the First Ply Failure (FPF) pressure. This approach is based on the first composite layer from inner layers to outer layers as the first ply fails. The five most common failure criteria, Maximum Stress, Maximum Strain, Tsai-Wu, Tsai-Hill, and Hoffman failure theories, were used to predict the FPF pressure to maximize the hybrid pipe strength performance.

5.2.4.1.1 Maximum Stress theory

The maximum stress criterion states that a fiber-reinforced material will fail if the stresses in the principal material coordinate system at any point were equal to or greater

than the corresponding ultimate strength. Thus, to avoid failure,

$$\sigma_1^C < \sigma_1 < \sigma_1^T, \sigma_2^C < \sigma_2 < \sigma_2^T \text{ and } |\tau_{12}| < \tau_{12}^F.$$

Where: σ_1^C Is the compression failure stress in the 1 direction.

σ_1^T Is the tensile failure stress in the 1 direction.

σ_2^C Is the compressive failure stress in the 2 direction.

σ_2^T Is the tensile failure stress in the 2 direction.

τ_{12}^F Is the shear failure stress in the 12 plane.

5.2.4.1.2 Maximum Strain Theory

According to the maximum strain theory, failure occurs when any strain in the principal material directions is equal to or greater than the corresponding ultimate strain. Thus, to avoid failure,

$$\varepsilon_1^C < \varepsilon_1 < \varepsilon_1^T, \varepsilon_2^C < \varepsilon_2 < \varepsilon_2^T \text{ and } |\gamma_{12}| < \gamma_{12}^F.$$

Where: ε_1^C Is the compression failure strain in the 1 direction.

ε_1^T Is the tensile failure strain in the 1 direction.

ε_2^C Is the compressive failure strain in the 2 direction.

ε_2^T Is the tensile failure strain in the 2 direction.

γ_{12}^F Is the shear failure strain in the 12 plane.

5.2.4.1.3 Azzi–Tsai–Hill Theory

Azzi and Tsai [193] proposed that failure occurs in an orthotropic lamina if and when the following equation is satisfied:

$$\frac{\sigma_1^2}{\sigma_1^{T\,2}} - \frac{\sigma_1\sigma_2}{\sigma_1^{T\,2}} + \frac{\sigma_2^2}{\sigma_2^{T\,2}} + \frac{\tau_{12}^2}{\tau_{12}^{F\,2}} = 1 \qquad\qquad (33)$$

5.2.4.1.4 Tsai–Wu Failure Theory

Tsai–Wu failure theory [194] predicts failure in an orthotropic lamina if and when the following equation is satisfied:

$$F_1\sigma_1 + F_2\sigma_2 + F_6\tau_{12} + F_{11}\sigma_1{}^2 + F_{22}\sigma_2{}^2 + F_{66}\tau_{12}{}^2 + 2F_{12}\sigma_1\sigma_2 = 1 \qquad (34)$$

Where F1, F2, and so on are called the strength coefficients and are given by:

$$F_1 = \frac{1}{\sigma_1^T} - \frac{1}{\sigma_1^C} \;,\; F_2 = \frac{1}{\sigma_2^T} - \frac{1}{\sigma_2^C} \;,\; F_6 = 0 \;,\; F_{11} = \frac{1}{\sigma_1^T\sigma_1^C} \;,\; F_{22} = \frac{1}{\sigma_2^T\sigma_2^C} \; \text{and} \; F_{66} = \frac{1}{\tau_{12}^{F\,2}} \; (35)$$

5.2.4.1.5 Hoffman Failure Theory

Hoffman had developed an equation for especially brittle material inspired by the Tsai-hill failure criterion where it can be expressed in the following form:

$$-\frac{\sigma_1^2}{\sigma_1^T\sigma_1^C} + \frac{\sigma_1\sigma_2}{\sigma_1^T\sigma_1^C} - \frac{\sigma_2^2}{\sigma_2^T\sigma_2^C} + \frac{\sigma_1^T+\sigma_1^C}{\sigma_1^T\sigma_1^C}\,\sigma_1 + \frac{\sigma_2^T+\sigma_2^C}{\sigma_2^T\sigma_2^C}\,\sigma_2 + \frac{\tau_{12}^2}{\tau_{12}^{F\,2}} = 1 \qquad (36)$$

5.2.4 Experimental Hydraulic Pressure Test

According to ASTM, internal pressure capacities of steel pipes, FRP/steel, steel/FRP, and FRP/steel/FRP pipes were tested using Resato high-pressure machine model SPU-CC-2000 D1599 (Figure 76). The pressuring device consists of a hydrostatic pressure pump to apply maximum pressure of 2000 bar. Internal pressure tests were conducted under a closed-loop control system to ensure safety. The pressure test was divided into two main stages. Stage one is the filling process, in which the machine fills the GFRP pipe with the oil at 5 bars. Stage two is pressurizing process, where the pressure increased continuously and uniformly up to pipe failure, where the applied pressure and

111

elapsed time were recorded.

<p align="center">(a)   (b)</p>
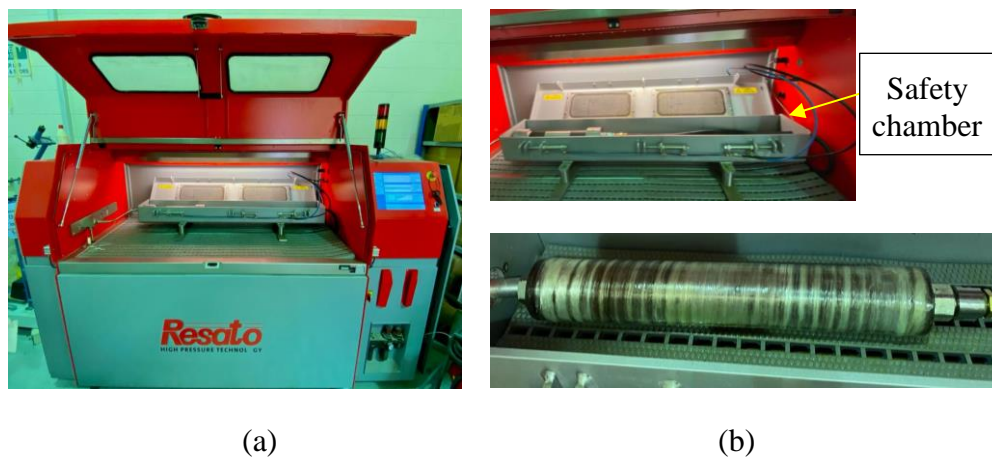
Figure 76- (a) SPU-CC-2000 Resato high-pressure machine, (b) FRP/steel pipe installed for testing.

5.3 Results and Discussion

5.3.1 Analytical Results

Table 16 presents the plane stresses in each FRP layer in the global coordinate system (x,y). The laminate input loads N_x, N_y and N_{xy} were calculated using equation (24) under internal pressure of 1 bar, where the presented stresses could be used to predict the first ply failure layer. By analyzing the data in Table 16, it could be concluded that the outermost GFRP layer will be the first layer to fail in all the pipes that have overwrapped GFRP layers; Figure 77 presents details for the hybrid pipe layers.
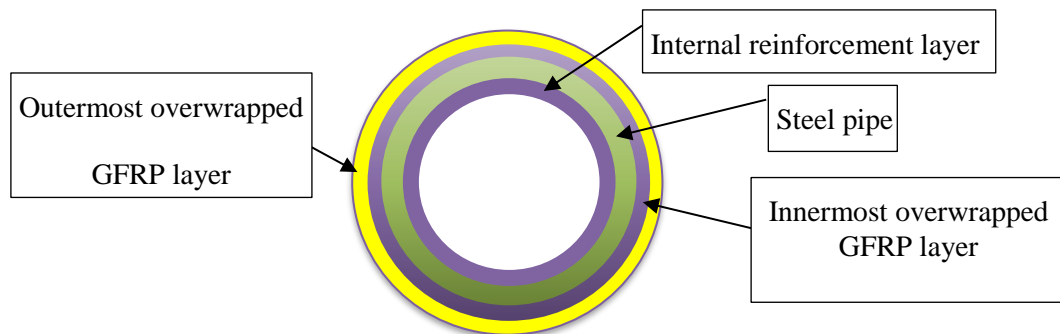
Figure 77. schematic for the GFRP/steel/GFRP hybrid pipe.

Table 16. Stress carrying capacity in each layer under internal pressure of 1 bar.

Specimen ID	Outermost GFRP layer			Innermost GFRP layer			Internal reinforcement		
	σ_x MPa	σ_y MPa	τ_{xy} MPa	σ_x MPa	σ_y MPa	τ_{xy} MPa	σ_x MPa	σ_y MPa	τ_{xy} MPa
Steel/GFRP$_o$± 55°	0.365	0.768	-0.268	0.336	0.695	0.339	____	____	____
Steel/GFRP$_o$9 0°	0.252	0.924	6.1e-4	0.178	0.689	4.9e-4	____	____	____
GFRP$_{in}$/steel/ GFRP$_o$ ±55°	0.148	0.317	-0.116	0.149	0.314	0.147	0.043	0.120	-0.005
GFRP$_{in}$/steel/ GFRP$_o$ 90°	0.094	0.380	2.5e-4	0.075	0.342	2.7e-4	0.024	0.138	5.5e-5
GFRP$_{in}$/steel	____	____	____	____	____	____	0.160	0.401	1.7e-4

5.3.2 Experimental Results

Figure 79. presents the pressure capacity of the steel, steel/GFRP, GFRP/steel, and GFRP/steel/GFRP pipes with different fiber winding angles. The unwrapped steel pipes were internally pressurized until they burst and were used as control specimens. It is recognized that the GFRP/steel/GFRP ± 55° can sustain the highest internal pressure before failing. Internally pressurizing the GFRP/steel pipes causes the metallic pipe to yield while the composite remains elastic. Failure of the composite layer is usually initiated by matrix cracking. The failure propagates with additional matrix failure with the increase of pressure. The glass fiber reinforced metallic pipe was tested by gradually increasing the internal pressure. Adding internal reinforcement results in increasing the internal pressure capacity because of the decrease in diameter and increase in thickness, where $p = \frac{2t\sigma}{d}$ (37).

Figure 78 shows the damage and failure nature of steel and GFRP/steel/GFRP pipes

with different winding angles. It could be noticed that the burst pipes experience an apparent increase in the diameter before failure result of the well-known ductile damage behavior of steel. The overwrapped GFRP layers had a significant effect on limiting the change in pipe diameter, especially for the ±55° winding angle because of the crossed layers behavior where it is much more difficult for the filaments to slip contrary to what happens in the FRP layers with 90° winding angle (clear filament slipping in the burst mode of GFRP /steel/GFRP 90° pipe) as shown in Figure 78-c, where it could be observed from Figure 79 that Δd decreased from 2.1 mm in the conventional steel pipe to 0.9 mm in the GFRP/steel/GFRP ±55° pipe. The internal reinforcement also affected the decrease of Δd by 0.3mm.

(a)	(b)
(c)	(d)
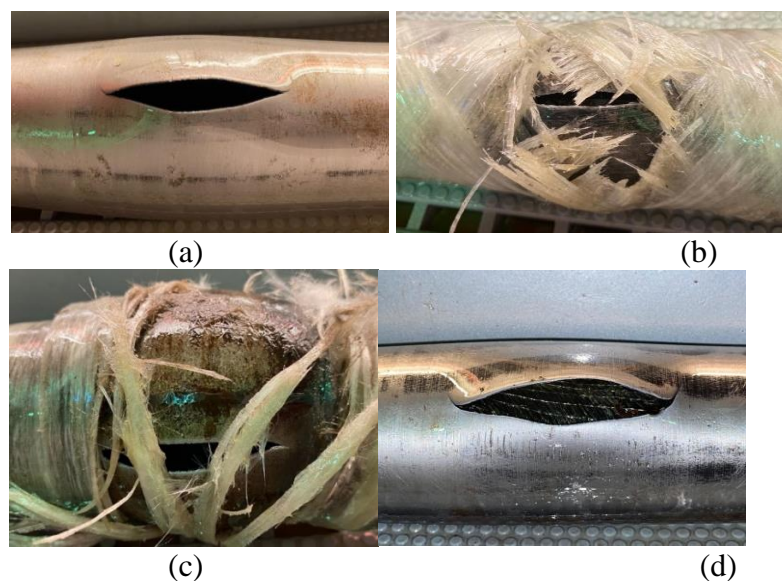
Figure 78. Burst mode of internally pressurized (a) steel (b) GFRP /steel/GFRP 55° (c)GFRP /steel/GFRP 90° (d) GFRP/steel pipes.
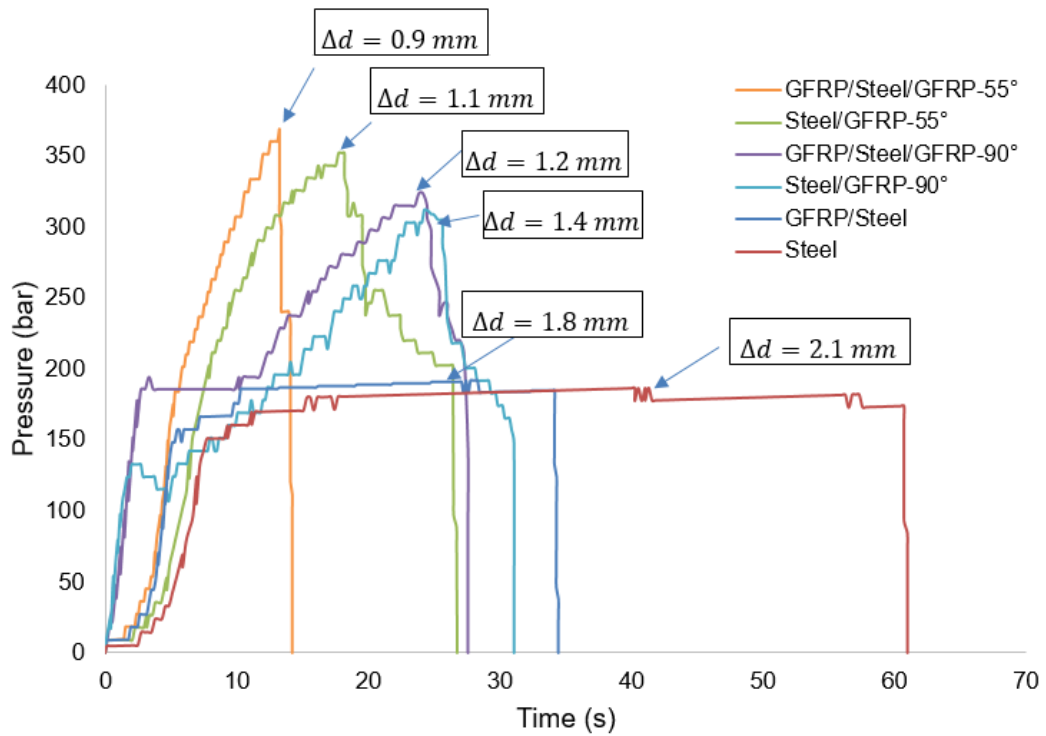
Figure 79. Pressure capacity versus time for steel, GFRP/steel, and GFRP/steel/GFRP pipes.

5.3.3 Overall Discussion

Table 17 presents the burst pressure and first ply failure pressure data for the hybrid FRP/steel, FRP/steel/FRP, and steel/FRP pipes. For the analytical data, five different failure theories were employed to identify the status of stress components at which first ply failure happens. The shear, tensile, and compressive stresses in the axial and hoop directions could be identified from the failure theories. The failure pressure presented in Table 17 was calculated using the FPF stress in the hoop direction using equation (37), since the stresses in the hoop direction are much higher than the shear stresses and the stresses in the axial direction, as shown in Table 16. While for the steel pipe, the yield and burst pressure were calculated using equation (32), using the yield strength and ultimate tensile strength presented in Table 15 for the ASTM-A53 steel alloy.

Table 17. Experimental and analytical failure data for the hybrid FRP/steel pipes.

Specimen ID	Experimental data	Analytical data -First Ply Failure pressure (FPF) using different failure theories				
	Burst Pressure (bar)	Max Stress (bar)	Max Strain (bar)	Tsai-Hill (bar)	Hoffman (bar)	Tsai-Wu (bar)
Steel/GFRP$_o$±55°	352	281	276	272	272	272
Steel/GFRP$_o$90°	308	315	316	316	316	316
GFRP$_{in}$/steel/GFRP$_o$ ±55°	369	177	176	174	174	174
GFRP$_{in}$/steel/GFRP$_o$ 90°	323	193	194	195	195	195
GFRP$_{in}$/steel	192	294	296	298	298	298
Steel	186	$P_{yield} = 120$ bar, $P_{burst} = 207$ bar using equation (32)				

5.4 Summary

This chapter proposed a corrosion-free hybrid pipe, which improved the pipeline's pressure capacity. Analytical and experimental failure data were presented in detail. The five most common failure criteria were used to predict the FPF pressure to maximize the hybrid pipe strength performance. The internal pressure capacity of steel, GFRP/steel, and GFRP/steel/GFRP composite pipes was tested using Resato high-pressure machine model SPU-CC-2000 ASTM D1599 standard. The external GFRP composite layers were wound at an angle of ± 55° and 90° using a computerized 5-axes filament winding machine. The novelty of the current research was the internal reinforcement fabrication. An elastic mandrel was used for this purpose. In addition to the fact that the produced pipes are corrosion-free, the testing results showed significant

improvement in the internal pressure capacity and a limitation in the change of diameter compared to the conventional steel pipes.

CHAPTER 6: ELECTROCHEMICAL EVALUATION OF FIBER REINFORCED

POLYMER SYSTEMS AGAINST CORROSION OF PIPELINE STEEL

6.1 Introduction

Worldwide, corrosion is counted as the most critical reason for materials failure [1].

Various coating types are believed to be reasonable solutions to protect pipeline

surfaces against corrosion [2]. However, some unsolved problems currently limit the

application of organic coatings such as pores, cracks, and scratches, in addition to

various damages that may destroy the protective barrier, leading to expose the bare

metal to the corrosive environment [3]. The degradation process of polymeric coatings

is scientifically known as a micro separation process with the enlargement of sub-

molecular structures, leading to deficient coating systems [4]. The utilization of epoxy

coatings, especially in high-performance applications, is mainly limited because of their

high rigidity and minimal impact strength. Many investigations have been performed

over the last decades in an attempt to build up a procedure or process that would grant

substantial enhancements in toughness achieved at minimal loss of mechanical

properties and a low cost [5].

Many researchers studied the corrosion-resistant behavior of different epoxy coatings

over steel surfaces. As the Epoxy zinc-rich coating [6] [7] [8][9][10], epoxy coating

reinforced with aluminum pigments or aluminum powder [11][12], and magnesium-

rich epoxy coating[13] since zinc and aluminum, and magnesium are metals that can

be used as sacrificial anodes [14]. Also, another type of epoxy coatings that gained the

interest of researchers is the epoxy-containing glass flakes [15][16][17]. The major

problem in these epoxy coating types is the high reinforcement content. For example,

around 85% of metallic zinc content is essential to guarantee the electrical contact

between zinc and steel substrate to deliver adequate cathodic protection [18]. This high content would result in poor mechanical properties, which would reduce the applied coating's service lifetime. Previous researches have shown that steel/ fiber-reinforced polymer (FRP) hybrid pipes are the best alternatives for steel pipes [19], and they are widely used in petroleum and chemical engineering industries [20]. The use of FRP composite materials to protect the steel pipes results in many advantages; it is cheap, lightweight [21], quick-procedure, corrosion-resistant, and impart extra strength and internal pressure capacity to the pipe [22][23][24]. Numerous investigations have been launched recently to present the effect of acidic and corrosive media on the corrosion behavior and deterioration mechanisms of FRP materials [25][26][27][28][29]. The studies indicated that there are considerable differences between the properties of initial and aged specimens. Due to specific environmental conditions, FRP materials' degradation has become a significant issue because of its economic consequences [30][31]. The mechanisms of these critical changes involve the degradation of all composite components, namely matrix, fibers, and their interface [32][33]. This research evaluates the electrochemical behavior of FRP systems against corrosion of carbon steel pipes, where the FRP layer strengthens the pipe in addition to the protection against corrosion. Two different fiber types were investigated, namely glass and Kevlar fibers with an epoxy resin matrix, compared to pure epoxy coating and conventional non coated steel.

6.2 Materials and Methods

6.2.1 Materials

Cleaned EN10130 carbon steel sheet specimens with a thickness of 1.5 mm, length of 8 cm, and width of 4 cm were used as a substrate for epoxy coatings and FRP layers. The chemical composition for the EN10130 carbon steel sheet is presented in Table 18.

The specimens were ground using different abrasive papers, up to 1200 grits, to improve the epoxy and FRP layers' adhesion with the steel surface and reduce the delamination. Then the specimens were washed with water, degreased in acetone, washed again with water, and dried with air.

Table 18. Chemical composition of the EN10130 carbon steel sheet.

	C	Mn	P	S	Si
99.09	0.12	0.6	0.045	0.045	0.1

Four types of specimens were prepared (Figure 80). The first type is the control sample, the non-coated steel specimen, referred to as the exposed substrate. The second type is the epoxy-coated steel specimen and will be referred to as epoxy/steel. The third and fourth types consist of glass fiber/epoxy, and Kevlar fiber/epoxy layers added on top of the steel specimens and referred to as GFRP/steel and KFRP/steel. The polymeric matrix comprises 100 parts of the epoxy resin (EL2) and 30 parts mass of curing agent (AT30). The prepared specimens were left for 48 hours at room temperature to cure. The average thickness of the epoxy coating and FRP composite layers in all the specimens was 0.5 mm±, consisting of one layer. Figure 2 presents the SEM images for the cross-section of the prepared specimen's thickness.

(a)   (b)   (c)   (d)
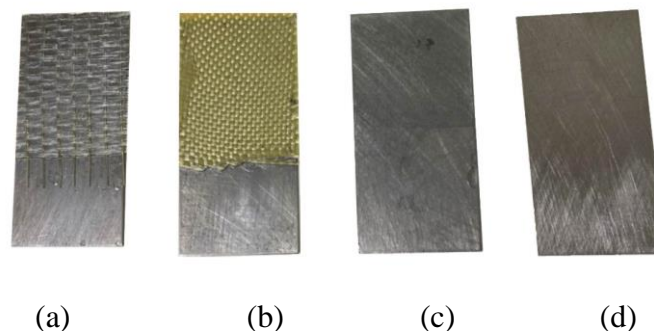
Figure 80. Prepared Specimens (a) GFRP/steel (b) KFRP/steel (c) Epoxy/steel (d) non-coated steel.

	Kevlar/epoxy-Steel	Glass/epoxy-Steel	Epoxy-steel
Cross-section for thickness	KFRP Steel	GFRP Steel	Epoxy Steel
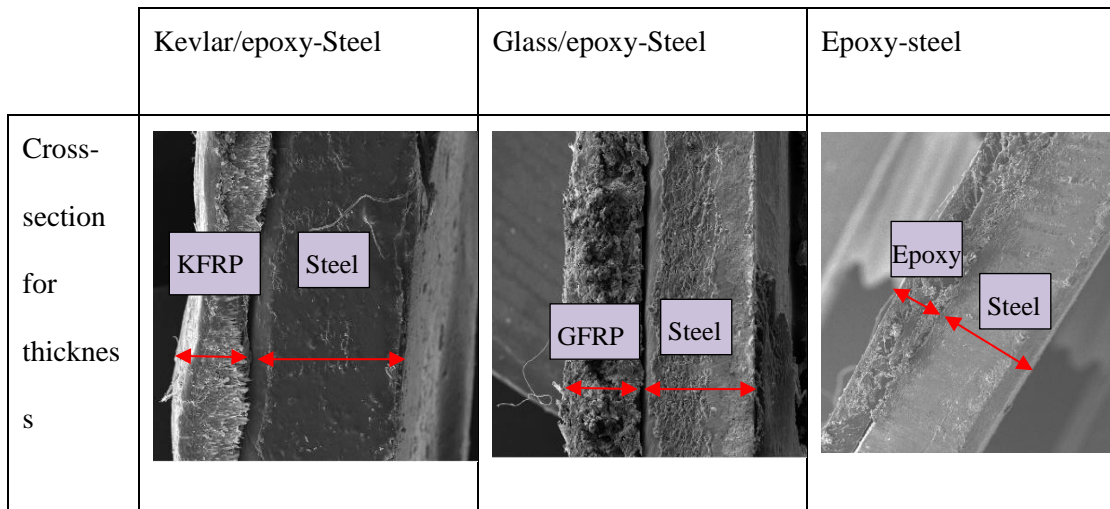
Figure 81. Cross-sectional SEM images for the prepared specimen's thickness.

6.2.2 Methods

2.2.1 Potentiodynamic Polarization (PDP) and Electrochemical Impedance Spectroscopy (EIS)

The potentiodynamic polarization testing is used to evaluate the kinetic data of the corrosion current densities' variation representing the corrosion rate and the corrosion potentials. Also, the testing provides information about the nature of the anodic reactions, the cathodic reactions, and passivity [34]. These are all beneficial when assessing the corrosion properties. The prepared specimens were subjected to a potentiodynamic polarization scan within the potential range of -1.2 V to 0.5 V (SCE). EIS is a testing that is utilized to quantify the impedance of coatings to corrosion and study the nature of the interfacial interactions for the coated systems to evaluate the interactions near the steel substrate to the solution [35].

The four sets of the developed specimens were immersed in 0.5M NaCl, 0.5M HCl, and 0.5M H_2SO_4 solutions to study their anticorrosion behavior. The EIS study was executed at open circuit potential (OCP) within frequency range 0.2 Hz to 100000 Hz, where OCP is used to evaluate the dominance of the anodic reactions versus the cathodic reactions and their variation with time about the nature of the coating system

and environmental conditions and will give information about the stability of the electrochemical system. All the electrochemical tests were conducted using a GAMRY 3000 potentiostat (Figure 82). A potentiostat is an electronic instrument that monitors the difference in voltage between the reference and working electrode by injecting current into the cell through the counter electrode.
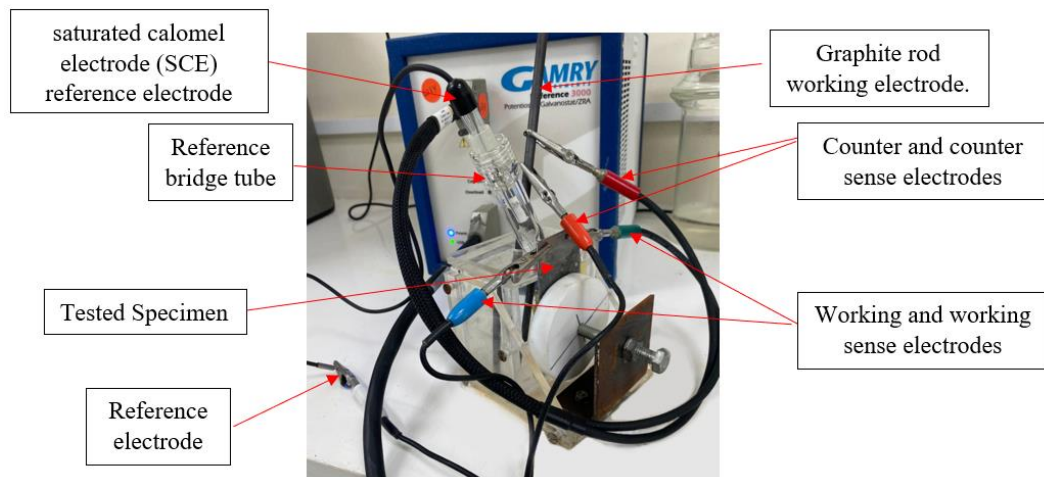
Figure 82. The electrochemical cell setup.

6.3 Results and Discussion

6.3.1 OCP/Potentiodynamic Polarization

The samples, exposed substrate, glass/epoxy, Kevlar/epoxy, and epoxy systems were immersed for 25 hours in the testing solutions of 0.5 M NaCl, 0.5 M HCl, and 0.5 M H_2SO_4. The open-circuit potentials' variations were monitored (across were also the electrochemical impedance spectroscopy discussed in another section). The potentiodynamic polarization scans were carried out at the end of immersion. This test evaluated the corrosion resistance, corrosion kinetics, passivation, and cathodic reactions in correspondence to the coating systems and testing solutions. The tests offered findings on the feasibility of using a coating type in mild and severe environmental conditions.

The OCPs, in Figure 83, indicated noticeably decelerated anodic activity of the substrate when coated, of higher OCPs than the exposed substrate in all states. The glass/epoxy system exhibited better corrosion/deterioration resistance than the Kevlar/epoxy system in acidic solutions. Kevlar/epoxy system interestingly showed evidence of deterioration in the H_2SO_4 solution to exhibit OCPs comparable to those of exposed substrate after nearly 50 ks. Epoxy alone seemed to demonstrate corrosion resistance intermediate between Kevlar/epoxy and Glass/epoxy systems. The potentiodynamic scans of the coated systems, in Figure 84, indicated a comparable polarization response in the anodic reactions, cathodic reactions, and passivation. No solution showed more significant influence than others, and no coating system showed more significant corrosion resistance than others. The corrosion rates were less than 1 million to 10 million times than exposed substrates. Agreeing with the OCPs, the glass/epoxy system had high corrosion potentials, and the Kevlar/epoxy system had low corrosion potentials, indicating the decelerated anodic activity and effectiveness of glass/epoxy accordingly. In the long run, in acidic conditions, glass promotes, and Kevlar lessens corrosion resistance, respectively. This result is exhibited from the instability of the Kevlar/epoxy layer at the end of the experiments in acidic conditions.
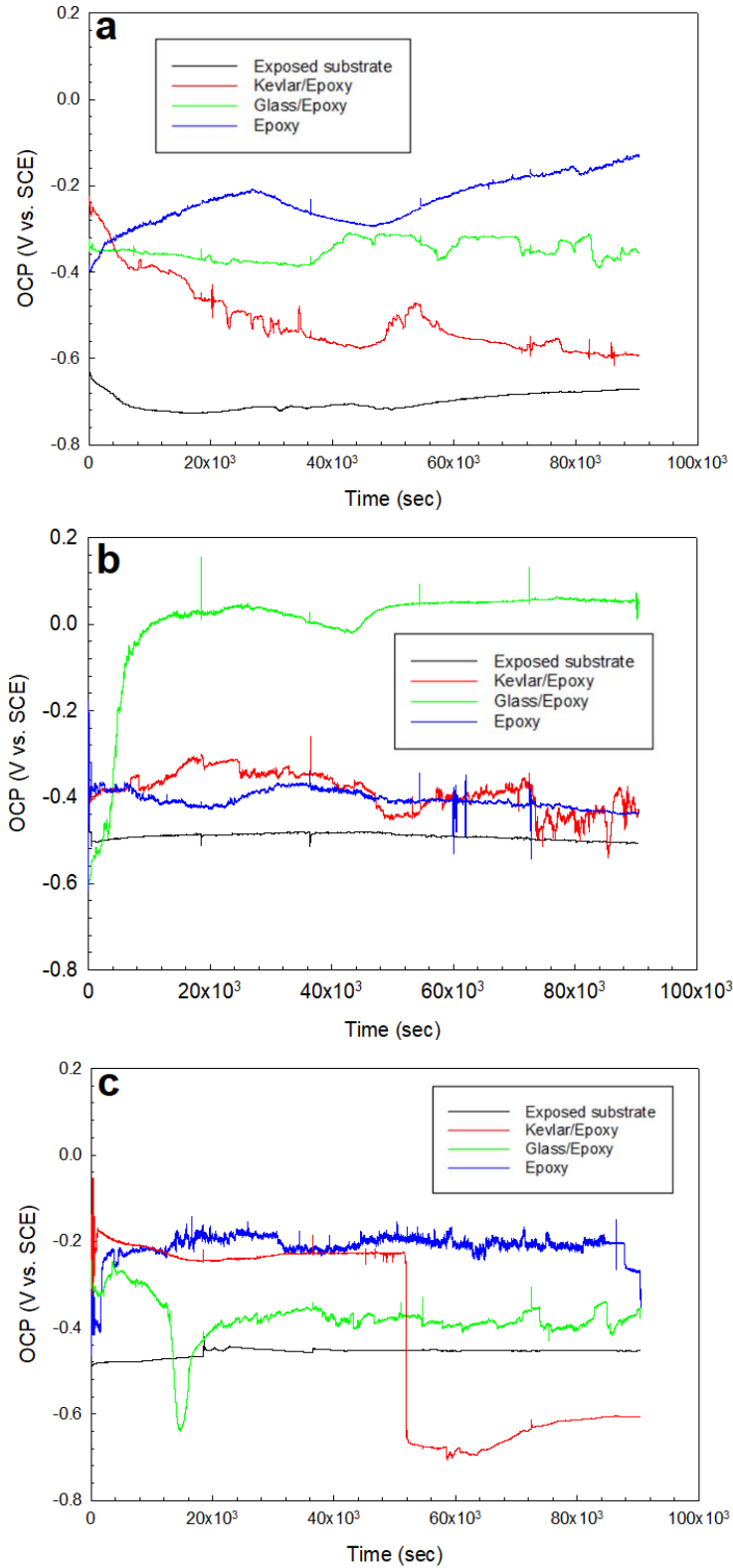
Figure 83. Open-circuit potentials in a) 0.5 M NaCl, b) 0.5 M HCl, and c) 0.5 M H$_2$SO$_4$ solutions of exposed substrate, and glass/epoxy, Kevlar/epoxy, and epoxy systems.
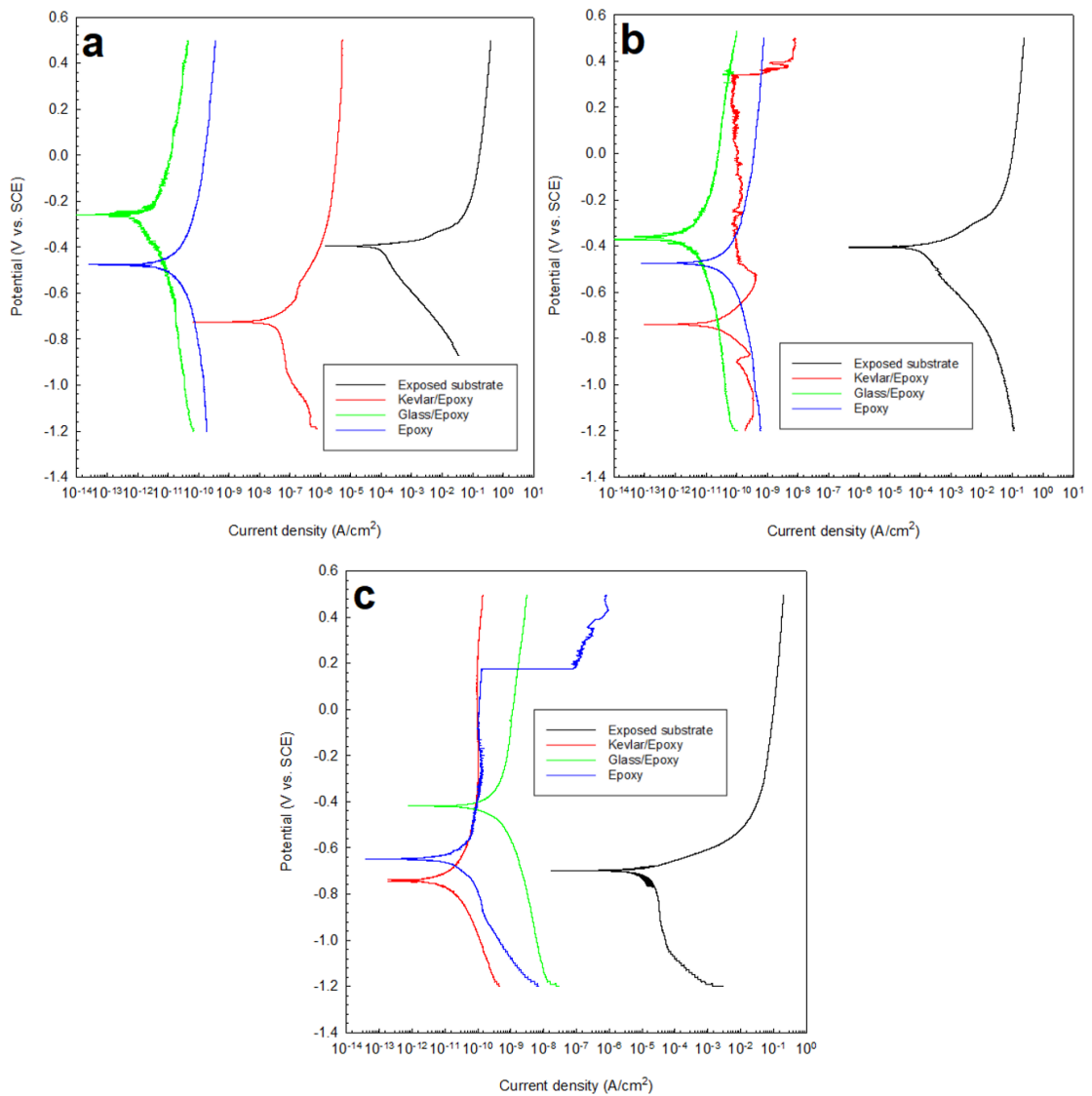
Figure 84. Potentiodynamic polarization in a) 0.5 M NaCl, b) 0.5 M HCl, and c) 0.5 M H2SO4 solutions of exposed substrate, and glass/epoxy, Kevlar/epoxy, and epoxy systems.

The relative agreement between the OCPs and E_{corr} values is manifested in Figure 85. The high E_{corr} values in the exposed substrate's acidic conditions pertain to the high rate of cathodic reactions. It should be noted from Figure 4 that during passivation, unlike the glass/epoxy system, the epoxy alone and epoxy/Kevlar system showed instability manifested in the abrupt increase in passive currents at nearly between 0.2 and 0.4 V vs. SCE in acidic solutions.
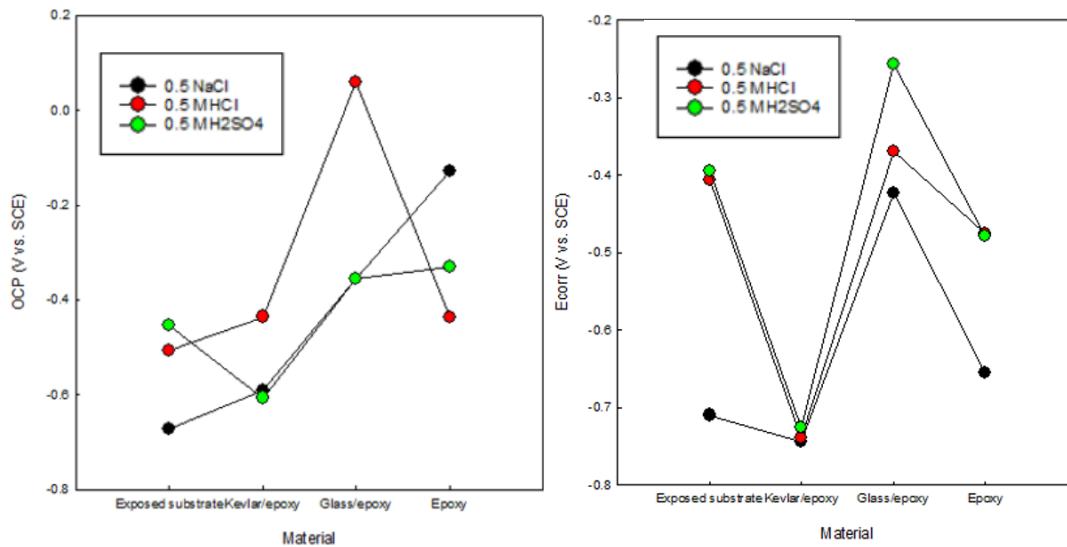
Figure 85. Open-circuit potentials and corrosion potentials of 0.5 M NaCl, 0.5 M HCl, and 0.5 M H2SO4 solutions of the exposed substrate, and glass/epoxy, Kevlar/epoxy, and epoxy systems

6.3.2 Electrochemical Impedance Spectroscopy (EIS)

The electrochemical impedance spectroscopy response has been monitored across the periods of 5, 10, 15, 20, and 25 hours of free immersion in 0.5 M NaCl, 0.5 M HCl, and 0.5 M H2SO4 for the steel surface and surfaces coated with glass/epoxy, Kevlar/epoxy, and epoxy systems. The purpose was to i) evaluate the nature of the interfacial interactions onto the protective epoxy-based systems, across them, and beneath them at steel/layer interface, ii) mechanisms of corrosion and mass transport, iii) deterioration of the epoxy or FRP, iv) distribution of the anodic and cathodic reactions, with time, and about the environmental conditions and physical properties of the layer system, and comparison, to the response of a steel substrate without protection. Also, the results were used to corroborate the kinetic results of the OCP and potentiodynamic polarization. Regardless of the solution (medium-pH (0.5 M NaCl) or low-pH (0.5 M HCl and 0.5 M H2SO4)), the anodic reaction involves the dissolution of the steel substrate to form ferrous ions. Those ions migrate and accumulate first within possible

pores reacting with hydroxide and O2 to form iron hydroxide (Fe(OH)2), iron carbonate (FeCO3), and iron oxides (Fe2O3 and Fe3O4) [36]. However, the anodic reaction proceeds at different rates depending on pH and the nature of the interfacial protection used. The dissolution might remain underneath the protective layer because of the partial, with-time pore-like deterioration of the epoxy, causing the immersion solution to reach the substrate. Or to result in corrosion products that fill the pores, weaken further the epoxy (being weakened already from the solution), accumulate out of the epoxy layer, and partially cover it. These drawbacks affect the corrosion protection in suppressing both the anodic and cathodic reactions. They also affect the distribution of the anodic versus the cathodic reactions with time, leading to a change in the overall mechanism that controls the interfacial interactions. The significance of the cathodic reactions that involve the reduction of hydrogen is much higher in HCl and H2SO4 solutions than in NaCl solutions. The anodic dissolution with time becomes high as a result of time.

Figure 7 and Figure 88 presents the Nyquist and bode plots together that are used to explain the interactions and their physical effects on the substrate and protective layer with time. In all solutions, regardless of the physical conditions at the interface (bare surface or coated), the interactions proceeded with the exact mechanism and a time-independent fashion. The equivalent circuit of the configuration {R(Q(R(QR)))} achieved fitting to the experimental data across the entire frequency range, from the high (charge transfer and surface interface) to the low (epoxy layer and bulk solution). The suitability of the equivalent circuit to the bare steel surface pertained interestingly to the developing corrosion products, which with time achieved significance similar to an original protective layer. To account for the heterogeneities, the capacitance of the double layer, corrosion products, and coating system was calculated as a constant phase

element (CPE), with admittance expressed as [37].

$$Y = Y_Q\,\omega^n cos\left(\frac{n\pi}{2}\right) + jY_Q\omega^n sin\left(\frac{n\pi}{2}\right) \qquad\qquad (38)$$

Where: ω is the angular frequency, and n is the CPE exponent.

The equivalent electrical circuits are fitted by Gamry Echem Analyst software. Figure 86 presents the electrochemical equivalent, electric circuit models, fitting the bare steel specimens' impedance data and the coated steel specimens. The data extracted from the fitting is presented in Appendix A. The schematics demonstrate the change in the coating system that results either in corrosion resistance enhancement or decrease. R_s is the solution resistance, R_c is the coating resistance, R_{ct} is the charge transfer resistance, Q_c is the coating capacitance, and Q_{dl} is the double-layer capacitance.
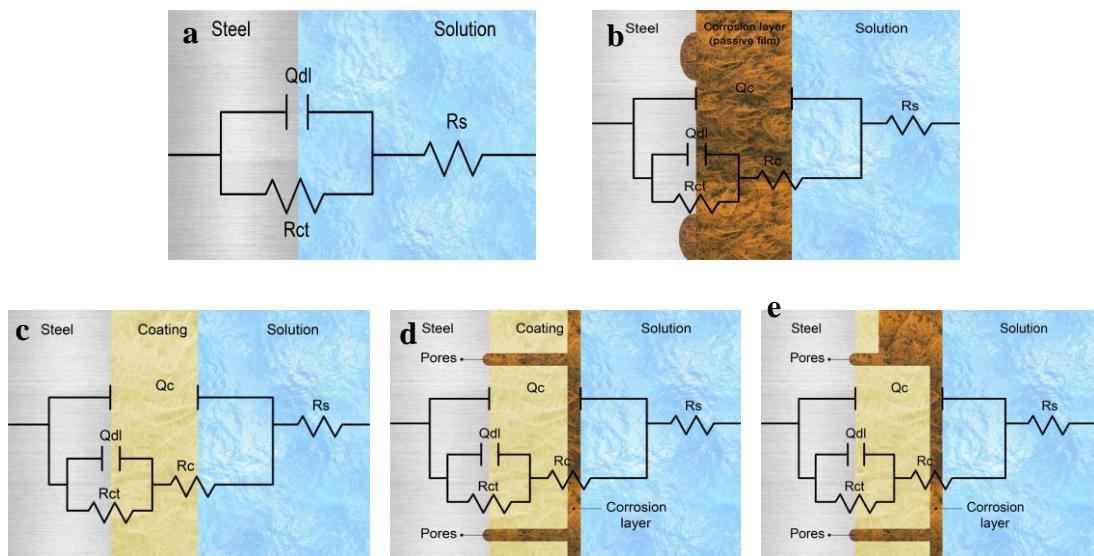
Figure 86. Electrochemical equivalent electric circuit models obtained from fitting the impedance data; (a) bare steel before corrosion (b) corroded bare steel (c) coated steel (d) enhanced corrosion resistance (e) decreased corrosion resistance.

6.3.2.1 EIS in 0.5 M NaCl Solutions

EIS response represented in Nyquist and Bode profiles in 0.5 M NaCl solutions is outlined in Figure 7 and Figure 8 regarding the exposed steel, glass/epoxy,

Kevlar/epoxy, and epoxy systems. From the fitting of the data with the equivalent circuit in the previous section, the interactions with time did not change in governing mechanism. Besides, the interactions were independent of the nature of the epoxy system used. The behavior change was primarily governed by the changes the epoxy systems underwent and the corrosion products' evolution in affecting the charge transfer resistance at the protective layer's double layer and corrosion resistance. In the glass/epoxy system, the corrosion resistance increased from nearly 8 MΩ.cm2 to 16 MΩ.cm2, indefinitely with time. The admittance did not change 190×10^{-12} $S.s^n/cm^2$, with exponent n values of nearly 0.7 at the double layer. This result indicated the passive film's significance in enhancing the protectiveness in a pseudocapacitive manner, with pores continuously filled with protective film. The Kevlar/epoxy system, in agreement with the OCP and polarization data, showed the least corrosion resistance, which was decreasing with time, from nearly 6.5 $M\Omega.cm^2$ to 30 $k\Omega.cm^2$, with higher admittance (that did not change with time) of nearly 150×10^{-12} $S.s^n/cm^2$. This result underlines the deterioration of the Kevlar-based epoxy layer, thinning for greater permeation of the chloride and hydroxyl ions to accelerate the deterioration of the substrate's layer and dissolution and formation of porous passive films. The epoxy only layer exhibited a continuously decreasing corrosion resistance before it increased at the end of testing, indicating its reliability against corrosion in the long run without interference from glass or Kevlar. Its permeability was interestingly the least, and the capacitance across the double layer and the epoxy layer was more capacitive than the glass/epoxy and Kevlar/epoxy systems. From the bode diagrams, the phase peaks did not change in values or shift in frequency with time, indicating the single-phase constant response and similarity in governing mechanisms of interactions. The peaks of glass-epoxy and epoxy systems indicated reliability against activity at both the

double and coating layers, appearing at frequencies of two orders of magnitude higher than those of the Kevlar-epoxy system. In comparison, the EIS response of the steel substrate was more capacitive, two-time constant based, of much lower resistance at the double layer and the passive film layer (whose resistance increased with time). This result outlines the superior advantage of the coating systems utilized in the chloride solutions.

Figure 87. EIS Nyquist plots of 0.5 M NaCl solution of a) exposed steel, b) glass/epoxy, c) Kevlar/epoxy, d) epoxy systems.
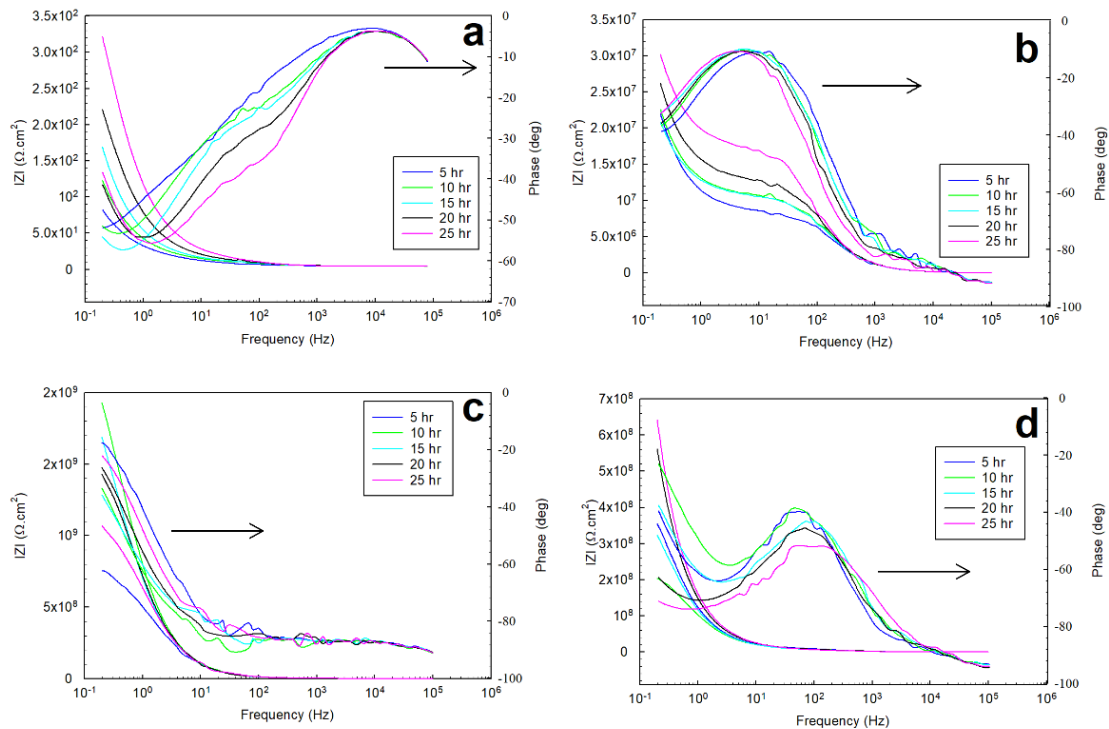
Figure 88. EIS bode plots of 0.5 M NaCl solution of a) exposed steel, b) glass/epoxy, c) Kevlar/epoxy, d) epoxy systems.

6.3.2.2 EIS in 0.5 M HCl and 0.5 M H₂SO₄ Solutions

In the acidic solutions, the EIS response underwent the exact governing mechanism of interfacial interactions that governed the NaCl solutions' coated systems (mild pH). The dominance and rate of the cathodic reactions of the direct reduction of hydrogen protons onto and across the coated systems' diffusion channels were higher, at variant times at the beginning of the immersion. Over time, this incentivized the anodic dissolution, passivation, and partial weakening or partial deterioration of the coating layer. The Nyquist profiles of 0.5 M HCl and 0.5 M H$_2$SO$_4$ solutions in Figure 89 and Figure 91 indicate the relatively higher capacitance of the interactions across both the low and high-frequency ranges. The variations in overall capacitance in the two solutions reflected the competitive, opposing kinetics of the hydrogen evolution and passive films' formation. In HCl solutions, the glass-epoxy system's resistance was the highest,

nearly 7 GΩ.cm^2, although showing a steady decrease with time to as low as 0.2 MΩ.cm^2. The Kevlar-epoxy system, on the contrary, had less resistance. Still, it increased with time with fluctuations from 45 kΩ.cm^2, to 0.5 MΩ.cm^2, to 4 MΩ.cm^2, underlining Kevlar's significance in promoting the formation of passive films that with time decelerate the dissolution and the significance of glass in stabilizing the epoxy system that initially was protecting the system. Interestingly, the epoxy-only system, in the long run, did not show a net change in the resistance; it increased only after 10 hours to decrease steadily back to nearly the initial resistance values of charge transfer and protective layer of nearly 1.2 MΩ.cm^2. The epoxy only layer exhibited comparable reliability to that of the glass-epoxy against corrosion towards the experiment's total time.
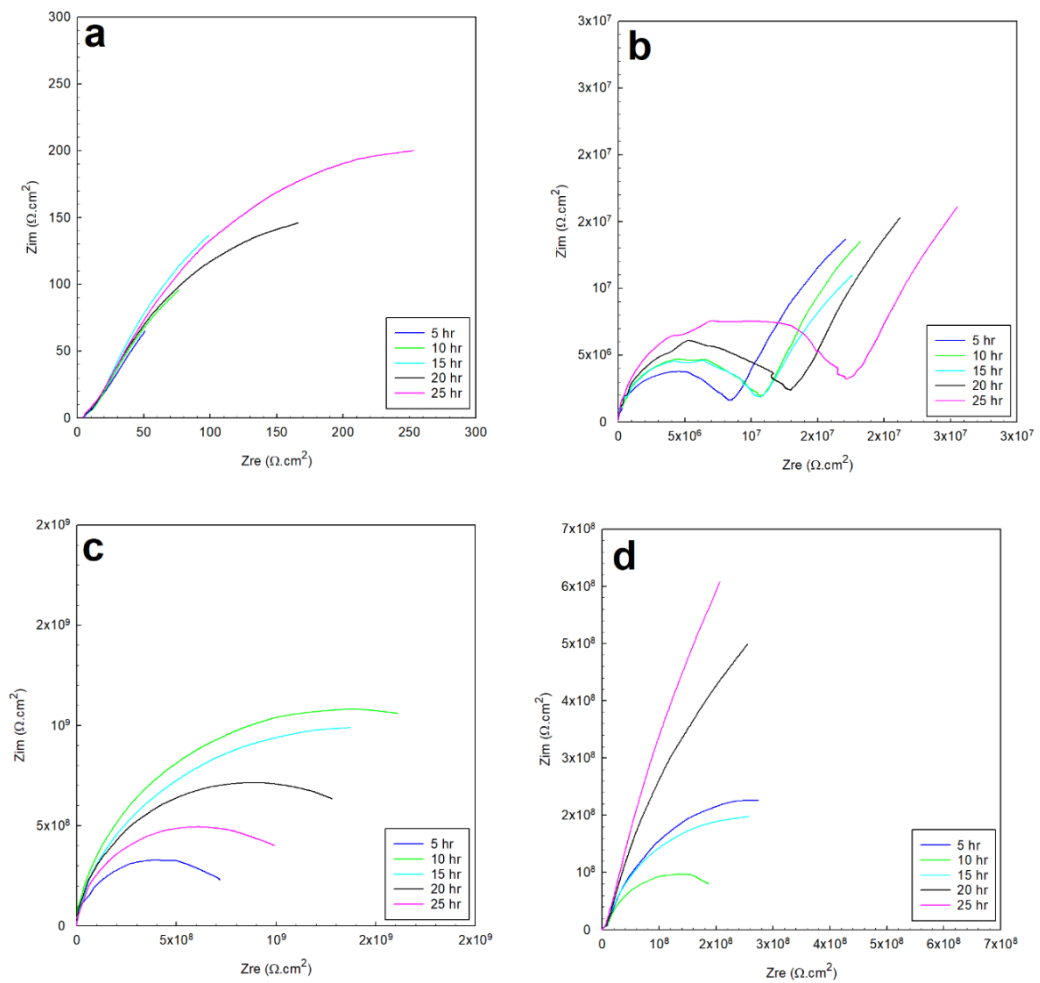

Figure 89. EIS Nyquist plots of 0.5 M HCl solution of a) exposed steel, b) glass/epoxy, c) Kevlar/epoxy, d) epoxy systems.

The phase peaks in Figure 90 indicated that the single-time-constant-based interactions were similar regardless of the coating systems, with peaks associated with interactions at hydrodynamic layers away from the coating system at low frequencies.
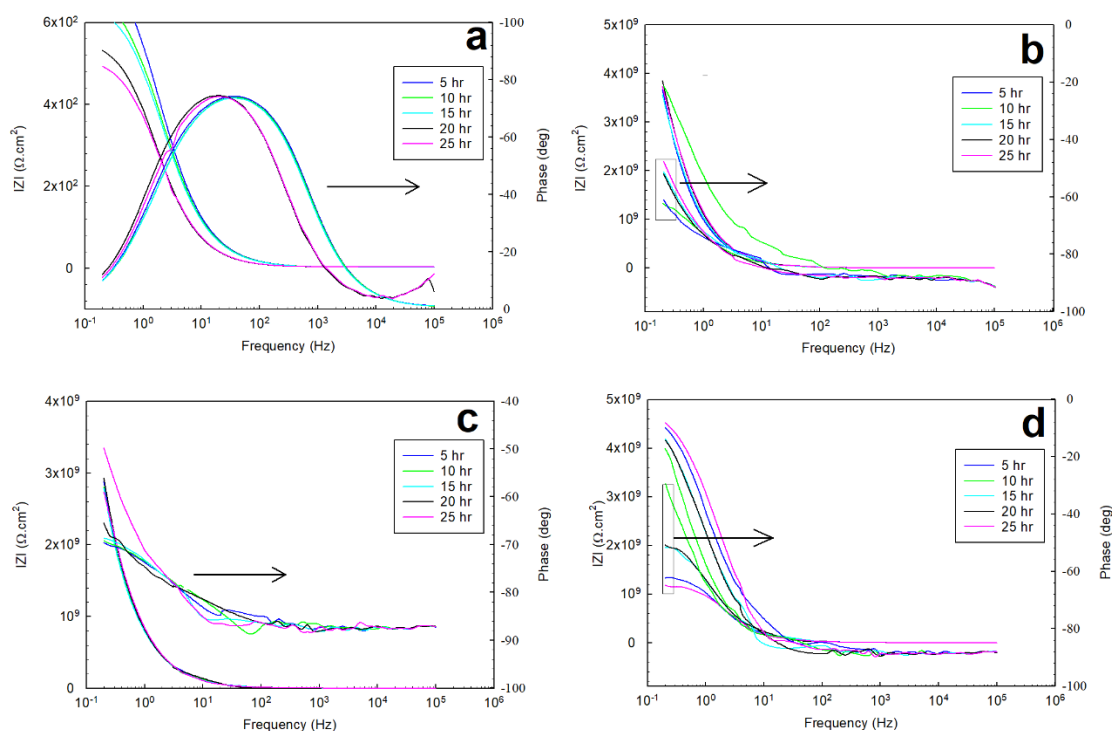
Figure 90. EIS bode plots of 0.5 M HCl solution of a) exposed steel, b) glass/epoxy, c) Kevlar/epoxy, d) epoxy systems.

In H_2SO_4 solutions, the hydrogen generation was more vigorous. Still, for the glass-epoxy system, it incentivized the anodic reactions to form protective films. It happened at rates high enough to surpass the disruption from the hydrogen generation to precipitate, and decelerate the dissolution, and promote the resistance of the layer. The resistance was higher than that of the HCl solutions, and it increased with time from nearly 3 $M\Omega.cm^2$ to 10 $M\Omega.cm^2$. In the Kevlar-epoxy system, however, the resistance was expectedly lower, and it decreased with time. The epoxy deteriorated with Kevlar fibers, not facilitating precipitation of influential passive films on the heavily attacked surface of system resistance of nearly 0.1 $M\Omega.cm^2$. Its bode phase peaks, in Figure 92,

indicated the two-time-constant-based nature of the interactions. The epoxy-only system exhibited reliability better than the Kevlar-epoxy system, and the resistance decreased steadily without fluctuation with time to nearly 6 $M\Omega.cm^2$. The physical properties of the reinforcing elements of glass and Kevlar, if associated with the adherence of the passive films in acidic conditions in future studies, could better predict coating systems' reliability in the long run.

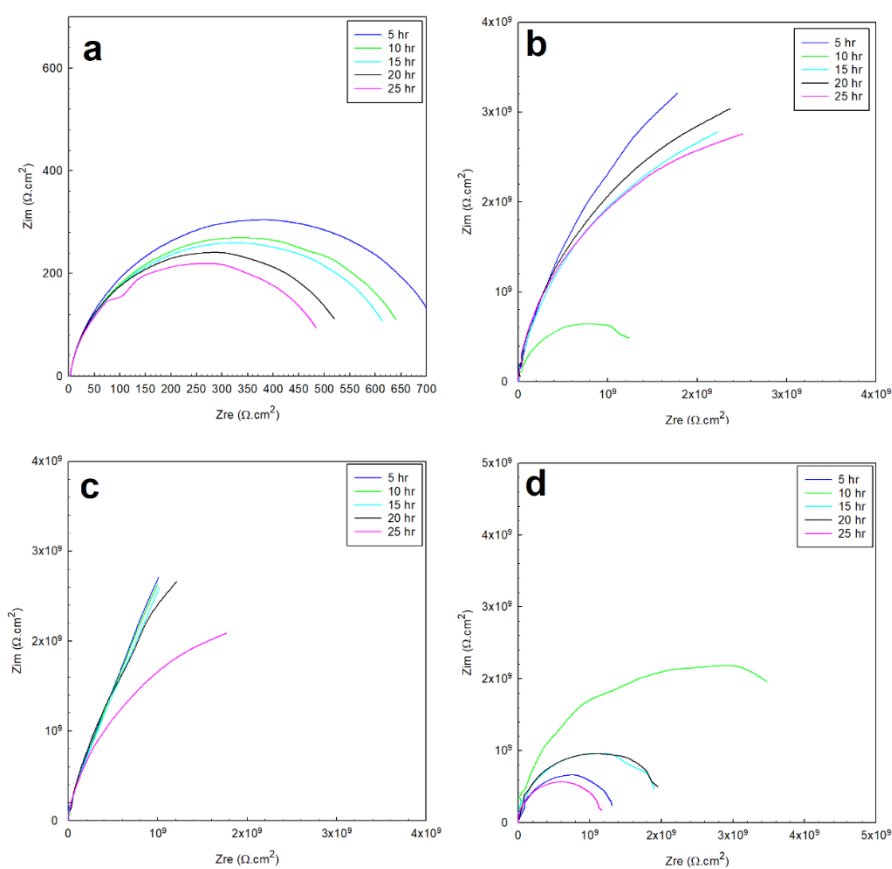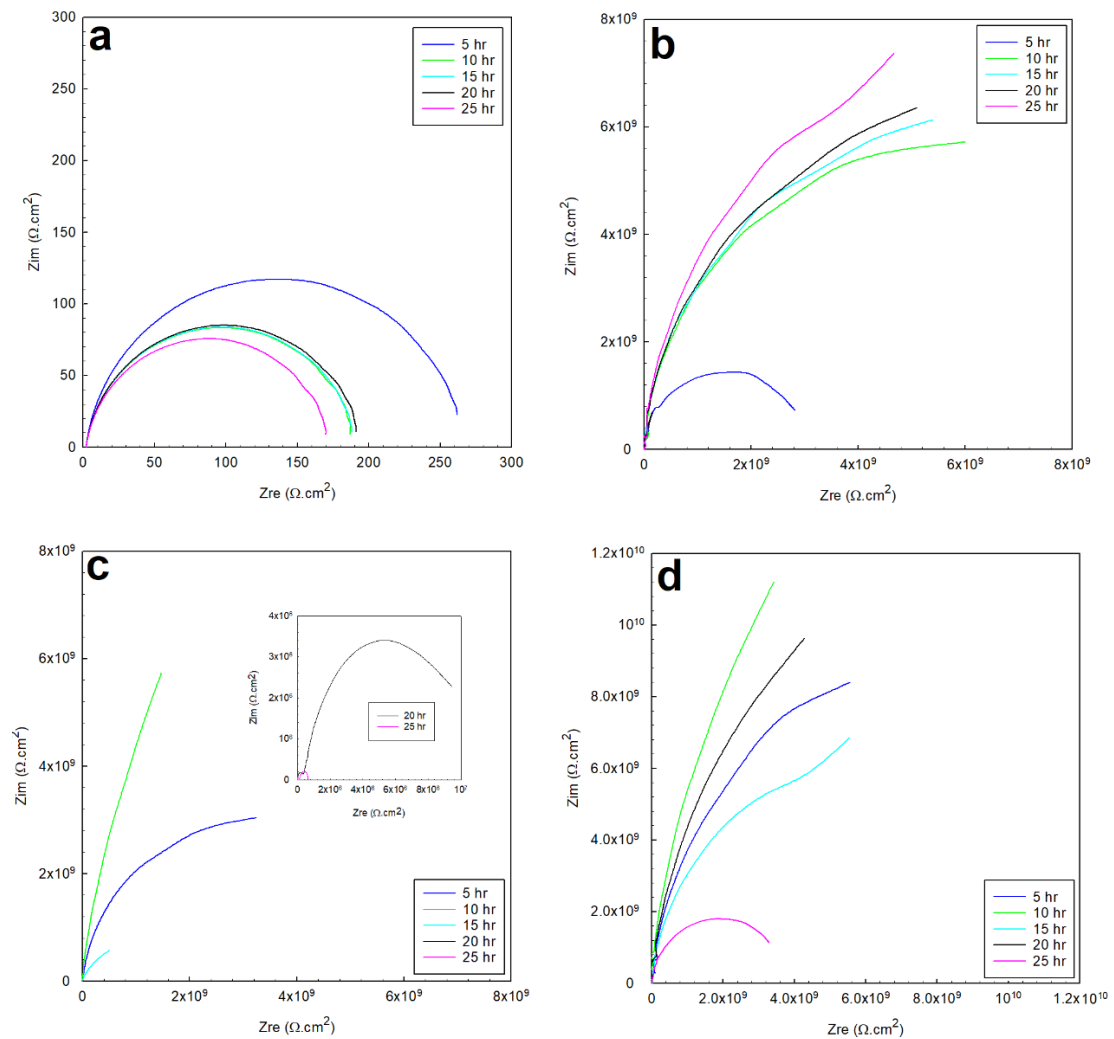Figure 91. EIS Nyquist plots of 0.5 M H_2SO_4 solution of a) exposed steel, b) glass/epoxy, c) Kevlar/epoxy, d) epoxy systems.
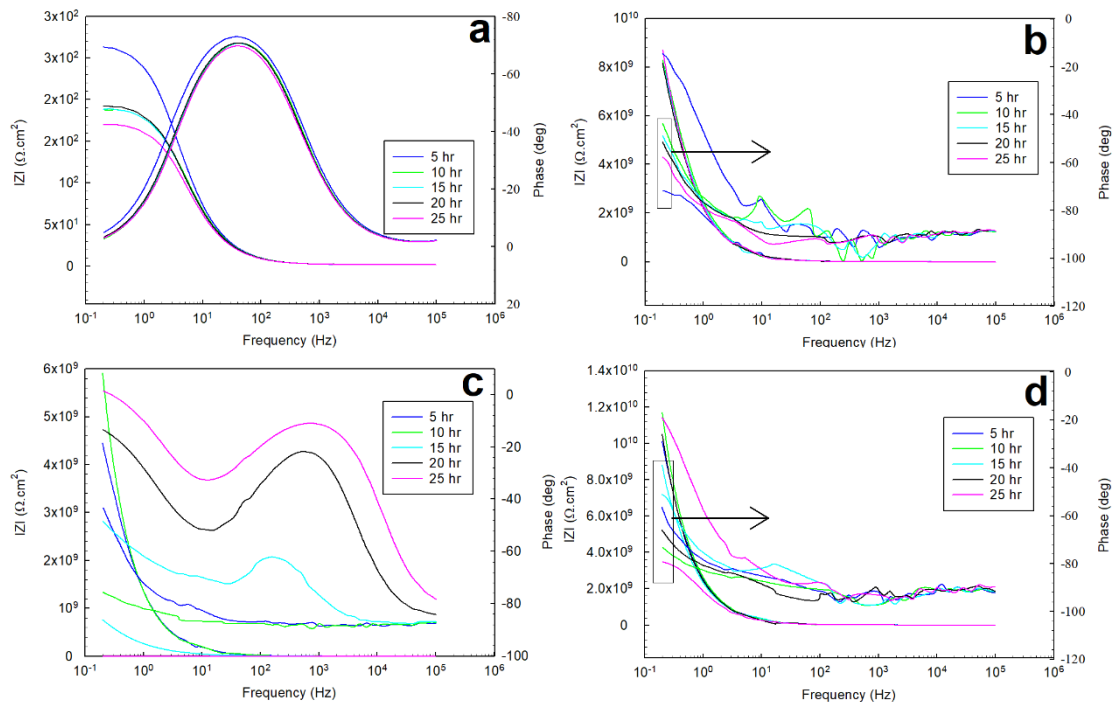
Figure 92. EIS bode plots of 0.5 M H_2SO_4 solution of a) exposed steel, b) glass/epoxy, c) Kevlar/epoxy, d) epoxy systems.

6.3.3 Failure Modes

6.3.3.1 Optical Microscope Images

Figure 93 presents optical microscope images for the tested samples before and after the electrochemical testing, where the failure mode of each specimen is described. The glass-epoxy system showed high stability against corrosion in all solutions without signs of deterioration, pores, or significant localized disbandment or scratches through which sustained corrosion or mass transport occurred. Expectedly, the NaCl solution sample retained salt crystals. Still, with no evidence that chloride ions were involved in localized corrosion or were the result of corrosion reactions – otherwise, iron chloride products would have been intermixed with iron oxides. In the acidic HCl and H2SO4 solutions, slight localized changes in color were observed onto the fibers. Kevlar samples showed deterioration in epoxy and the appearance of pores, and the color

change was most in the H_2SO_4 solution. The epoxy-only system showed evidence of minor pores acted as diffusion channels, but it showed stability regardless of the environmental conditions. Comparably the steel samples were heavily attacked, most severely in the acidic solutions.

GFRP/Steel
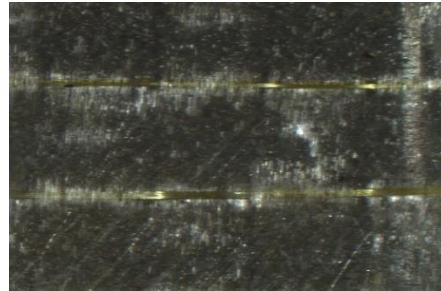
Before
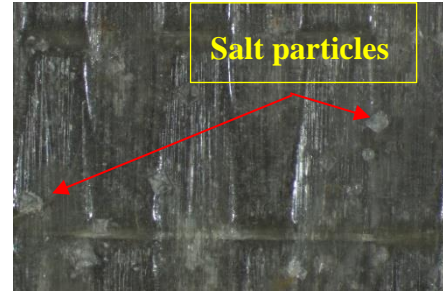
In NaCl solution
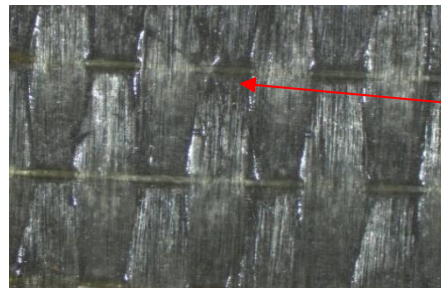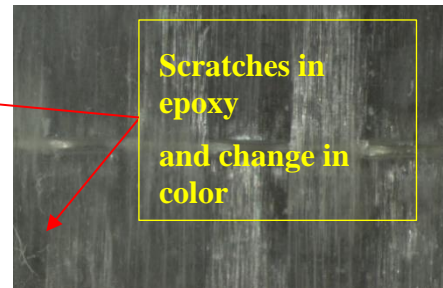
In HCl solution

In H_2SO_4 solution

KFRP/Steel
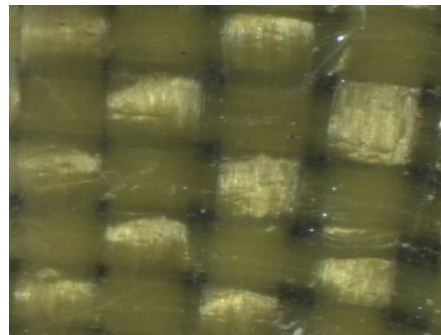
Before
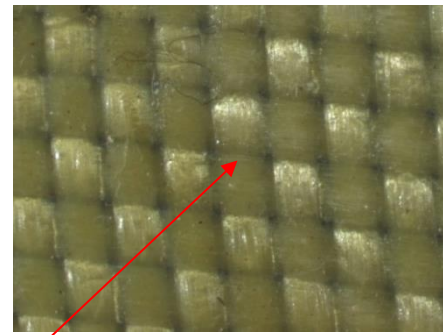
In NaCl solution
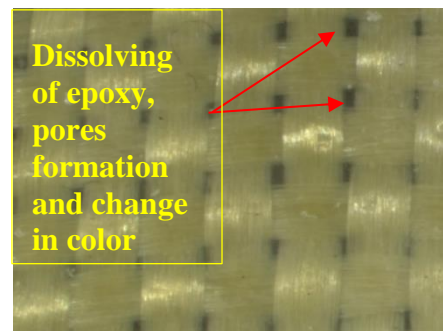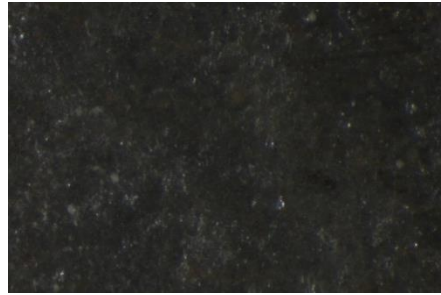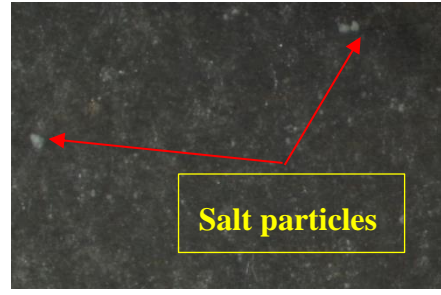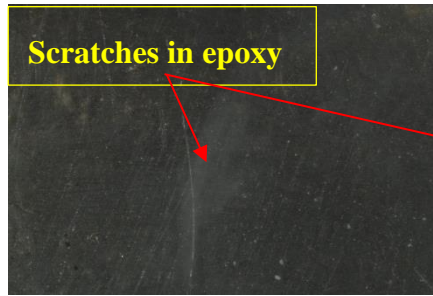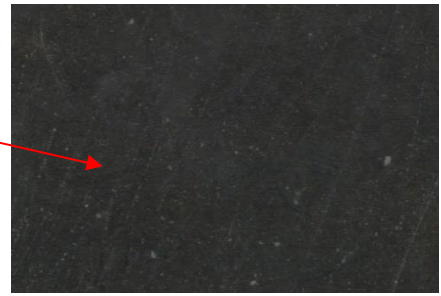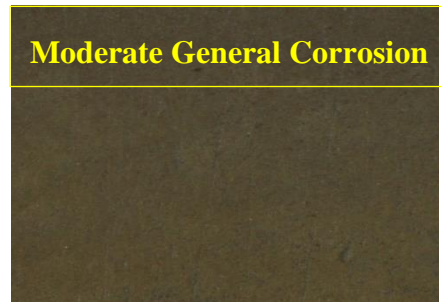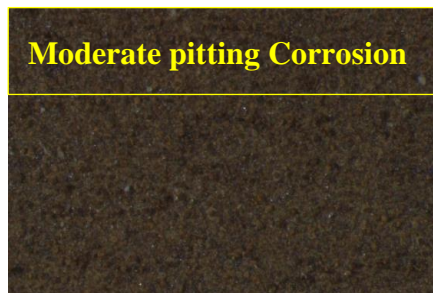
In HCl solution

In H_2SO_4 solution

Figure 93. Optical microscope images for the tested specimens before and after the electrochemical testing.

6.3.3.2 SEM Analysis

The SEM images presented in Figure 94 reveal the nature of the samples before and after testing in top views. It revealed cracks and exposure of embedded fibers from under epoxy subjected to deterioration from acid attack, sustained/assisted by the

137

diffusion of the corrosion species.
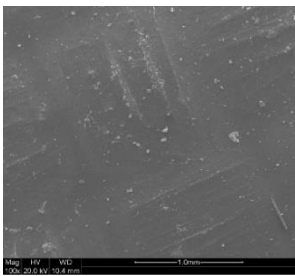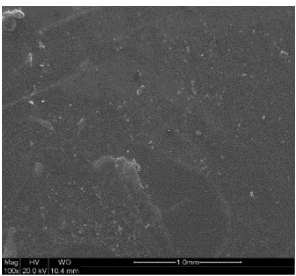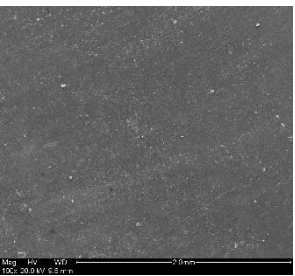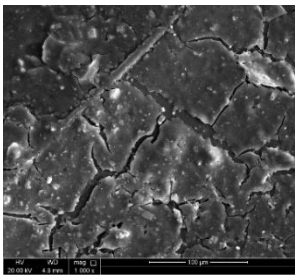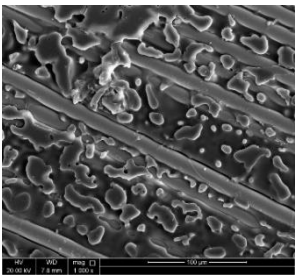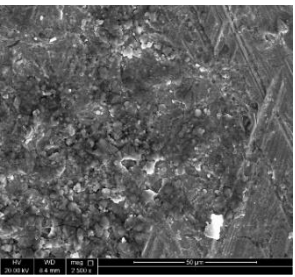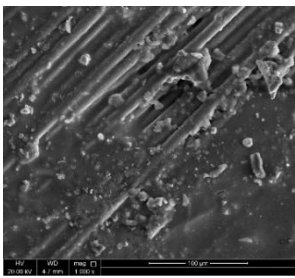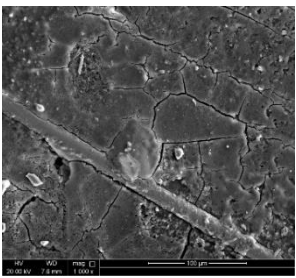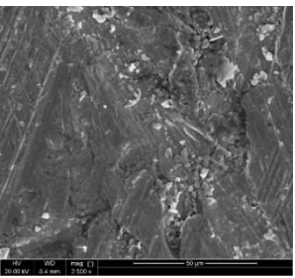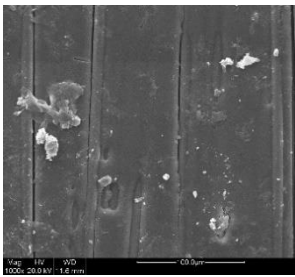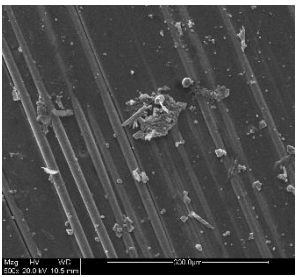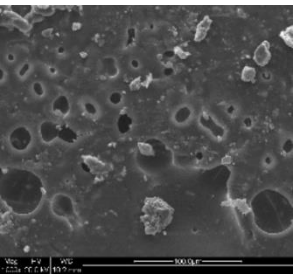
Top view	Kevlar/epoxy-Steel	Glass/epoxy-Steel	Epoxy-steel
Before-Testing			
After-Testing in NaCl solution			
After-Testing in HCl solution			
After-Testing in H_2SO_4 solution			

Figure 94. SEM images for the tested samples, before and after testing.

6.4 Summary

A detailed evaluation of fiber type's effect on the electrochemical corrosion aspects in different highly corrosive solutions was presented. The electrochemical tests offered findings on the feasibility of using an FRP layered system for corrosion protection in

138

mild and severe environmental conditions. The glass/epoxy system exhibited better corrosion/deterioration resistance than the Kevlar/epoxy system in acidic solutions. The corrosion rates when using the FRP system were less than 1 million to 10 million times than exposed substrates.

CHAPTER 7: EXTERNAL CORROSION BEHAVIOR OF STEEL/GFRP

COMPOSITE PIPES IN HARSH CONDITIONS

7.1 Introduction

Corrosion is a harmful attack of metals that results in undesirable effects on the environment during the transport and production of oil and gas [215]. Both corrosion and abrasion cause significant losses and decrease the structural integrity of pipelines [216]. The corrosion development consists of three critical components. The first component is the anode that characterizes the metal under corrosion. The electrolyte is a corrosive medium that transmits the electrons from the anodic site to the cathodic site, an electrical conductor [217]. Oil and gas generally transmit several impurities that are corrosive under many conditions. These impurities might contain carbon dioxide (CO_2) and hydrogen sulfide (H_2S) [3]. Scathing attacks on metal pipes can come from the soil in which the pipe is buried, which will cause corrosion damage for the surfaces of oil and gas pipelines. The degradation of metals is followed regularly by the retrogradation of mechanical properties like strength and ductility. This degradation may lead to the weakening of material and ultimate failure [218]. Corrosion in the metallic pipeline could be classified into two types. These are external and internal corrosions. External corrosion is generally slowed down using organic coating and cathodic protection[219], [220], while corrosion inhibitors are widely used to fight internal corrosion[221] [222].

Inner corrosion is one of the critical factors affecting the integrity of oil and gas pipelines. The non-destructive analysis is frequently applied in different ways as the ultrasound and magnetic current detect and measure internal corrosion damage [223]. In the long run, the existing technology is not helping to eliminate internal corrosion. Composite pipe materials in the oilfields are accepted. FRP composites are used

extensively to protect underground pipes and fuel tanks [7]. Most metallic alloys bear experience corrosion, and the outcomes are costly repairs and safety hazards. Low to moderate pressure composite, plastic flow line, and gathering line systems for oil and natural gas have been in service for many years [119]. Experts in the oil and gas industry agree that future transmission pipelines will have to operate at higher pressures and decrease corrosion costs. To meet the increased demands, maintain safety and reliability, and be competitive, pipeline designers and operators look at alternatives to the conventional metallic pipe and the pure composite pipelines. From the literature reviews, it is understood that most of the published information was focused on the corrosion behavior of coated carbon steel with polymers and corrosion inhibition material [224]–[227]. Recently, many manufacturers provide pipes made of steel with external warps of glass or carbon-based composite layers [119]. The idea behind the external layers of composite materials is to prevent/eliminate external corrosion and add extra strength to the pipe [6]. GFRP/epoxy is the most used material for overwrapping metallic pipes because of their low cost, good mechanical and insulating properties, and deterioration resistance, especially when their interaction is with sweet or salty water. When used in the chemical industry, the GFRP/epoxy may be degraded due to abrasion, change in brittleness, delamination, separation of fiber from the matrix, and the matrix's degradation because of the highly corrosive environments. Some researchers investigated acid solutions' effect on the GFRP/epoxy mechanical properties, durability, and performance.

Both Amaro et al. [228] and Kajorncheappunngam et al. [229] studied the effects of hydrochloric acid (HCl) on glass/epoxy composites, and results revealed that the flexural strength and the flexural modulus decrease with the exposure time. Kotnarowska [230] studied the destruction of epoxy due to the sulfuric acid solution,

and investigation proved the generation of pores in the aged coatings. However, most of the existing studies are based on short-times immersion in corrosive media. Moreover, there is no recent research on the study of corrosion behavior of GFRP/steel under long-term immersion in a highly corrosive environment. Hence, the present chapter was carried out to investigate the comparative evaluation of corrosion behavior of GFRP/steel under different corrosion media. The aim is to develop hybrid pipes and monitor their corrosion properties under harsh corrosive conditions. The GFRP/epoxy layer's influence on the steel pipes' corrosion rate was investigated by carrying out immersion tests in hydrochloric acid 37%, sodium chloride, and sulphuric acid 95% solutions with 0.5M concentration, for six months and one year.

7.2 Materials and Methods

7.2.1 Materials

The base material was ASTM A53 carbon steel alloy. The base material's chemical composition and mechanical properties are presented in Table 19and Table 20, respectively. Carbon steel pipes were overwrapped with a composite material that consists of glass fiber and epoxy resin. E-glass fiber is commonly used because of its low cost [231]. The polymeric matrix is composed of epoxy resin (EL2) and hardener (AT30). The matrix comprises 100 parts mass of the epoxy resin (EL2) and 30 parts mass of curing agent (AT30). Matrix resin with low diffusivity can theoretically protect the fibers from direct contact with the environmental liquid over a long-time span [232].

Table 19. Chemical composition (wt%) of ASTM A53 carbon steel alloy.

Iron	Carbon	Manganese	Phosphorus	Sulfur	Copper	Nickel	Chromium	Molybdenum	Vanadium
96.9	0.3	1.2	0.05	0.045	0.4	0.4	0.4	0.15	0.08

Table 20. Mechanical properties of ASTM A53 carbon steel alloy.

Yield Strength (MPa)	Tensile Strength (MPa)	Elongation in 50mm Min. (%)	Hardness (HRB)
240	415	21	241

7.2.2 Specimen Preparation

The carbon steel pipes had a 6 cm outer diameter, a thickness of 3 mm, and 20 cm for each tested specimen (Figure 95-a). The 5-axis filament-winding machine was used to overwrap the steel pipes with the glass FRP material. The filament winding machine in overwrapping steel pipes is the most used fabrication process [71]. The fiber orientation angle for all the samples was unidirectional at 90° (Figure 95-b). The average thickness of the composite overwrapped system in all the specimens was 2.5 mm ± 0.1, consisting of eight layers. The pipe specimens were closed and sealed using Teflon cups and chemical resistant sealing to prevent leakage to the inner steel layer and ensure that the contact is only between the GFRP composite and the corrosive solution. The cups were designed on SOLIDWORKS and fabricated on the CNC machine.
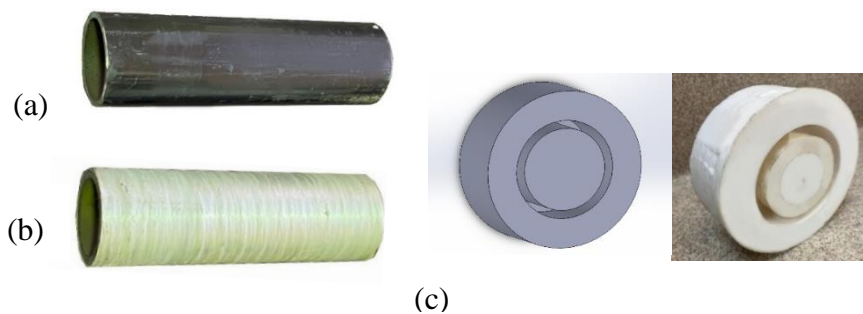
Figure 95. The prepared specimens, (a) steel pipe, (b) GFRP overwrapped steel pipe, (c) Teflon Cups to close the two ends of the pipes.

7.2.3 Immersion Corrosion Test

To evaluate the performance of hybrid composite/metallic pipes and their corrosion properties under harsh corrosive, one can prepare and test GFRP/Steel specimens.

GFRP/Steel pipes' corrosion aspects were evaluated in hydrochloric acid 37%, sodium chloride, and sulphuric acid 95% solutions with 0.5M concentration. The specimens were closed and sealed using Teflon cups and chemical resistant sealing to prevent leakage to the inner steel layer and ensure that the contact is only between the GFRP composite and the corrosive solution. The GFRP/steel pipes were immersed in a glass container containing the corrosive solutions and monitored for six months and one year (Figure 96-a). Simultaneously, the steel pipes without any coating were immersed for two weeks (Figure 96-b).
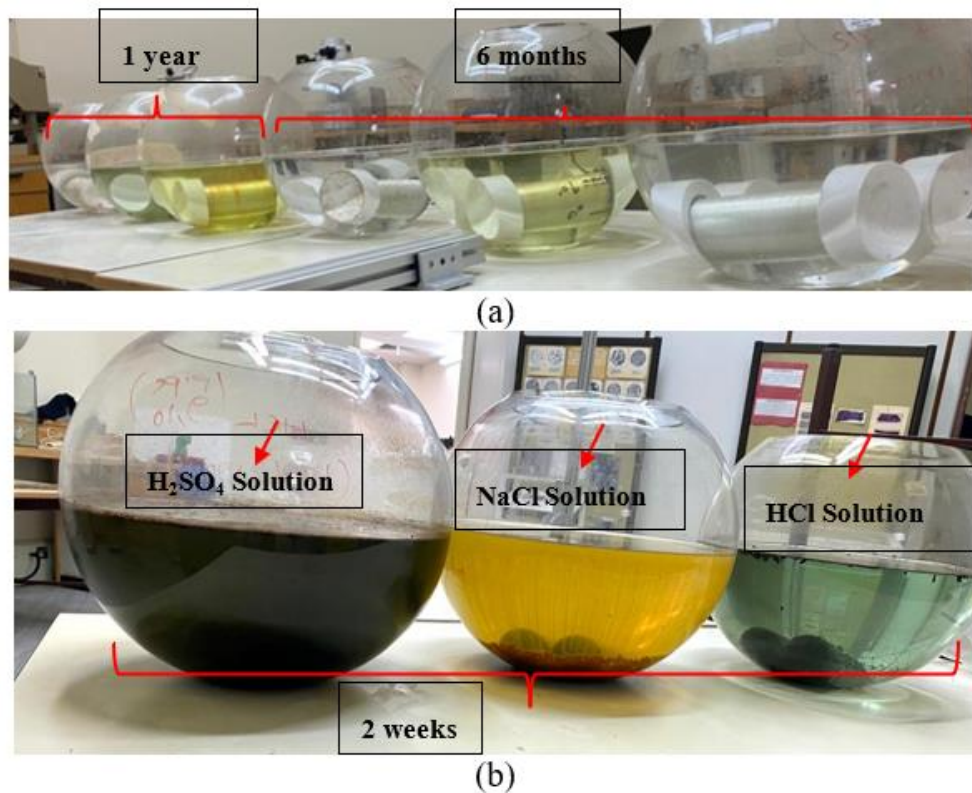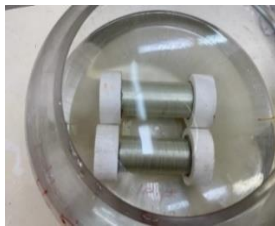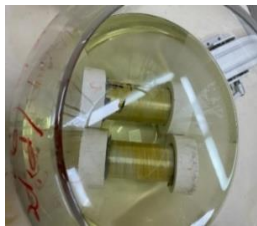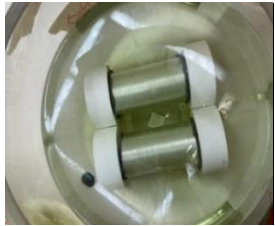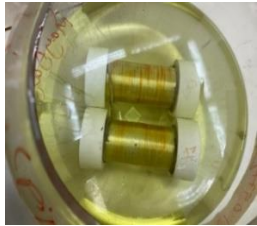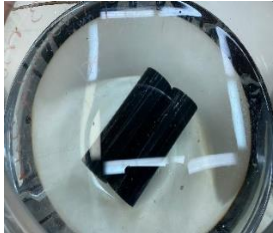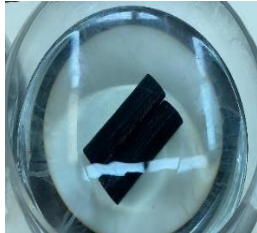
Figure 96. (a) GFRP/steel pipes after one year and six months, (b) steel pipes after two weeks of immersion in acidic environments.

According to ASTM TM0169/G31 [233], duplicate test specimens were exposed in each test, and evaporation losses were controlled by the frequent addition of appropriate solutions to maintain the original volume within ±1%. Table 21 shows the photos for

immersion test containers for all the specimens. Some yellowing signs have been observed at the surface of the GFRP/Steel pipes immersed in the HCl solution. Gamma-ray radiography was used to investigate the FRP layer in this specimen and check any sign of corrosion in the steel layer before peeling off the GFRP layer (Figure 96) (diffusion channel). The radiography images revealed no detected corrosion, metal loss, or thinning in the thickness of the steel layer. However, some degradation for the FRP layer and dissolving of epoxy was observed because of the long-term interaction with the highly concentrated hydrochloric acid solution. According to Krauklis et al. [234], the cause of yellowing in the epoxy layer could be related to the irreversible aging mechanism. When the color of the epoxy surface became yellow, there is oxidation in the epoxy resin chains [235].

Table 21. photos for immersion test containers for all the specimens.

	NaCl solution	H_2SO_4 solution	HCl solution
Steel/GFRP pipes after six months			
Steel/GFRP pipes after one year			
Steel pipes at day 1			

	NaCl solution	H₂SO₄ solution	HCl solution
Steel pipes after two weeks			

No detected corrosion, metal loss or thinning in the thickness of steel layer.

Signs of GFRP/epoxy degradation
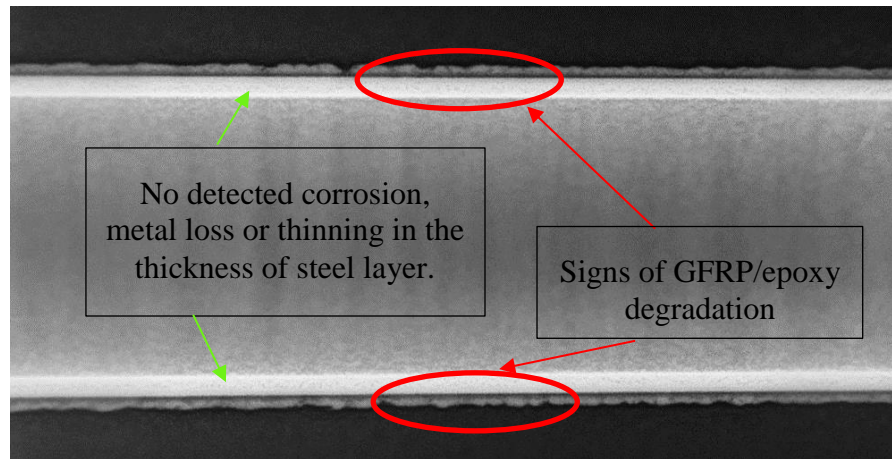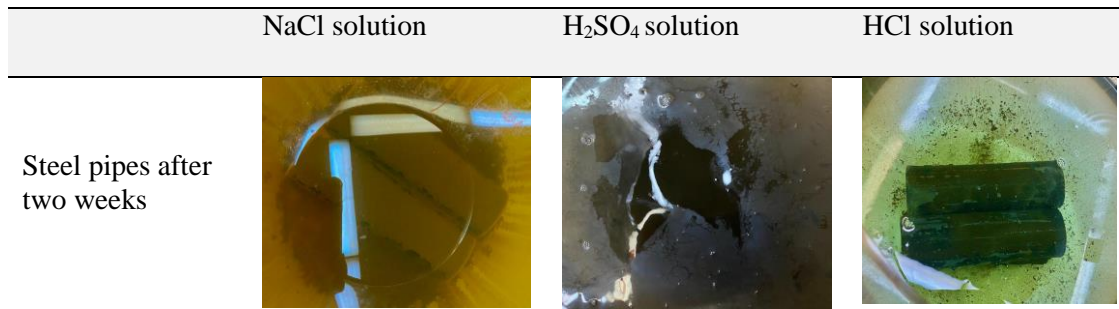
Figure 97. gamma-ray radiography for the GFRP/steel pipe immersed in HCl solution for 1year.

7.3 Results and Discussion

After taking all the immersed pipe out from the solution, the Teflon cups have been removed, and the FRP layer was cut and peeled off from the steel pipes. The corrosion condition was observed and qualitatively analyzed by visual inspection (ll the overwrapped steel pipes.

Table 22), scanning electron microscopy (SEM), X-ray diffraction analysis (XRD), and energy-dispersive X-ray spectroscopy (EDX). Moreover, gamma-ray radiography was used to investigate the FRP layer and corrosion condition of one of the GFRP/steel immersed pipes. Photos for the immersed pipes after the end of the immersing test are presented in Table 22. By the visual inspection, no areas of pitting corrosion were noticed in all the overwrapped steel pipes.

Table 22. photos for the immersed pipes after the end of the immersing test.

	H₂SO₄ solution	NaCl solution	HCl solution
GFRP/steel pipes immersed for six months after removing the GFRP layer			
GFRP/steel pipes immersed for one year after removing the GFRP layer			
Steel pipes immersed for two weeks			

No significant weight loss was observed in the steel pipes that were overwrapped with GFRP/epoxy layer. Simultaneously, the steel pipes immersed without any coating had a massive weight loss in 2 weeks only (Figure 98). The mass loss during the test period can be used as the principal measure of corrosion [236]. Before weighing the corroded pipes, they were cleaned according to the G1-03 ASTM standard [237], which mentions that the ideal cleaning procedure is when cleaning removes only corrosion products and does not result in the removal of any base metal. A soft metallic bristle brush was used in the cleaning of the corrosion products. After corroded test specimens have been cleaned, their masses were measured with an accuracy corresponding to the original mass measurements.

(a)   (b)   (c)   (d)
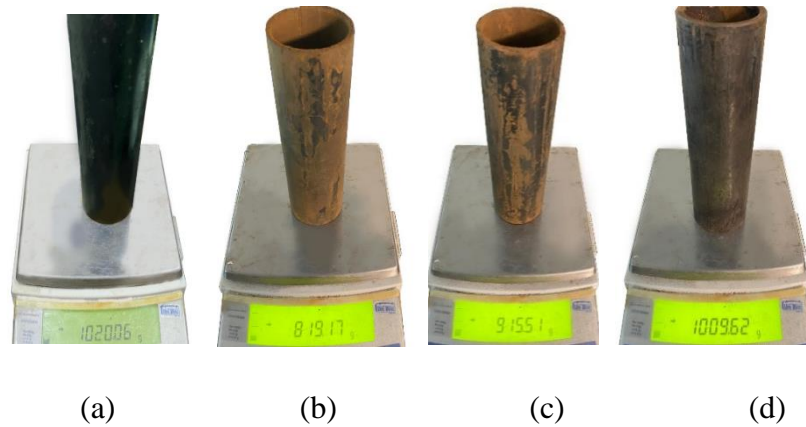
Figure 98. Weight measurements, (a) before, (b) after two weeks in sulfuric acid, (c) after two weeks in hydrochloric acid, (d) after two weeks in sodium chloride.

The steel pipes that were immersed in the corrosive environments witnessed high weight loss in a brief period. The pipes lost 20%, 10%, and 1% of their total weight when immersed in 0.5M sulfuric acid, hydrochloric acid, and sodium chloride solutions, respectively, in 2 weeks. One can calculate the average corrosion rate by the following equation [237].

Corrosion rate = (K × W)/ (A × T × D)   (39)

where:

K = a constant= 8.76×10^4, T = time of exposure in hours, A = area of exposure = outer surface area of the pipe+inner surface area of the pipe+2 × base area (for non-coated steel pipe), and only outer surface area for GFRP/steel pipes. W = mass loss in g. And, D = density in g/cm^3= 7.85 g/cm^3.

Table 23. Corrosion rates for the immersed steel pipes in different solutions.

	Time of exposure (hours)	Area of exposure (cm^2)	Mass loss (g)	Corrosion rate (mm/y)
Non-coated steel in 0.5M H_2SO_4 solution (2 weeks)	336	742.5	201	8.99
Non-coated steel in 0.5M HCl solution (2 weeks)	336	742.5	105	4.69
Non-coated steel in 0.5M NaCl solution (2 weeks)	336	742.5	11	0.49
GFRP/steel in 0.5M H_2SO_4 solution (6 months)	4320	377	5	0.034
GFRP/steel in 0.5M HCl solution (6 months)	4320	377	3	0.020
GFRP/steel in 0.5M NaCl solution (6 months)	4320	377	0	0
GFRP/steel in 0.5M H_2SO_4 solution (1 year)	8640	377	7	0.0239
GFRP/steel in 0.5M HCl solution (1 year)	8640	377	5	0.017
GFRP/steel in 0.5M NaCl solution (1 year)	8640	377	0	0

According to the qualitative categorization of carbon steel corrosion rates for oil production systems, any corrosion rate above 0.38 mm/y is considered severe pitting corrosion, a catastrophic localized steel failure that produces global severe economic losses [238]. Moreover, any corrosion rate below 0.025 mm/y is considered low general corrosion [30]. General corrosion or rusting is considered a uniform corrosion process in which micro corrosion cells are activated at the corroded area. For the GFRP/steel pipes, no weight loss was detected in the case of NaCl immersion, which means that the GFRP/epoxy layer eliminated any possible Corrosion in the base metal. Also, for

HCl and H2SO4, the corrosion rate is considered very low compared to the corrosion rate of the non-coated steel (less than 1/100 of the conventional steel pipes corrosion rate).

7.3.1 SEM and EDX

Table 24 presents the surface analysis (SEM/EDX) that shows the participation of the different alloying elements in each tested specimen according to the alloy constituents for the immersed steel pipes, before and after immersion in the different solutions at a magnification of 5000x. The first row shows the SEM images for the steel after polishing, where the steel surface is very flat, and the traces are shown results from sanding by sandpaper. The second and third-row presents the SEM images for the pipes that were overwrapped by GFRP and immersed in different solutions for six months and one year, respectively. It could be observed that the surface of the steel that was immersed in sodium chloride solutions is smooth and clean, and there is no evidence of any corrosion reaction, which proves the functionality of the GFRP/epoxy layer. While for HCl and H2SO4 immersion cases, it could be noticed that the surface is rough due to the removal effect of the FRP/epoxy layer and the presence of some remnant epoxy particles. The fourth row shows the cases of non-coated immersed steel pipes. The universal corrosion products, some of which develop and blossom to be corrosion flowers, covered the exposed specimens totally, as shown in the SEM images of the immersed steel in HCl and H_2SO_4.

Moreover, the porous lamellar structure is detected in all the immersed specimens without coating, which results from the Pitting corrosion feature, especially when immersed in HCl solution. The critical factor leading to stress cracking corrosion and pitting corrosion of pipeline steel is chloride ion reactions. The adsorbed chloride ions

on the metal surface will break down the steel's passivity and consequently upturn the corrosion rate [239]. Figure 98 presents a schematic diagram that demonstrates the pitting corrosion mechanism of pipeline steel in the corrosive environment containing chloride ions, where the negative ions of chloride attract the hydrogen protons to the pitting areas, causing hydrogen protons to accumulate, driving a more significant cathodic reaction outside the pitting, and accelerating anodic reaction inside the pitting.
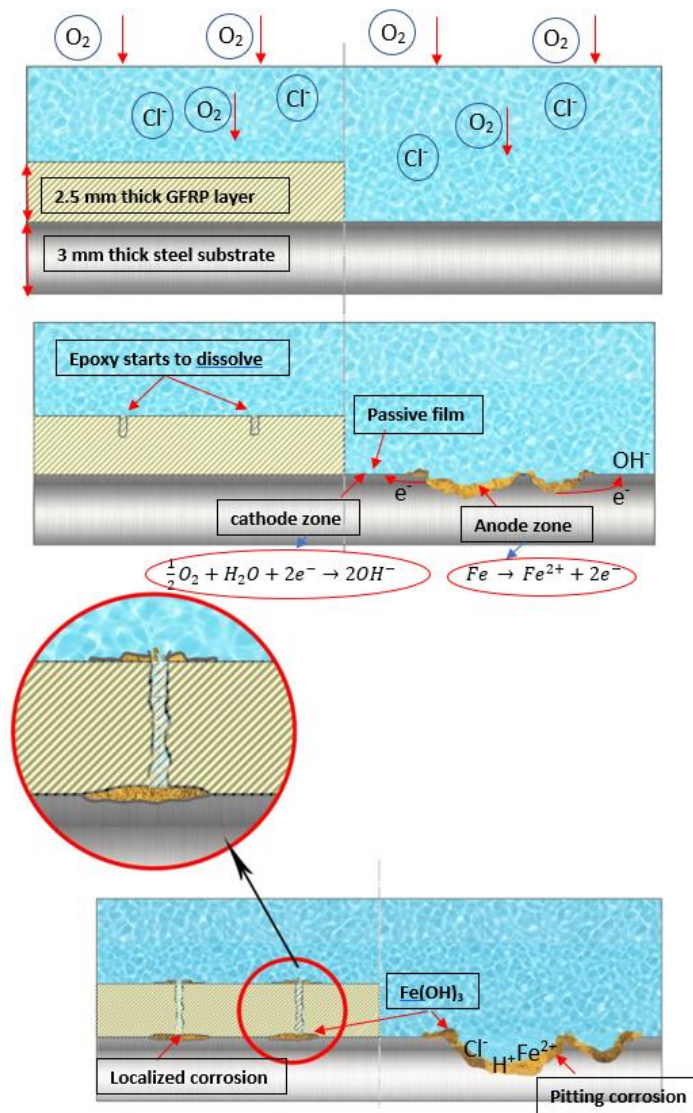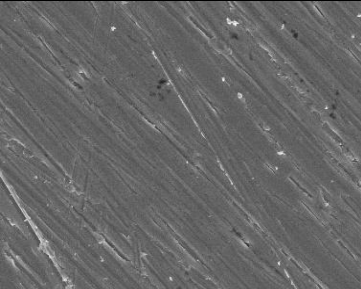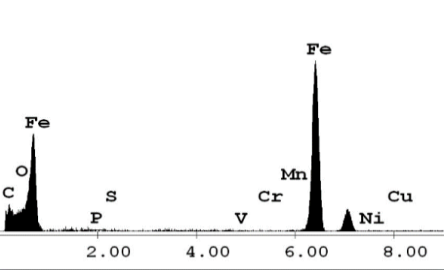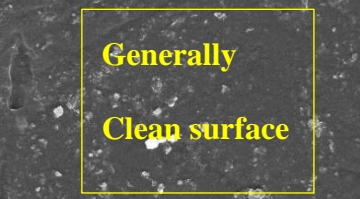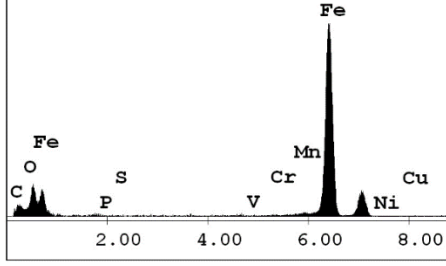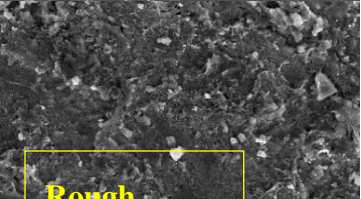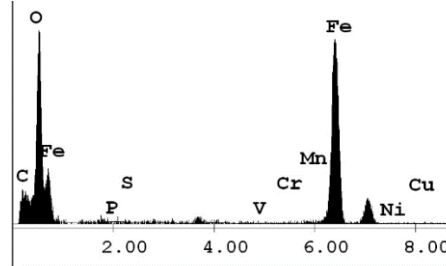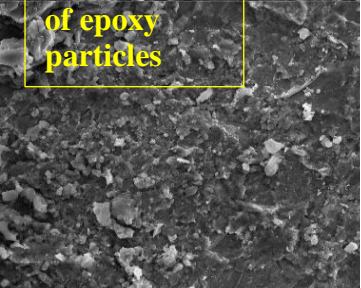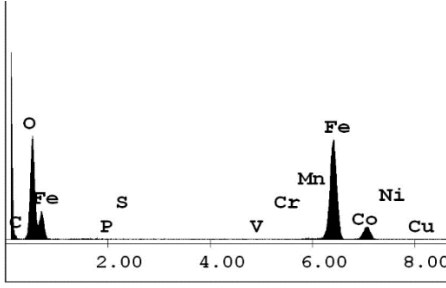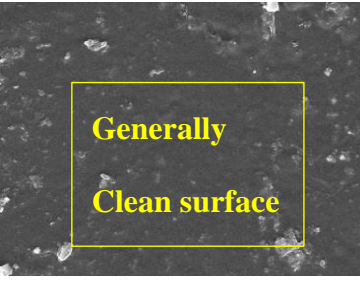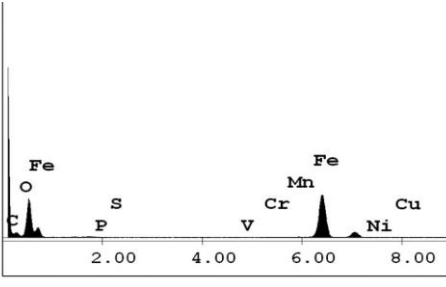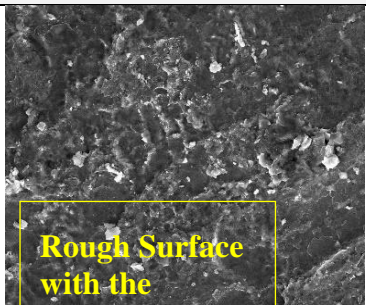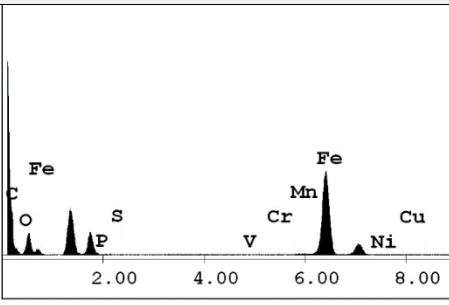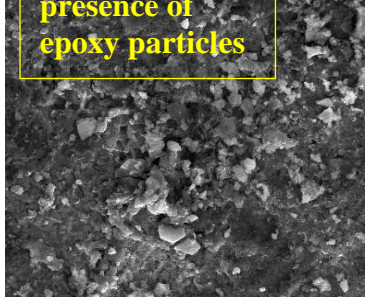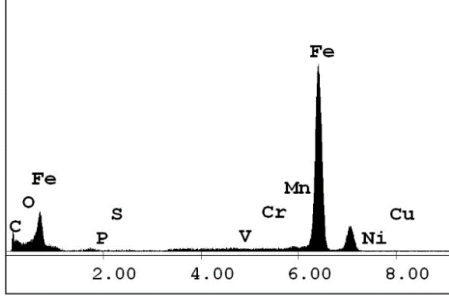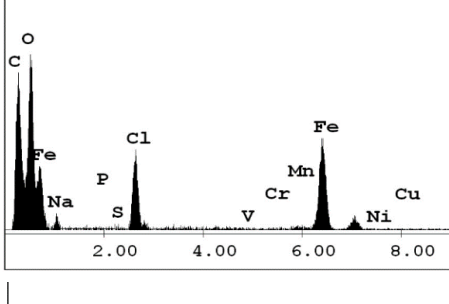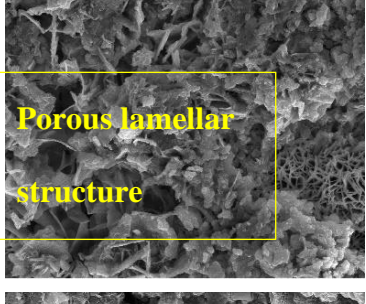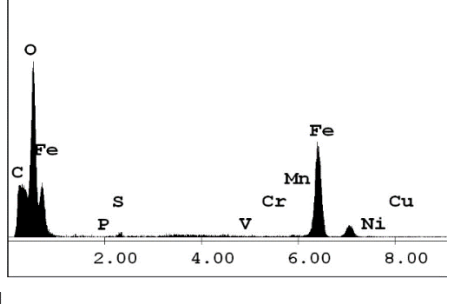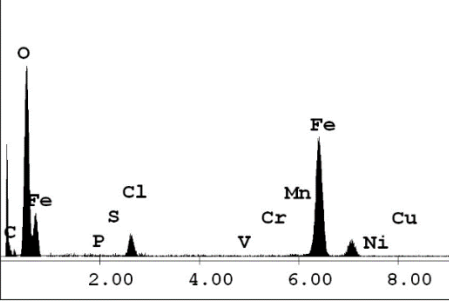
Figure 99. Schematic for the development of corrosion on uncoated steel vs. GFRP/steel in corrosive solution.

Table 24. SEM images and EDX analysis for the immersed specimens before and after immersion (5000x magnification).

	SEM	EDX
New steel pipe (before immersion)		
GFRP/steel pipes immersed for six months in NaCl solution after removing the GFRP layer	Generally Clean surface	
GFRP/steel pipes immersed for six months in H_2SO_4 solution after removing the GFRP layer	Rough Surface with the presence of epoxy particles	
GFRP/steel pipes immersed for six months in HCl solution after removing the GFRP layer		
GFRP/steel pipes immersed for one year in NaCl solution after removing the GFRP layer	Generally Clean surface	

SEM	EDX
GFRP/steel pipes immersed for one year in H₂SO₄ solution after removing the GFRP layer	
GFRP/steel pipes immersed for one year in HCl solution after removing the GFRP layer	
Steel pipes immersed for two weeks in NaCl solution	
Steel pipes immersed for two weeks in H₂SO₄ solution	
Steel pipes immersed for two weeks in HCl solution	

The SEM images show: Rough Surface with the presence of epoxy particles, Corrosion pits, Porous lamellar structure, and Corrosion flowers.

153

7.3.2 X-Ray Diffraction Analysis (XRD)

Standard methods for identifications and characterizations of iron oxides have tradi-tionally used X-ray diffraction (XRD). X-ray diffraction analysis was applied on all immersed specimens to detect and characterize any corrosion products' formation on the surface. Figure 100-10 show the XRD patterns representing the signal intensity against 2θ collected from the carbon steel surfaces at the end of each immersion experiment for the three corrosive solutions. Figure 100 patterns reveal that the only crystalline phase detected on the polished steel surface was Iron (Fe). Some low peaks of iron oxide phase as Magnetite compound (Fe_3O_4) for the painted steel specimen and no other phases were detected. The most intense peak for both patterns was observed at $2\theta = 44.79°$, and the presence of iron oxide compounds results from the typical oxidation in nature, where the painted pipes were tested as received from the industry without any polishing.
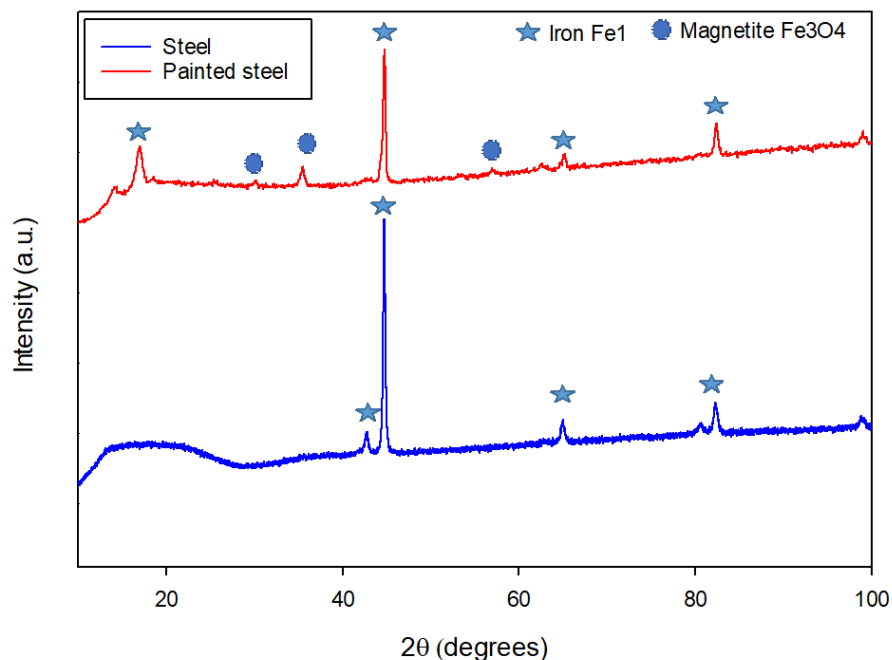
Figure 100. XRD pattern for the steel surface before immersion.

Figure 101-10 patterns for the steel pipes were overwrapped with GFRP layer and

immersed in sulfuric acid, hydrochloric acid, and sodium chloride solutions for six months and one year. The patterns reveal that the crystalline phases detected are mainly iron Fe1, where the most intense peak in almost the specimens observed at $2\theta = 44.79°$ same as the new steel specimen. It is also observed that iron oxide compounds were detected in small peaks as magnetite and hematite in all the patterns. Some researchers studied the transformation of the iron oxides. They found that it begins with nucleation and growth of goethite (FeOOH) followed by dehydration to hematite (Fe_2O_3), and then reduction to magnetite (Fe_3O_4) [240]. Simultaneously, the XRD analysis for the uncoated steel that was immersed for two weeks in sulfuric acid solutions exposes that the corrosion products consist mainly of cohenite, goethite, and hohmannite, where all of them are compounds that are usually found in iron corrosion scales. Goethite (FeOOH) is an iron oxyhydroxide, and it is the main component of rust [241]; those compounds are predominately present in iron corrosion scales of corroded iron pipe in water distribution systems [242].
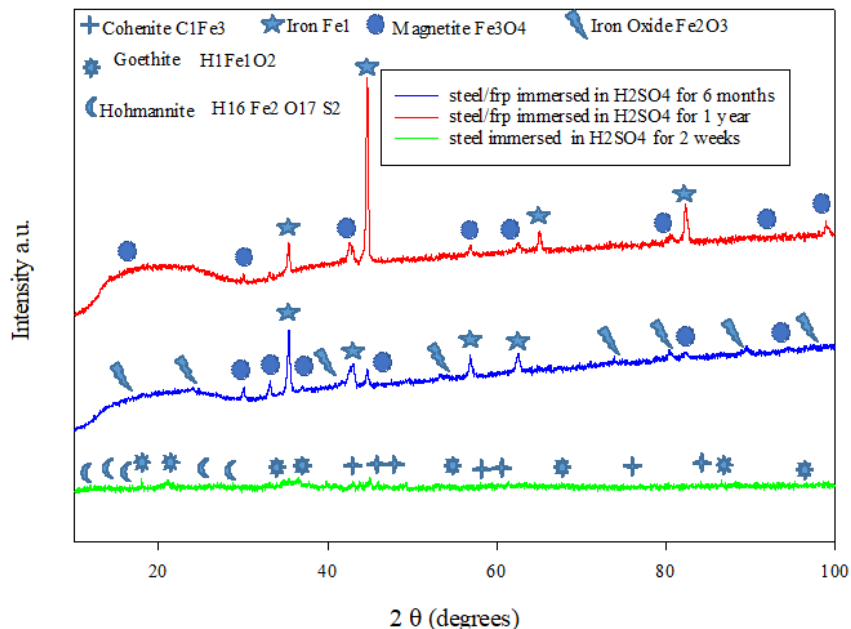
Figure 101. XRD patterns for the steel surfaces after immersion in H_2SO_4 solution.

Figure 102 reveals that the corrosion products for the uncoated steel that was immersed for two weeks in HCl solution consist of magnetite and goethite. Corrosion of iron in an anoxygenic atmosphere usually proceeds via goethite (FeOOH) through hematite and magnetite [243]. Magnetite is a familiar kind of iron oxide that forms at room temperature in crevices at steel alloy, where the oxidation product of Fe_3O_4 is either γ-Fe_2O_3 or α-Fe_2O_3 depending on the oxidation temperature [244]. While Figure 103 reveals that the crystalline phases detected for the uncoated steel that was immersed for two weeks in NaCl solution are mainly iron Fe1 with the presence of compounds that consists of halite (Cl1Na1), sodium peroxide (Na1O2), and tetrachloromethane (C1Cl4). Halite is a form of isometric crystals known as rock salt [245] accumulated on the surface of the steel pipe when immersed in sodium chloride solution. Simultaneously, sodium peroxide is produced as the reaction of sodium with oxygen that crystallizes with hexagonal symmetry [246].
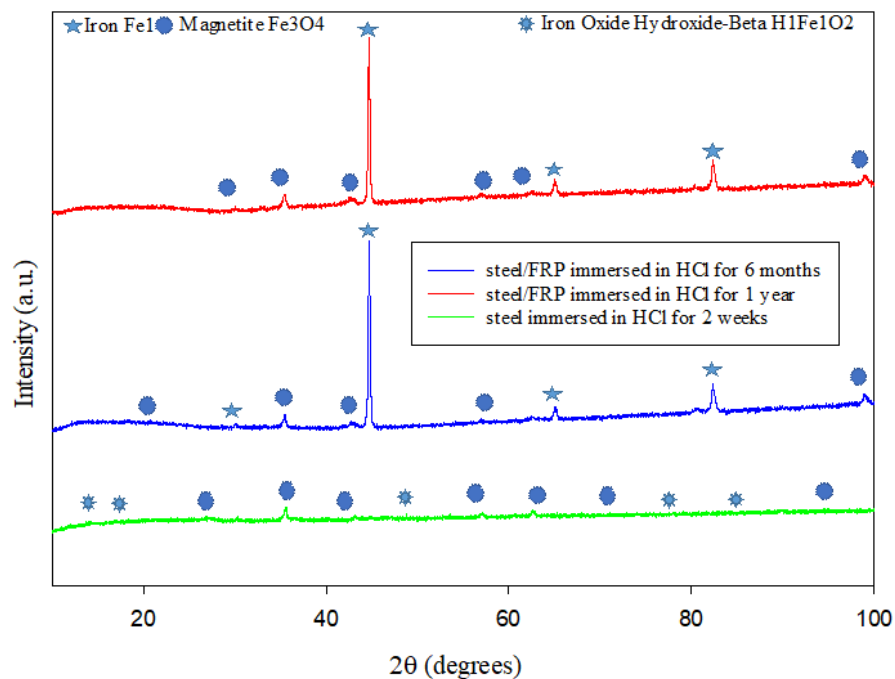
Figure 102. XRD patterns for the steel surfaces after immersion in HCl solution.
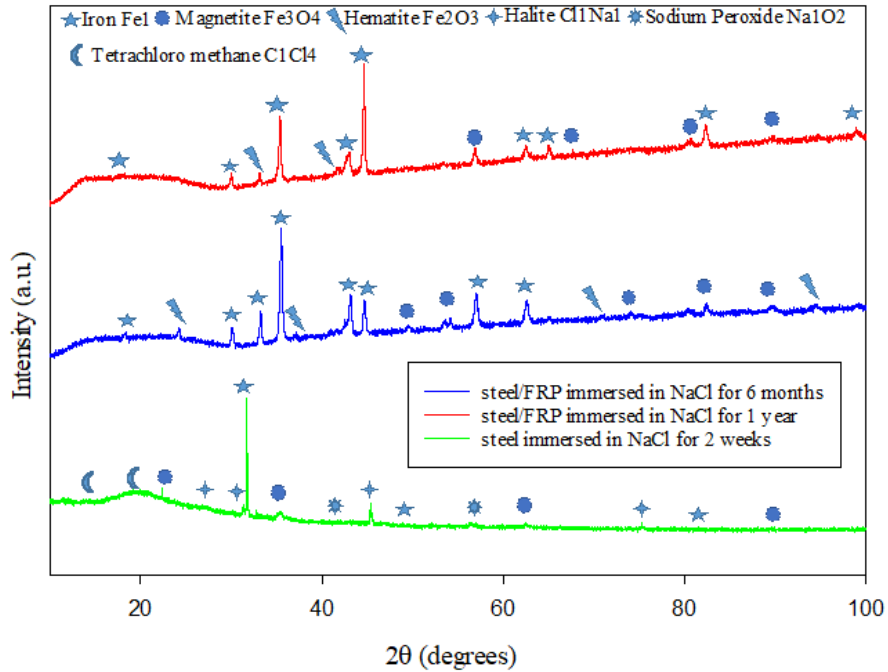
Figure 103. XRD patterns for the steel surfaces after immersion in NaCl solution.

7.4 Summary

In this study, the long-term effect of GFRP/epoxy when exposed to different highly corrosive environments in protecting the steel pipe from any potential corrosion was studied. The GFRP/steel pipes were immersed in a glass container containing the corrosive solutions and monitored for six months and one year, while the steel pipes as received from the industry were immersed for two weeks. SEM, XRD, and EDX qualitatively analyzed the specimens. Results show that the GFRP/steel pipes have excellent corrosion resistance compared to the carbon steel pipes without coating.

CHAPTER 8: CONCLUSION AND FUTURE WORK

The present study investigated the fiber type and fiber orientation's effects on the interface bonding between steel and fiber-reinforced composites. The fracture loads for modes I and II were computed using DCB and ENF tests. The outcomes revealed that the interface bonding between the steel and fiber-reinforced composite and the modes I and II fracture toughness had been significantly affected by fiber orientation and fiber types. For both modes I and II tests, the CFRP/steel interface exhibited the highest toughness when comparing the different tested fabric types. However, when comparing the effect of fiber orientations, the 0° GFRP/Steel interface had the maximum toughnesses for mode I and mode II tests. It was well observed that all specimens' delamination response strongly depends on the loading condition. The shearing-mode (mode II) fracture toughness is larger than the opening-mode (mode I) fracture toughness in all the tested specimens, proving that the interface between FRP and steel layer is stronger in mode II than in mode I due to the compaction process during the bending loading. While in mode I, the loading process is opening. All steel-composite specimens tested for mode I have established some cracking and peeling off for the resin matrix layer in some sheet areas, followed by some fiber failure and breakage. While all steel-composite specimens tested for mode II have experienced matrix cracks and fiber-matrix debonding, followed by fiber failure and breakage due to the applied bending loads.

Later a cost-effective FRP composite overwrap system was introduced to give more strength for the welded regions and eliminate the effect of weld metal and heat-affected zone. By applying the three-point and four-point bending loading method on the prepared pipe specimens, it was observed that when comparing it with the conventional

steel pipe, the maximum flexure load increased by 16.94 kN in the case of three-point bending with two welding lines along with the pipe specimen. On the other hand, the increase in the load-carrying capacity was 10.35 kN and 26.8 kN in three-point bending with four welding lines along with the pipe specimen and four-point bending. All failure modes of the deformed specimens were observed and analyzed using scanning electron microscopy. Where steel-composite samples have established matrix cracking and fiber-matrix debonding followed by fiber failure and breakage because of the applied bending loads.

Moreover, the plastically deformed steel specimens, which have been taken from HAZ, revealed that they experienced three stages with the increase of the applied bending load: the elastic stage, ovalization stage, and failure stage after exceeding the ultimate strength of the specimen. In addition, it was concluded that the fracture strength of welded structures is significantly affected by HAZ microstructure, and increasing stress concentration due to welding defects will sharply reduce fracture strength since martensite structure with fine lath. High dislocation density was observed in the HAZ after welding.

Then the internal pressure capacity of steel, GFRP/steel, and GFRP/steel/GFRP composite pipes was tested using the Resato high-pressure machine model SPU-CC-2000 ASTM D1599 standard. The external GFRP composite layers were wound at an angle of ± 55° and 90° using a computerized 5-axes filament winding machine. The novelty was the internal reinforcement fabrication. An elastic mandrel was used for this purpose. In addition to the fact that the produced pipes are corrosion-free, the testing results showed significant improvement in the internal pressure capacity compared to the conventional steel pipes.

Moreover, a detailed evaluation of fiber type's effect on the electrochemical corrosion aspects in different highly corrosive solutions was presented. The electrochemical tests offered findings on the feasibility of using an FRP layered system for corrosion protection in mild and severe environmental conditions. The glass/epoxy system exhibited better corrosion/deterioration resistance than the Kevlar/epoxy system in acidic solutions. The corrosion rates when using the FRP system were less than 1 million to 10 million times than exposed substrates.

Finally, the long-term effect of GFRP/epoxy when exposed to different highly corrosive environments in protecting the steel pipe from any potential corrosion was studied. The GFRP/steel pipes were immersed in a glass container containing the corrosive solutions and monitored for six months and one year, while the steel pipes as received from the industry were immersed for two weeks. SEM, XRD, and EDX qualitatively analyzed the specimens. Results showed that the GFRP/steel pipes have excellent corrosion resistance compared to the carbon steel pipes without coating. However, hydrochloric and sulfuric acid solutions can attack the GFRP/epoxy layer surface by increasing the water's saturation uptake in the material. Hence, the rate of absorption and saturation moisture content increases with the increase of soaking time and will eventually lead to the formation of pores in the GFRP/epoxy layer. The results were promising. They indicate that when fabricated perfectly with the appropriate resin system, the FRP layer will offer excellent corrosion resistance for decades and improve the durability of the pipelines with severe corrosive environments.

In the light of the development so far, the following points are suggested for further enhancing the performance of the hybrid pipe:

1- Deeply investigate different polymeric matrices' behavior in different acidic

solutions and concentrations to clearly understand each matrix type's dissolving rate, since the dissolving of the polymeric matrix could lead to a significant degradation in the pipeline over time.

2- Further studies on the joining of FRP pipes, interfacial properties between the FRP layers and the conventional pipe, load transfer mechanism between the FRP composite systems layers should be conducted to increase the confidence in expanding the market using this encouraging material system.

3- Subjecting the GFRP/steel pipe to an initial overpressure cycle to cause yielding in the steel pipe. So that when the pressure is released, it results in a state of residual compression in the steel pipe that will give an advantage in increasing the safety factor for any subsequent yielding during the regular pressure cycles, and residual tension in the overwrapped GFRP layer that will ensure that no slip of the fibers takes place, by enhancing the interfacial properties between the steel and FRP layer.

REFERENCES

[1]   F. Taheri, "Advanced fiber-reinforced polymer (FRP) composites for the manufacture and rehabilitation of pipes and tanks in the oil and gas industry," in *Advanced Fibre-Reinforced Polymer (FRP) Composites for Structural Applications*, 2013, pp. 662–704.

[2]   K. A. Beklemysheva, A. V. Vasyukov, V. I. Golubev, and Y. I. Zhuravlev, "On the Estimation of Seismic Resistance of Modern Composite Oil Pipeline Elements," *Dokl. Math.*, vol. 97, no. 2, pp. 184–187, 2018, doi: 10.1134/S1064562418020011.

[3]   L. T. Popoola, A. S. Grema, G. K. Latinwo, B. Gutti, and A. S. Balogun, "Corrosion problems during oil and gas production and its mitigation," *International Journal of Industrial Chemistry*, vol. 4, no. 1. 2013, doi: 10.1186/2228-5547-4-35.

[4]   Laney Patrick, "Use of Composite Pipe Materials in the Transportation of Natural Gas," *Ineel/Ext-02-00992*, vol. 64, no. 2, pp. 294–296, 1990.

[5]   K. S. Lim, S. N. A. Azraai, N. M. Noor, and N. Yahaya, "An Overview of Corroded Pipe Repair Techniques Using Composite Materials," *World Acad. Sci. Eng. Technol. Int. J. Chem. Mol. Nucl. Mater. Metall. Eng.*, vol. 10, no. 1, pp. 19–25, 2016.

[6]   F. G. Al-Abtah, E. Mahdi, and S. Gowid, "The use of composite to eliminate the effect of welding on the bending behavior of metallic pipes," *Compos. Struct.*, vol. 235, 2020, doi: 10.1016/j.compstruct.2019.111793.

[7]   L. C. Hollaway, "Using fiber-reinforced polymer (FRP) composites to

rehabilitate differing types of metallic infrastructure," in *Rehabilitation of Metallic Civil Infrastructure Using Fiber Reinforced Polymer (FRP) Composites: Types Properties and Testing Methods*, 2014, pp. 323–372.

[8]   C. R. Alexander, "Advances in the Repair of Pipelines Using Composite Materials," *Pipeline Gas Technol. Mag. Hart Energy Publ. LP*, no. July, pp. 1–11, 2009.

[9]   M. M. Watanabe Junior, J. M. L. Reis, and H. S. da Costa Mattos, "Polymer-based composite repair system for severely corroded circumferential welds in steel pipes," *Eng. Fail. Anal.*, vol. 81, pp. 135–144, 2017, doi: 10.1016/j.engfailanal.2017.08.001.

[10]   N. R. F. Rohem, L. J. Pacheco, S. Budhe, M. D. Banea, E. M. Sampaio, and S. de Barros, "Development and qualification of a new polymeric matrix laminated composite for the pipe repair," *Compos. Struct.*, vol. 152, pp. 737–745, 2016, doi: 10.1016/j.compstruct.2016.05.091.

[11]   Ł. Mazurkiewicz, J. Małachowski, K. Damaziak, and M. Tomaszewski, "Evaluation of the response of fiber-reinforced composite repair of steel pipeline subjected to puncture from excavator's tooth," *Compos. Struct.*, vol. 202, pp. 1126–1135, 2018, doi: 10.1016/j.compstruct.2018.05.065.

[12]   K. S. Lim, S. N. A. Azraai, N. Yahaya, N. Md Noor, L. Zardasti, and J. H. J. Kim, "Behaviour of steel pipelines with composite repairs analyzed using experimental and numerical approaches," *Thin-Walled Struct.*, vol. 139, pp. 321–333, 2019, doi: 10.1016/j.tws.2019.03.023.

[13]   J. R. Reeder, "An Evaluation of Mixed-Mode Delamination Failure Criteria,"

NASA Tech. Memo. 104210, 1992.

[14] Y. Zhang, L. Sun, L. Li, B. Huang, T. Wang, and Y. Wang, "Direct injection molding and mechanical properties of high strength steel/composite hybrids," *Compos. Struct.*, 2019, doi: 10.1016/j.compstruct.2018.11.035.

[15] P. B. Potyrała, "Use of Fibre Reinforced Polymer Composites in Bridge Construction. State of the Art in Hybrid and All-Composite Structures," *Thesis*, 2011.

[16] H. Altenbach, J. Altenbach, W. Kissing, H. Altenbach, J. Altenbach, and W. Kissing, "Classification of Composite Materials," in *Mechanics of Composite Structural Elements*, 2004, pp. 1–14.

[17] D. K. Rajak, D. D. Pagar, P. L. Menezes, and E. Linul, "Fiber-reinforced polymer composites: Manufacturing, properties, and applications," *Polymers*, vol. 11, no. 10. 2019, doi: 10.3390/polym11101667.

[18] R. M. Christensen, "Mechanical Properties of Composite Materials.," 1983, pp. 1–16, doi: 10.1016/b978-0-08-029384-4.50008-0.

[19] N. Gupta, S. E. Zeltmann, V. C. Shunmugasamy, and D. Pinisetty, "Applications of polymer matrix syntactic foams," *Jom*, vol. 66, no. 2, pp. 245–254, 2014, doi: 10.1007/s11837-013-0796-8.

[20] C. Soutis, "Carbon fiber reinforced plastics in aircraft construction," *Mater. Sci. Eng. A* vol. 412, no. 1–2, pp. 171–176, 2005, doi: 10.1016/j.msea.2005.08.064.

[21] R. A. Hawileh, A. Abu-Obeidah, J. A. Abdalla, and A. Al-Tamimi, "Temperature effect on the mechanical properties of carbon, glass, and carbon-glass FRP laminates," *Constr. Build. Mater.*, vol. 75, pp. 342–348, 2015, doi:

10.1016/j.conbuildmat.2014.11.020.

[22]   R. Her, J. Renard, V. Gaffard, Y. Favry, and P. Wiet, "Design of pipeline composite repairs: From lab-scale tests to fea and full-scale testing," in *Proceedings of the Biennial International Pipeline Conference, IPC*, 2014, vol. 2, doi: 10.1115/IPC201433201.

[23]   P. Morampudi, K. K. Namala, Y. K. Gajjela, M. Barath, and G. Prudhvi, "Review on glass fiber reinforced polymer composites," *Mater. Today Proc.*, no. ISSN 2214-7853, 2021, doi: 10.1016/j.matpr.2020.11.669.

[24]   S. G. Maxineasa and N. Taranu, "Life cycle analysis of strengthening concrete beams with FRP," in *Eco-efficient Repair and Rehabilitation of Concrete Infrastructures*, 2018, pp. 673–721.

[25]   "ISO 14692, Standard: petroleum and natural gas industries - glass-reinforced plastics (GRP) piping. Part 1: vocabulary, symbols, applications, and materials; Part 2: qualification and manufacture; Part 3: system design; Part 4: fabrication, installation an," 2017.

[26]   W. K. Goertzen and M. R. Kessler, "Dynamic mechanical analysis of carbon/epoxy composites for structural pipeline repair," *Compos. Part B Eng.*, vol. 38, no. 1, pp. 1–9, 2007, doi: 10.1016/j.compositesb.2006.06.002.

[27]   L. S. Lee and H. Estrada, "Time-dependent probability analysis of fiber-reinforced polymer rehabilitated pipes," in *Rehabilitation of Pipelines Using Fiber-reinforced Polymer (FRP) Composites*, 2015, pp. 79–100.

[28]   D. Kong, X. Huang, M. Xin, and G. Xian, "Effects of defect dimensions and putty properties on the burst performances of steel pipes wrapped with CFRP

composites," *Int. J. Press. Vessel. Pip.*, vol. 186, 2020, doi: 10.1016/j.ijpvp.2020.104139.

[29] P. C. Varelidis, D. G. Papakostopoulos, C. I. Pandazis, and C. D. Papaspyrides, "Polyamide coated KevlarTM fabric in epoxy resin: Mechanical properties and moisture absorption studies," *Compos. Part A Appl. Sci. Manuf.*, vol. 31, no. 6, pp. 549–558, 2000, doi: 10.1016/S1359-835X(99)00101-3.

[30] M. P. Kruijer, L. L. Warnet, and R. Akkerman, "Analysis of the mechanical properties of a reinforced thermoplastic pipe (RTP)," in *Composites Part A: Applied Science and Manufacturing*, 2005, vol. 36, no. 2 SPEC. ISS., pp. 291–300, doi: 10.1016/j.compositesa.2004.06.018.

[31] G. Qi *et al.*, "Experimental study on the thermostable property of aramid fiber reinforced PE-RT pipes," *Nat. Gas Ind. B*, vol. 2, no. 5, pp. 461–466, 2015, doi: 10.1016/j.ngib.2015.09.023.

[32] M. H. Farag and E. Mahdi, "New approach of pipelines joining using fiber reinforced plastics composites," *Composite Structures*, vol. 228. 2019, doi: 10.1016/j.compstruct.2019.111341.

[33] M. Akay, S. Kong Ah Mun, and A. Stanley, "Influence of moisture on the thermal and mechanical properties of autoclaved and oven-cured Kevlar-49/epoxy laminates," *Compos. Sci. Technol.*, vol. 57, no. 5, pp. 565–571, 1997, doi: 10.1016/S0266-3538(97)00017-1.

[34] J. H. Greenwood and P. G. Rose, "Compressive behavior of Kevlar 49 fibers and composites," *J. Mater. Sci.*, vol. 9, no. 11, pp. 1809–1814, 1974, doi: 10.1007/BF00541750.

[35] S. J. Deteresa, S. R. Allen, R. J. Farris, and R. S. Porter, "Compressive and torsional behavior of Kevlar 49 fiber," *J. Mater. Sci.*, vol. 19, no. 1, pp. 57–72, 1984, doi: 10.1007/BF02403111.

[36] R. E. Allred and D. K. Roylance, "Transverse moisture sensitivity of aramid/epoxy composites," *J. Mater. Sci.*, vol. 18, no. 3, pp. 652–656, 1983, doi: 10.1007/BF00745562.

[37] C. Chen *et al.*, "Eco-friendly and mechanically reliable alternative to synthetic FRP in the externally bonded strengthening of RC beams: Natural FRP," *Compos. Struct.*, vol. 241, 2020, doi: 10.1016/j.compstruct.2020.112081.

[38] S. V. Joshi, L. T. Drzal, A. K. Mohanty, and S. Arora, "Are natural fiber composites environmentally superior to glass fiber reinforced composites?," in *Composites Part A: Applied Science and Manufacturing*, 2004, vol. 35, no. 3, pp. 371–376, doi: 10.1016/j.compositesa.2003.09.016.

[39] B. Dan-asabe, "Thermo-mechanical characterization of banana particulate reinforced PVC composite as a piping material," *J. King Saud Univ. - Eng. Sci.*, vol. 30, no. 4, pp. 296–304, 2018, doi: 10.1016/j.jksues.2016.11.001.

[40] B. Dan-asabe, S. A. Yaro, and D. S. Yawas, "Microstructural and mechanical characterization of doum-palm leaves particulate reinforced PVC composite as piping materials," *Alexandria Eng. J.*, vol. 57, no. 4, pp. 2929–2937, 2018, doi: 10.1016/j.aej.2018.07.007.

[41] S. Q. Shi, L. Cai, Y. Weng, D. Wang, and Y. Sun, "Comparative life-cycle assessment of water supply pipes made from bamboo vs. polyvinyl chloride," *J. Clean. Prod.*, vol. 240, 2019, doi: 10.1016/j.jclepro.2019.118172.

[42] B. S. K. Ganesh D.Shrigandhi, "Biodegradable composites for filament winding process," *Mater. Today Proc.*, 2021.

[43] S. Panthapulakkal, L. Raghunanan, M. Sain, B. Kc, and J. Tjong, "Natural fiber and hybrid fiber thermoplastic composites: Advancements in lightweighting applications," in *Green Composites: Waste and Nature-based Materials for a Sustainable Future: Second Edition*, 2017, pp. 39–72.

[44] A. B. M. Supian, S. M. Sapuan, M. Y. M. Zuhri, E. S. Zainudin, and H. H. Ya, "Hybrid reinforced thermoset polymer composite in energy absorption tube application: A review," *Defence Technology*, vol. 14, no. 4. pp. 291–305, 2018, doi: 10.1016/j.dt.2018.04.004.

[45] A. Panigrahi and S. R. Mallick, "Characterization of Hybrid FRP Composites With Hygrothermal Exposure Under Varied Ambient Conditions," 2009.

[46] Y. Swolfs, L. Gorbatikh, and I. Verpoest, "Fibre hybridisation in polymer composites: A review," *Composites Part A: Applied Science and Manufacturing*, vol. 67. pp. 181–200, 2014, doi: 10.1016/j.compositesa.2014.08.027.

[47] Z. Li, X. Jiang, H. Hopman, L. Zhu, and Z. Liu, "External surface cracked offshore steel pipes reinforced with composite repair system subjected to cyclic bending: An experimental investigation," *Theor. Appl. Fract. Mech.*, vol. 109, 2020, doi: 10.1016/j.tafmec.2020.102703.

[48] C. Dong, "Flexural behaviour of carbon and glass reinforced hybrid composite pipes," *Compos. Part C Open Access*, vol. 4, no. ISSN 2666-3597, p. 100090, 2021, doi: 10.1016/j.jcomc.2020.100090.

[49] C. Dong, "Optimal design of carbon and glass reinforced hybrid composite pipes

under flexural loading," *Forces Mech.*, vol. 2, no. ISSN 2666-3597, p. 100003, 2021, doi: 10.1016/j.finmec.2020.100003.

[50] J. M. George, M. Kimiaei, M. Elchalakani, and S. Fawzia, "Experimental and numerical investigation of underwater composite repair with fibre reinforced polymers in corroded tubular offshore structural members under concentric and eccentric axial loads," *Eng. Struct.*, vol. 227, 2021, doi: 10.1016/j.engstruct.2020.111402.

[51] "Composite repair system increases pipe service life," *Seal. Technol.*, vol. 2014, no. 12, pp. 4–5, 2014, doi: 10.1016/s1350-4789(14)70437-4.

[52] D. Kr Singh, A. Villamayor, and A. Hazra, "Numerical and experimental analysis of loctite adhesive composite wrapping on EN 10028 steel pipe," *Mater. Today Proc.*, 2020, doi: 10.1016/j.matpr.2020.10.525.

[53] C. Santulli, "Mechanical and impact damage analysis on carbon/natural fibers hybrid composites: A review," *Materials (Basel).*, vol. 12, no. 3, p. 517, 2019, doi: 10.3390/ma12030517.

[54] J. M. C. Cadei, "Fatigue of FRP composites in civil engineering applications," in *Fatigue in Composites*, 2003, pp. 658–685.

[55] L. Gemi, M. Kayrıcı, M. Uludağ, D. S. Gemi, and Ö. S. Şahin, "Experimental and statistical analysis of low velocity impact response of filament wound composite pipes," *Compos. Part B Eng.*, vol. 149, pp. 38–48, 2018, doi: 10.1016/j.compositesb.2018.05.006.

[56] L. Zu, H. Xu, B. Zhang, D. Li, and B. Zi, "Design of filament-wound composite structures with arch-shaped cross sections considering fiber tension simulation,"

Compos. Struct., vol. 194, pp. 119–125, 2018, doi: 10.1016/j.compstruct.2018.04.018.

[57] M. Quanjin, M. R. M. Rejab, N. M. Kumar, and M. N. M. Merzuki, "Robotic Filament Winding Technique (RFWT) in Industrial Application: A Review of State of the Art and Future Perspectives," *Int. Res. J. Eng. Technol.*, p. 1668, 2008, [Online]. Available: www.irjet.net.

[58] Q. Wang, T. Li, B. Wang, C. Liu, Q. Huang, and M. Ren, "Prediction of void growth and fiber volume fraction based on filament winding process mechanics," *Compos. Struct.*, vol. 246, 2020, doi: 10.1016/j.compstruct.2020.112432.

[59] F. H. Abdalla *et al.*, "Design and fabrication of low cost filament winding machine," *Mater. Des.*, vol. 28, no. 1, pp. 234–239, 2007, doi: 10.1016/j.matdes.2005.06.015.

[60] M. Quanjin, M. R. M. Rejab, N. M. Kumar, and M. S. Idris, "Experimental assessment of the 3-axis filament winding machine performance," *Results Eng.*, vol. 2, 2019, doi: 10.1016/j.rineng.2019.100017.

[61] E. Vargas Rojas, D. Chapelle, D. Perreux, B. Delobelle, and F. Thiebaud, "Unified approach of filament winding applied to complex shape mandrels," *Compos. Struct.*, vol. 116, no. 1, pp. 805–813, 2014, doi: 10.1016/j.compstruct.2014.06.009.

[62] L. Sorrentino, M. Marchetti, C. Bellini, A. Delfini, and F. Del Sette, "Manufacture of high performance isogrid structure by Robotic Filament Winding," *Compos. Struct.*, vol. 164, pp. 43–50, 2017, doi:

10.1016/j.compstruct.2016.12.061.

[63] I. Koustas, T. Papingiotis, G. C. Vosniakos, and A. Dine, "On the development of a filament winding robotic system," in *Procedia Manufacturing*, 2018, vol. 17, pp. 919–926, doi: 10.1016/j.promfg.2018.10.145.

[64] P. Mertiny and F. Ellyin, "Influence of the filament winding tension on physical and mechanical properties of reinforced composites," *Compos. Part A Appl. Sci. Manuf.*, vol. 33, no. 12, pp. 1615–1622, 2002, doi: 10.1016/S1359-835X(02)00209-9.

[65] F. Abdalla, M. Megat, M. Sapuan, and S. Bb, "Determination of Volume Fraction Values Of Filament Wound Glass and Carbon Fiber Reinforced Composites," *ARPN J Eng Appl Sci*, vol. 3, no. 4, pp. 7–11, 2008, [Online]. Available:

http://www.arpnjournals.com/jeas/research_papers/rp_2008/jeas_0808_109.pdf

.

[66] P. D. Soden, R. Kitching, P. C. Tse, Y. Tsavalas, and M. J. Hinton, "Influence of winding angle on the strength and deformation of filament-wound composite tubes subjected to uniaxial and biaxial loads," *Compos. Sci. Technol.*, vol. 46, no. 4, pp. 363–378, 1993, doi: 10.1016/0266-3538(93)90182-G.

[67] J. S. Park, C. S. Hong, C. G. Kim, and C. U. Kim, "Analysis of filament wound composite structures considering the change of winding angles through the thickness direction," *Compos. Struct.*, vol. 55, no. 1, pp. 63–71, 2002, doi: 10.1016/S0263-8223(01)00137-4.

[68] B. Spencer and D. Hull, "Effect of winding angle on the failure of filament

wound pipe," *Composites*, vol. 9, no. 4, pp. 263–271, 1978, doi: 10.1016/0010-4361(78)90180-5.

[69]   P. Mertiny, F. Ellyin, and A. Hothan, "An experimental investigation on the effect of multi-angle filament winding on the strength of tubular composite structures," *Compos. Sci. Technol.*, vol. 64, no. 1, pp. 1–9, 2004, doi: 10.1016/S0266-3538(03)00198-2.

[70]   A. F. Hamed, Y. A. Khalid, S. M. Sapuan, M. M. Hamdan, T. S. Younis, and B. B. Sahari, "Effects of winding angles on the strength of filament wound composite tubes subjected to different loading modes," *Polym. Polym. Compos.*, vol. 15, no. 3, pp. 199–206, 2007, doi: 10.1177/096739110701500304.

[71]   C. Colombo and L. Vergani, "Optimization of filament winding parameters for the design of a composite pipe," *Compos. Part B Eng.*, vol. 148, pp. 207–216, 2018, doi: 10.1016/j.compositesb.2018.04.056.

[72]   J. Ramôa Correia, "Pultrusion of advanced fibre-reinforced polymer (FRP) composites," in *Advanced Fibre-Reinforced Polymer (FRP) Composites for Structural Applications*, 2013, pp. 207–251.

[73]   A. M. Fairuz, S. M. Sapuan, E. S. Zainudin, and C. N. A. Jaafar, "Polymer composite manufacturing using a pultrusion process: A review," *Am. J. Appl. Sci.*, vol. 11, no. 10, pp. 1798–1810, 2014, doi: 10.3844/ajassp.2014.1798.1810.

[74]   S. C. Joshi, "The pultrusion process for polymer matrix composites," in *Manufacturing Techniques for Polymer Matrix Composites (PMCs): A Volume in Woodhead Publishing Series in Composites Science and Engineering*, 2012, pp. 381–413.

[75] P. J. Novo, J. F. Silva, J. P. Nunes, and A. T. Marques, "Pultrusion of fibre reinforced thermoplastic pre-impregnated materials," *Compos. Part B Eng.*, vol. 89, pp. 328–339, 2016, doi: 10.1016/j.compositesb.2015.12.026.

[76] K. Van De Velde and P. Kiekens, "Thermoplastic pultrusion of natural fibre reinforced composites," *Compos. Struct.*, vol. 54, no. 2–3, pp. 355–360, 2001, doi: 10.1016/S0263-8223(01)00110-6.

[77] S. P. Rawal and J. W. Goodman, "Composites for Spacecraft," in *Comprehensive Composite Materials*, 2000, pp. 279–315.

[78] G. Bechtold, S. Wiedmer, and K. Friedrich, "Pultrusion of thermoplastic composites - New developments and modelling studies," *J. Thermoplast. Compos. Mater.*, vol. 15, no. 5, pp. 443–465, 2002, doi: 10.1177/0892705702015005202.

[79] T. Q. Liu, X. Liu, and P. Feng, "A comprehensive review on mechanical properties of pultruded FRP composites subjected to long-term environmental effects," *Composites Part B: Engineering*, vol. 191. 2020, doi: 10.1016/j.compositesb.2020.107958.

[80] "Manufacturing of fibre–polymer composite materials," in *Introduction to Aerospace Materials*, 2012, pp. 303–337.

[81] B. T. Åström, *Manufacturing of Polymer Composites*. 2018.

[82] A. L. Kalamkarov, S. B. Fitzgerald, and D. O. MacDonald, "Use of Fabry Perot fiber optic sensors to monitor residual strains during pultrusion of FRP composites," *Compos. Part B Eng.*, vol. 30, no. 2, pp. 167–175, 1999, doi: 10.1016/S1359-8368(98)00052-3.

[83] Milan, "Top glass company." https://www.topglass.it/en/technologies/pullwinding/.

[84] China, "Unicomposite company." https://www.unicomposite.com/products/product/.

[85] Denmark, "Carbonprofiles company." https://www.carbonprofiles.dk/composites/pullwinding.aspx.

[86] A. A. Abd-Elhady, H. E. D. M. Sallam, I. M. Alarifi, R. A. Malik, and T. M. A. A. EL-Bagory, "Investigation of fatigue crack propagation in steel pipeline repaired by glass fiber reinforced polymer," *Compos. Struct.*, vol. 242, 2020, doi: 10.1016/j.compstruct.2020.112189.

[87] M. Shamsuddoha, M. M. Islam, T. Aravinthan, A. Manalo, and K. tak Lau, "Effectiveness of using fibre-reinforced polymer composites for underwater steel pipeline repairs," *Composite Structures*, vol. 100. pp. 40–54, 2013, doi: 10.1016/j.compstruct.2012.12.019.

[88] C. E. Bakis *et al.*, "Fiber-Reinforced Polymer Composites for Construction - State-of-the-Art Review," in *Perspectives in Civil Engineering: Commemorating the 150th Anniversary of the American Society of Civil Engineers*, 2003, pp. 369–383, doi: 10.1061/(asce)1090-0268(2002)6:2(73).

[89] M. Shamsuddoha, A. Manalo, T. Aravinthan, M. Mainul Islam, and L. Djukic, "Failure analysis and design of grouted fibre-composite repair system for corroded steel pipes," *Eng. Fail. Anal.*, vol. 119, 2021, doi: 10.1016/j.engfailanal.2020.104979.

[90] H. GangaRao, "Infrastructure Applications of Fiber-Reinforced Polymer

Composites," in *Applied Plastics Engineering Handbook*, 2011, pp. 565–584.

[91] H. Toutanji and S. Dempsey, "Stress modeling of pipelines strengthened with advanced composites materials," *Thin-Walled Struct.*, vol. 39, no. 2, pp. 153–165, 2001, doi: 10.1016/S0263-8231(00)00049-5.

[92] L. S. Lee, H. Estrada, and M. Baumert, "Time-Dependent Reliability Analysis of FRP Rehabilitated Pipes," *J. Compos. Constr.*, vol. 14, no. 3, pp. 272–279, 2010, doi: 10.1061/(asce)cc.1943-5614.0000075.

[93] C. Alexander and B. Francini, "State of the art assessment of composite systems used to repair transmission pipelines," in *Proceedings of the Biennial International Pipeline Conference, IPC*, 2007, vol. 1, pp. 823–830, doi: 10.1115/IPC2006-10484.

[94] B. Capeska, S., Risteska, S., Samak, S., & Kostadinoska, "Impact of the technological parameters for the production of UD prepreg," *Knowledge-International Journal, Sci. Pap.*, vol. 20, no. 5, 2017.

[95] L. M. Wei Zhou, Xiao-long Ji, Sa Yang, Jia Liu, "Review on the performance improvements and non-destructive testingof patches repaired composites," *Compos. Struct.*, vol. 263, 2021.

[96] G. Li, D. Davis, C. Stewart, J. Peck, and S. S. Pang, "Joining Composite Pipes Using Hybrid Prepreg Welding and Adhesive Bonding," *Polym. Compos.*, vol. 24, no. 6, pp. 697–705, 2003, doi: 10.1002/pc.10063.

[97] M. Meriem-Benziane, S. A. Abdul-Wahab, H. Zahloul, B. Babaziane, M. Hadj-Meliani, and G. Pluvinage, "Finite element analysis of the integrity of an API X65 pipeline with a longitudinal crack repaired with single- and double-bonded

composites," *Compos. Part B Eng.*, vol. 77, pp. 431–439, 2015, doi: 10.1016/j.compositesb.2015.03.008.

[98] J. Liu, M. Qin, Q. Zhao, L. Chen, P. Liu, and J. Gao, "Fatigue performances of the cracked aluminum-alloy pipe repaired with a shaped CFRP patch," *Thin-Walled Struct.*, vol. 111, pp. 155–164, 2017, doi: 10.1016/j.tws.2016.11.008.

[99] "The Clock Spring Company," *Clock Spring® product brochure*, 2012. https://www.clockspring.com/wp-content/uploads/2011/12/brochure1.pdf.

[100] Ł. Mazurkiewicz, J. Małachowski, M. Tomaszewski, P. Baranowski, and P. Yukhymets, "Performance of steel pipe reinforced with composite sleave," *Compos. Struct.*, vol. 183, no. 1, pp. 199–211, 2018, doi: 10.1016/j.compstruct.2017.02.032.

[101] S. Beckwith and M. Greenwood, "Don't overlook composite FRP pipe: satisfying hydraulic and fluid are key considerations in the efficient design of FRP piping systems," *Chem. Eng.*, vol. 113, no. 5, pp. 42–49, 2006.

[102] R. Barrett-Gonzalez, S. Rolfe, A. Matamoros, and C. Bennett, "Extending the fatigue life of steel bridges using fiber-reinforced polymer (FRP) composites," in *Rehabilitation of Metallic Civil Infrastructure Using Fiber Reinforced Polymer (FRP) Composites: Types Properties and Testing Methods*, 2014, pp. 269–319.

[103] M. Dawood, "Durability of steel components strengthened with fiber-reinforced polymer (FRP) composites," in *Rehabilitation of Metallic Civil Infrastructure Using Fiber Reinforced Polymer (FRP) Composites: Types Properties and Testing Methods*, 2014, pp. 96–114.

[104] K. A. Harries, "Enhancing the stability of structural steel components using fibre-reinforced polymer (FRP) composites," in *Rehabilitation of Metallic Civil Infrastructure Using Fiber Reinforced Polymer (FRP) Composites: Types Properties and Testing Methods*, 2014, pp. 117–139.

[105] Z. Liu and Y. Kleiner, "State of the art review of inspection technologies for condition assessment of water pipes," *Measurement: Journal of the International Measurement Confederation*, vol. 46, no. 1. pp. 1–15, 2013, doi: 10.1016/j.measurement.2012.05.032.

[106] E. K. Arthur, E. Gikunoo, F. O. Agyemang, S. T. Azeko, A. Andrews, and A. Twenewaa, "Material Selection for Water Pipes by the Multi-Objective Decision-Making Method: The Case of Alternative Materials for PVC Pipes," *J. Sci. Technol.*, vol. 5, no. 1, pp. 29–42, 2020, [Online]. Available: www.jst.org.in.

[107] N. Ampiah, A. Fam, and I. D. Moore, "Effect of Wrinkles on the Circumferential Strength of a Cast-in-Place Composite Polymer Liner Used in Retrofitting Pressure Pipes," *J. Mater. Civ. Eng.*, vol. 22, no. 12, pp. 1304–1314, 2010, doi: 10.1061/(asce)mt.1943-5533.0000160.

[108] "Hydroelectric plant employs FRP pipes," *Reinf. Plast.*, vol. 51, no. 9, p. 6, 2007, doi: 10.1016/s0034-3617(07)70259-x.

[109] H. GangaRao, "Infrastructure Applications of Fiber-Reinforced Polymer Composites," in *Applied Plastics Engineering Handbook: Processing, Materials, and Applications: Second Edition*, 2017, pp. 675–695.

[110] M. J.Al-Mahfooz and E. Mahdi, "Bending behavior of glass fiber reinforced composite overwrapping pvc plastic pipes," *Composite Structures*, vol. 251.

2020, doi: 10.1016/j.compstruct.2020.112656.

[111] C. Affolter, M. Barbezat, G. Piskoty, O. Neuner, and G. Terrasi, "Failure of a sag water pipe triggered by aging of the GFRP composite relining," *Eng. Fail. Anal.*, vol. 84, pp. 358–370, 2018, doi: 10.1016/j.engfailanal.2017.09.017.

[112] R. Rafiee, F. Reshadi, and S. Eidi, "Stochastic analysis of functional failure pressures in glass fiber reinforced polyester pipes," *Mater. Des.*, vol. 67, pp. 422–427, 2015, doi: 10.1016/j.matdes.2014.12.003.

[113] R. Rafiee and A. Amini, "Modeling and experimental evaluation of functional failure pressures in glass fiber reinforced polyester pipes," *Comput. Mater. Sci.*, vol. 96, no. PB, pp. 579–588, 2015, doi: 10.1016/j.commatsci.2014.03.036.

[114] H. Hu, T. Dou, F. Niu, H. Zhang, and W. Su, "Experimental and numerical study on CFRP-lined prestressed concrete cylinder pipe under internal pressure," *Eng. Struct.*, vol. 190, pp. 480–492, 2019, doi: 10.1016/j.engstruct.2019.03.106.

[115] R. Jain and L. Lee, *Fiber reinforced polymer (FRP) composites for infrastructure applications: Focusing on innovation, technology implementation and sustainability*. 2012.

[116] "FRP liner used to repair LA sewer pipe," *Reinf. Plast.*, vol. 52, no. 9, p. 8, 2008, doi: 10.1016/s0034-3617(08)70320-5.

[117] E. Vahidi, E. Jin, M. Das, M. Singh, and F. Zhao, "Environmental life cycle analysis of pipe materials for sewer systems," *Sustain. Cities Soc.*, vol. 27, pp. 167–174, 2016, doi: 10.1016/j.scs.2016.06.028.

[118] R. Kakaei and M. Hajiazizi, "The effect of GFRP on reinforcing the buried and internally pressurized steel pipes against terrorist attacks," *Int. J. Press. Vessel.*

Pip., vol. 189, 2021, doi: 10.1016/j.ijpvp.2020.104273.

[119] E. Mahdi and E. Eltai, "Development of cost-effective composite repair system for oil/gas pipelines," *Compos. Struct.*, vol. 202, pp. 802–806, 2018, doi: 10.1016/j.compstruct.2018.04.025.

[120] J. Conley, B. Weller, and E. Slingerland, "The use of reinforced thermoplastic pipe in oil and gas gathering and produced water pipelines," in *Society of Petroleum Engineers - SPE Gas Technology Symposium*, 2008, vol. 1, pp. 50–56, doi: 10.2118/113718-ms.

[121] X. Zhang, H. Li, D. Qi, Q. Li, N. Ding, and X. Cai, "Failure analysis of anticorrosion plastic alloy composite pipe used for oilfield gathering and transportation," *Eng. Fail. Anal.*, vol. 32, pp. 35–43, 2013, doi: 10.1016/j.engfailanal.2013.03.001.

[122] C. and Alexander and J. Bedoya, "An Updated Perspective on Using Composite Materials to Reinforce Offshore Pipelinesand Risers," in *Proceeding of the 6th International offshore Pipeline Forum IOPF 2011*, 2011, p. 18, [Online]. Available: http://armorplateinc.com/uploads/2011 Oct - Alexander, C., et al - IOPF2011-7002-Houston.pdf.

[123] C. Alexander, L. Cercone, and J. Lockwood, "Development of a carbon-fiber composite repair system for offshore risers," Texas A&M University, 2008.

[124] M. D. Hurlimann, "Development of A Composite Repair Syatem For reinforcing Offshore Risers," *Combust. Sci. Technol.*, vol. 21, no. 5–6, pp. 1–49, 2007, [Online]. Available: https://doi.org/10.1080/00102208008946937.

[125] C. Alexander, L. Cercone, and J. Lockwood, "Development of a carbon-fiber

composite repair system for offshore risers," in *Proceedings of the International Conference on Offshore Mechanics and Arctic Engineering - OMAE*, 2008, vol. 5, pp. 389–405, doi: 10.1115/OMAE2008-57599.

[126] T. A. Anderson *et al.*, "Progress in the development of test methods and flexible composite risers for 3000 m water depths," in *Proceedings of the Annual Offshore Technology Conference*, 2016, vol. 5, pp. 4236–4250, doi: 10.4043/27260-ms.

[127] A. Rowe and C. Alexander, "The use of composite materials in repairing and reinforcing pipelines, piping, and structures," in *Proceedings - SPE Annual Technical Conference and Exhibition*, 2008, vol. 6, pp. 3771–3793, doi: 10.2118/116280-ms.

[128] S. Ahankari and A. Patil, "Sea Water Effect on Mechanical Performance of Steel Pipes Rehabilitated with Glass Fiber Reinforced Epoxy Composites," in *Materials Today: Proceedings*, 2019, vol. 22, pp. 2490–2498, doi: 10.1016/j.matpr.2020.03.377.

[129] C. Alexander and O. O. Ochoa, "Extending onshore pipeline repair to offshore steel risers with carbon-fiber reinforced composites," *Compos. Struct.*, vol. 92, no. 2, pp. 499–507, 2010, doi: 10.1016/j.compstruct.2009.08.034.

[130] C. P. Pantelides, "Rehabilitation of cracked aluminum components using fiber-reinforced polymer (FRP) composites," in *Rehabilitation of Metallic Civil Infrastructure Using Fiber Reinforced Polymer (FRP) Composites: Types Properties and Testing Methods*, 2014, pp. 201–214.

[131] Y. D. Boon, S. C. Joshi, and L. S. Ong, "Effects of Mechanical Surface

Treatment on Bonding between Aluminum and Carbon/Epoxy Composites," *Procedia Engineering*, 2017, vol. 184, pp. 552–559, doi: 10.1016/j.proeng.2017.04.134.

[132] H. Zarrinzadeh, M. Z. Kabir, and A. Deylami, "Experimental and numerical fatigue crack growth of an aluminium pipe repaired by composite patch," *Eng. Struct.*, vol. 133, pp. 24–32, 2017, doi: 10.1016/j.engstruct.2016.12.011.

[133] M. Stamenović, S. Putić, M. Rakin, B. Medjo, and D. Čikara, "Effect of alkaline and acidic solutions on the tensile properties of glass-polyester pipes," *Mater. Des.*, vol. 32, no. 4, pp. 2456–2461, 2011, doi: 10.1016/j.matdes.2010.11.023.

[134] M. K. Mahmoud and S. H. Tantawi, "Effect of strong acids on mechanical properties of glass/polyester GRP pipe at normal and high temperatures," *Polym. - Plast. Technol. Eng.*, vol. 42, no. 4, pp. 677–688, 2003, doi: 10.1081/PPT-120023102.

[135] K. Sindhu, K. Joseph, J. M. Joseph, and T. V. Mathew, "Degradation studies of coir fiber/polyester and glass fiber/polyester composites under different conditions," *J. Reinf. Plast. Compos.*, vol. 26, no. 15, pp. 1571–1585, 2007, doi: 10.1177/0731684407079665.

[136] "FRP products suitable for chemical service," *Reinforced Plastics*, vol. 60, no. 4. p. 184, 2016, doi: 10.1016/j.repl.2016.06.016.

[137] F. G. Al-Abtah, E. Mahdi, and S. Gowid, "The use of composite to eliminate the effect of welding on the bending behavior of metallic pipes," *Compos. Struct.*, 2020, doi: 10.1016/j.compstruct.2019.111793.

[138] M. H. Farag and E. Mahdi, "New approach of pipelines joining using fiber

reinforced plastics composites," *Composite Structures*. 2019, doi: 10.1016/j.compstruct.2019.111341.

[139] D. R. Haider *et al.*, "Adhesion Studies of Thermoplastic Fibre-Plastic Composite Hybrid Components Part 2: Thermoplastic-Metal-Composites," 2018.

[140] S. Farahani, V. A. Yerra, and S. Pilla, "Analysis of a hybrid process for manufacturing sheet metal-polymer structures using a conceptual tool design and an analytical-numerical modelling," *J. Mater. Process. Technol.*, 2020, doi: 10.1016/j.jmatprotec.2019.116533.

[141] R. Mohammadi, M. A. Najafabadi, H. Saghafi, and D. Zarouchas, "Mode-II fatigue response of AS4/8552 carbon /epoxy composite laminates interleaved by electrospun nanofibers," *Thin-Walled Struct.*, 2020, doi: 10.1016/j.tws.2020.106811.

[142] R. C. Alderliesten, "Designing for damage tolerance in aerospace: A hybrid material technology," *Mater. Des.*, 2015, doi: 10.1016/j.matdes.2014.06.068.

[143] O. Laban and E. Mahdi, "Enhancing mode I inter-laminar fracture toughness of aluminum/fiberglass fiber-metal laminates by combining surface pre-treatments," *Int. J. Adhes. Adhes.*, 2017, doi: 10.1016/j.ijadhadh.2017.08.008.

[144] B. D. Davidson, R. Krüger, and M. König, "Three-dimensional analysis of center-delaminated unidirectional and multidirectional single-leg bending specimens," *Compos. Sci. Technol.*, 1995, doi: 10.1016/0266-3538(95)00069-0.

[145] I. De Baere, S. Jacques, W. Van Paepegem, and J. Degrieck, "Study of the mode i and mode II interlaminar behaviour of a carbon fabric reinforced thermoplastic," *Polym. Test.*, 2012, doi: 10.1016/j.polymertesting.2011.12.009.

[146] C. Mildner, "Numerical and experimental investigations of the crash behavior of FRP-reinforced metal structural components." Technical University of Munich., 2013.

[147] C. Liu *et al.*, "Study on mode-I fracture toughness of composite laminates with curved plies applied by automated fiber placement," *Mater. Des.*, 2020, doi: 10.1016/j.matdes.2020.108963.

[148] M. M. Shokrieh, A. Zeinedini, and S. M. Ghoreishi, "On the mixed-mode I/II delamination R-curve of E-glass/epoxy laminated composites," *Compos. Struct.*, 2017, doi: 10.1016/j.compstruct.2017.03.017.

[149] E. Jahanian and A. Zeinedini, "Influence of drilling on mode II delamination of E-glass/epoxy laminated composites," *Theor. Appl. Fract. Mech.*, 2018, doi: 10.1016/j.tafmec.2018.06.002.

[150] K. Saravanakumar, N. Farouk, and V. Arumugam, "Effect of fiber orientation on Mode-I delamination resistance of glass/epoxy laminates incorporated with milled glass fiber fillers," *Eng. Fract. Mech.*, 2018, doi: 10.1016/j.engfracmech.2018.05.027.

[151] E. Moradi and A. Zeinedini, "On the mixed mode I/II/III inter-laminar fracture toughness of cotton/epoxy laminated composites," *Theor. Appl. Fract. Mech.*, 2020, doi: 10.1016/j.tafmec.2019.102400.

[152] A. Kurtovic, E. Brandl, T. Mertens, and H. J. Maier, "Laser induced surface nano-structuring of Ti-6Al-4V for adhesive bonding," *Int. J. Adhes. Adhes.*, 2013, doi: 10.1016/j.ijadhadh.2013.05.004.

[153] N. Choupani, "Experimental and numerical investigation of the mixed-mode

delamination in Arcan laminated specimens," *Mater. Sci. Eng. A*, 2008, doi: 10.1016/j.msea.2007.05.103.

[154] N. Fantuzzi, R. Dimitri, and F. Tornabene, "A SFEM-based evaluation of mode-I Stress Intensity Factor in composite structures," *Compos. Struct.*, 2016, doi: 10.1016/j.compstruct.2016.02.076.

[155] ASTM Standard, "Standard E399: Standard Test Method for Linear-Elastic Plane-Strain Fracture Toughness KIC of Metallic Materials," *Annu. B. ASTM Stand.*, 2009.

[156] S. K. Sharma and S. Maheshwari, "A review on welding of high strength oil and gas pipeline steels," *Journal of Natural Gas Science and Engineering*, vol. 38. pp. 203–217, 2017, doi: 10.1016/j.jngse.2016.12.039.

[157] E. Mahdi, A. Rauf, and E. O. Eltai, "Effect of temperature and erosion on pitting corrosion of X100 steel in aqueous silica slurries containing bicarbonate and chloride content," *Corros. Sci.*, vol. 83, pp. 48–58, 2014, doi: 10.1016/j.corsci.2014.01.021.

[158] E. Eltai, K. Al-Khalifa, A. Al-Ryashi, E. Mahdi, and A. S. Hamouda, "Investigating the corrosion under insulation (CUI) on steel pipe exposed to Arabian Gulf sea water drops," in *Key Engineering Materials*, 2016, vol. 689, pp. 148–153, doi: 10.4028/www.scientific.net/KEM.689.148.

[159] A. Rauf, W. F. Bogaerts, and E. Mahdi, "Electrochemical frequency modulation method and its causality factors for corrosion monitoring," in *NACE - International Corrosion Conference Series*, 2012, vol. 7, pp. 5997–6010.

[160] J. F. Kiefner and C. J. Trench, "Oil Pipeline Characteristics and Risk Factors:

Illustrations from the Decade of Construction," *Am. Pet. Inst.*, no. December, 2001.

[161] A. P. Institute, *API 5L Specification for line pipe*, vol. Forty fift. 2012.

[162] "API Energy, Comparison of API Spec 5L 43rd Edition and ISO 3183, second edition, API Spec 5L 44th edition, 2008."

[163] "API, API 1104 Standard for Welding Pipelines and Related Facilities, Twentieth Edition, American Petroleum Institute, USA, 2005."

[164] T. N. G. Beavers John A, "External Corrosion of Oil and Natural Gas Pipelines," in *Corrosion: Environments and Industries*, 2018, pp. 1015–1025.

[165] Z. A. Majid, R. Mohsin, Z. Yaacob, and Z. Hassan, "Failure analysis of natural gas pipes," *Eng. Fail. Anal.*, vol. 17, no. 4, pp. 818–837, 2010, doi: 10.1016/j.engfailanal.2009.10.016.

[166] R. Datta, R. Veeraraghavan, and K. L. Rohira, "Weldability characteristics of torr and corrosion-resistant TMT bars using SMAW process," *J. Mater. Eng. Perform.*, vol. 11, no. 4, pp. 369–375, 2002, doi: 10.1361/105994902770343881.

[167] P. G. Fazzini, A. P. Cisilino, and J. L. Otegui, "Experimental validation of the influence of lamination defects in electrical resistance seam welded pipelines," *Int. J. Press. Vessel. Pip.*, vol. 82, no. 12, pp. 896–904, 2005, doi: 10.1016/j.ijpvp.2005.07.006.

[168] C. R. F. Azevedo, "Failure analysis of a crude oil pipeline," *Eng. Fail. Anal.*, vol. 14, no. 6 SPEC. ISS., pp. 978–994, 2007, doi: 10.1016/j.engfailanal.2006.12.001.

[169] R. D. Kane and J. B. Greer, "Sulfide Stress Cracking of High-Strength Steels in

Laboratory and Oilfield Environments.," *JPT, J. Pet. Technol.*, vol. 29, pp. 1483–1488, 1977, doi: 10.2118/6144-PA.

[170] P. G. Fazzini and J. L. Otegui, "Experimental determination of stress corrosion crack rates and service lives in a buried ERW pipeline," *Int. J. Press. Vessel. Pip.*, vol. 84, no. 12, pp. 739–748, 2007, doi: 10.1016/j.ijpvp.2007.05.008.

[171] M. A. Al-Anezi, S. Rao, and G. R. Lobley, "Pipeline failure by transit fatigue," *J. Fail. Anal. Prev.*, vol. 9, no. 1, pp. 35–38, 2009, doi: 10.1007/s11668-008-9201-2.

[172] K. A. Macdonald, A. Cosham, C. R. Alexander, and P. Hopkins, "Assessing mechanical damage in offshore pipelines - Two case studies," *Eng. Fail. Anal.*, vol. 14, no. 8 SPEC. ISS., pp. 1667–1679, 2007, doi: 10.1016/j.engfailanal.2006.11.074.

[173] R. Celin, J. Burja, and G. Kosec, "A comparison of as-welded and simulated heat affected zone (HAZ) microstructures," *Mater. Tehnol.*, vol. 50, no. 3, pp. 455–460, 2016, doi: 10.17222/mit.2016.006.

[174] M. R. Abd-Ali, Kadum Nabel, Ahmed, "Effect of Fiber Orientation Angles on Mechanical Behavior of Car Bumper Composite," *Kufa J. Eng. مجلة الكوفة الهندسية*, vol. 7, no. 3, pp. 27–37, 2016.

[175] Z. Sloderbach and J. Pajak, "Determination of ranges of components of heat affected zone including changes of structure," *Arch. Metall. Mater.*, vol. 60, no. 4, pp. 2607–2612, 2015, doi: 10.1515/amm-2015-0421.

[176] "ASM, Corrosion of Weldments, 2006, Pages 1-10."

[177] A. Rauf and E. Mahdi, "Studying and comparing the erosion-enhanced pitting

corrosion of X52 and X100 steels," *Int. J. Electrochem. Sci.*, vol. 7, no. 6, pp. 5692–5707, 2012, doi: 10.5339/qfarf.2012.eep56.

[178] P. Colegrove *et al.*, "Welding process impact on residual stress and distortion," *Sci. Technol. Weld. Join.*, vol. 14, no. 8, pp. 717–725, 2009, doi: 10.1179/136217109X406938.

[179] D. L. Olson, A. N. Lasseigne, M. Marya, and B. Mishra, "Weld Features that Differentiate Weld and Plate Corrosion," *Pract. Fail. Anal.*, vol. 3, no. 5, pp. 43–57, 2003, doi: 10.1361/152981503771816763.

[180] H. Ahmed, M. I. Abbas, and M. A. K. Shahen, "Girth Weld Fitness After Multiple SMAW Repairs.," *Pipeline & Gas Journal*, vol. 240, no. 1. pp. 83–85, 2013, [Online]. Available: http://search.ebscohost.com/login.aspx?direct=true&AuthType=ip,shib&db=buh&AN=85269648&site=ehost-live&scope=site&custid=s1123049.

[181] X. Gao, N. Tao, X. Yang, C. Wang, and F. Xu, "Quasi-static three-point bending and fatigue behavior of 3-D orthogonal woven composites," *Compos. Part B Eng.*, vol. 159, pp. 173–183, 2019, doi: 10.1016/j.compositesb.2018.09.077.

[182] H. S. da Costa Mattos, J. M. L. Reis, L. M. Paim, M. L. D. da Silva, R. Lopes Junior, and V. A. Perrut, "Failure analysis of corroded pipelines reinforced with composite repair systems," *Eng. Fail. Anal.*, vol. 59, pp. 223–236, 2016, doi: 10.1016/j.engfailanal.2015.10.007.

[183] P. H. Chan, K. Y. Tshai, M. Johnson, H. L. Choo, S. Li, and K. Zakaria, "Burst strength of carbon fibre reinforced polyethylene strip pipeline repair system - A numerical and experimental approach," *J. Compos. Mater.*, vol. 49, no. 6, pp.

749–756, 2015, doi: 10.1177/0021998314525652.

[184] N. Saeed, H. Ronagh, and A. Virk, "Composite repair of pipelines, considering the effect of live pressure-analytical and numerical models concerning ISO/TS 24817 and ASME PCC-2," *Compos. Part B Eng.*, vol. 58, pp. 605–610, 2014, doi: 10.1016/j.compositesb.2013.10.035.

[185] M. F. Köpple, S. Lauterbach, and W. Wagner, "Composite repair of through-wall defects in pipework - Analytical and numerical models concerning ISO/TS 24817," *Compos. Struct.*, vol. 95, pp. 173–178, 2013, doi: 10.1016/j.compstruct.2012.06.023.

[186] T. Gurunathan, S. Mohanty, and S. K. Nayak, "A review of the recent developments in biocomposites based on natural fibres and their application perspectives," *Composites Part A: Applied Science and Manufacturing*, vol. 77. pp. 1–25, 2015, doi: 10.1016/j.compositesa.2015.06.007.

[187] J. E. Green, "Overview of filament winding," *SAMPE J.*, vol. 37, no. 1, pp. 7–11, 2001.

[188] M. Babiak, M. Gaff, A. Sikora, and Š. Hysek, "Modulus of elasticity in three- and four-point bending of wood," *Composite Structures*, vol. 204. pp. 454–465, 2018, doi: 10.1016/j.compstruct.2018.07.113.

[189] R. Budynas and K. Nisbett, "Shigley's Mechanical Engineering Design, Ninth Edition," *McGraw Hill Inc.*, pp. 1–15, 2009.

[190] M. Kartal, R. Molak, M. Turski, S. Gungor, M. E. Fitzpatrick, and L. Edwards, "Determination of weld metal mechanical properties utilising novel tensile testing methods," in *Applied Mechanics and Materials*, 2007, vol. 7–8, pp. 127–

132, doi: 10.4028/www.scientific.net/AMM.7-8.127.

[191] N. Li, J. F. Gu, and P. H. Chen, "Fracture plane based failure criteria for fibre-reinforced composites under three-dimensional stress state," *Compos. Struct.*, vol. 204, pp. 466–474, 2018, doi: 10.1016/j.compstruct.2018.07.103.

[192] K. Sawada, T. Hara, M. Tabuchi, K. Kimura, and K. Kubushiro, "Microstructure characterization of heat affected zone after welding in Mod.9Cr-1Mo steel," *Mater. Charact.*, vol. 101, pp. 106–113, 2015, doi: 10.1016/j.matchar.2015.01.013.

[193] V. D. Azzi and S. W. Tsai, "Anisotropic strength of composites," *Exp. Mech.*, 1965, doi: 10.1007/bf02326292.

[194] S. W. Tsai and E. M. wu, "A General Theory of Strength for Anisotropic Materials," *J. Compos. Mater.*, 1971, doi: 10.1177/002199837100500106.

[195] M. Finšgar and J. Jackson, "Application of corrosion inhibitors for steels in acidic media for the oil and gas industry: A review," *Corrosion Science*. 2014, doi: 10.1016/j.corsci.2014.04.044.

[196] B. Fotovvati, N. Namdari, and A. Dehghanghadikolaei, "On coating techniques for surface protection: A review," *Journal of Manufacturing and Materials Processing*. 2019, doi: 10.3390/jmmp3010028.

[197] A. Khan *et al.*, "Designing and performance evaluation of polyelectrolyte multilayered composite smart coatings," *Prog. Org. Coatings*, 2019, doi: 10.1016/j.porgcoat.2019.105319.

[198] H. Lee, K. Neville, L. Henry, and K. Neville, *Handbook of epoxy resins*. 1982.

[199] P. H. Sung and C. Y. Lin, "Polysiloxane modified epoxy polymer networks - I.

Graft interpenetrating polymeric networks," *Eur. Polym. J.*, 1997, doi: 10.1016/S0014-3057(96)00214-5.

[200] S. Ananda Kumar, M. Alagar, and V. Mohan, "Studies on corrosion-resistant behavior of siliconized epoxy interpenetrating coatings over mild steel surface by electrochemical methods," *J. Mater. Eng. Perform.*, 2002, doi: 10.1361/105994902770344178.

[201] W. Li *et al.*, "Improved anti-corrosion performance of epoxy zinc rich coating on rusted steel surface with aluminum triphosphate as rust converter," *Prog. Org. Coatings*, 2019, doi: 10.1016/j.porgcoat.2019.06.049.

[202] S. Shreepathi, P. Bajaj, and B. P. Mallik, "Electrochemical impedance spectroscopy investigations of epoxy zinc rich coatings: Role of Zn content on corrosion protection mechanism," *Electrochim. Acta*, 2010, doi: 10.1016/j.electacta.2010.04.018.

[203] M. Jalili, M. Rostami, and B. Ramezanzadeh, "An investigation of the electrochemical action of the epoxy zinc-rich coatings containing surface modified aluminum nanoparticle," *Appl. Surf. Sci.*, 2015, doi: 10.1016/j.apsusc.2014.12.034.

[204] S. Zhou *et al.*, "Designing reduced graphene oxide/zinc rich epoxy composite coatings for improving the anticorrosion performance of carbon steel substrate," *Mater. Des.*, 2019, doi: 10.1016/j.matdes.2019.107694.

[205] S. González, F. Cáceres, V. Fox, and R. M. Souto, "Resistance of metallic substrates protected by an organic coating containing aluminum powder," *Prog. Org. Coatings*, 2003, doi: 10.1016/S0300-9440(03)00021-3.

[206] B. Nikravesh, B. Ramezanzadeh, A. A. Sarabi, and S. M. Kasiriha, "Evaluation of the corrosion resistance of an epoxy-polyamide coating containing different ratios of micaceous iron oxide/Al pigments," *Corros. Sci.*, 2011, doi: 10.1016/j.corsci.2011.01.045.

[207] C. Ge, X. Zhao, Y. Guo, J. Duan, and B. Hou, "Study on preparation of magnesium-rich composite coating and performance enhancement by graft modification of epoxy resin," *IEEE J. Sel. Top. Quantum Electron.*, 2019, doi: 10.1515/secm-2019-0009.

[208] R. H. Petrucci, W. S. Harwood, G. E. Herring, and J. Madura, *General Chemistry: Principles & Modern Applications*. 2013.

[209] J. González-Guzmán, J. J. Santana, S. González, and R. M. Souto, "Resistance of metallic substrates protected by an organic coating containing glass flakes," *Prog. Org. Coatings*, 2010, doi: 10.1016/j.porgcoat.2010.01.005.

[210] S. Sathiyanarayanan, S. Syed Azim, and G. Venkatachari, "Corrosion protection coating containing polyaniline glass flake composite for steel," *Electrochim. Acta*, 2008, doi: 10.1016/j.electacta.2007.09.015.

[211] W. Tian, L. Liu, F. Meng, Y. Liu, Y. Li, and F. Wang, "The failure behaviour of an epoxy glass flake coating/steel system under marine alternating hydrostatic pressure," *Corros. Sci.*, 2014, doi: 10.1016/j.corsci.2014.04.038.

[212] R. I. HOLLAND, "Use of potentiodynamic polarization technique for corrosion testing of dental alloys," *Eur. J. Oral Sci.*, 1991, doi: 10.1111/j.1600-0722.1991.tb01026.x.

[213] F. F. Eliyan, E. S. Mahdi, and A. Alfantazi, "Electrochemical evaluation of the

corrosion behaviour of API-X100 pipeline steel in aerated bicarbonate solutions," *Corros. Sci.*, 2012, doi: 10.1016/j.corsci.2012.01.015.

[214] "B. Boukamp, Equivalent Circuit User's Manual, second ed., University of Twente, Enschede, 1989."

[215] A. H. Alamri, "Localized corrosion and mitigation approach of steel materials used in oil and gas pipelines – An overview," *Engineering Failure Analysis*, vol. 116. 2020, doi: 10.1016/j.engfailanal.2020.104735.

[216] M. Javidi, R. Chamanfar, and S. Bekhrad, "Investigation on the efficiency of corrosion inhibitor in CO2 corrosion of carbon steel in the presence of iron carbonate scale," *J. Nat. Gas Sci. Eng.*, 2019, doi: 10.1016/j.jngse.2018.11.017.

[217] T. Thi Xuan Hang, T. A. Truc, T. H. Nam, V. K. Oanh, J. B. Jorcin, and N. Pébère, "Corrosion protection of carbon steel by an epoxy resin containing organically modified clay," *Surf. Coatings Technol.*, 2007, doi: 10.1016/j.surfcoat.2007.02.009.

[218] P. R. Roberge., *Handbook of corrosion engineering*, vol. 37, no. 09. McGraw-Hill, 2000.

[219] A. F. Baldissera and C. A. Ferreira, "Coatings based on electronic conducting polymers for corrosion protection of metals," *Prog. Org. Coatings*, 2012, doi: 10.1016/j.porgcoat.2012.05.004.

[220] E. O. Eltai, J. D. Scantlebury, and E. V. Koroleva, "The effects of zinc ions on the performance of epoxy coated mild steel under cathodic protection (CP)," *Prog. Org. Coatings*, 2013, doi: 10.1016/j.porgcoat.2012.11.006.

[221] A. Pradityana, Sulistijono, A. Shahab, L. Noerochim, and D. Susanti, "Inhibition

of Corrosion of Carbon Steel in 3.5% NaCl Solution by Myrmecodia Pendans Extract," *Int. J. Corros.*, 2016, doi: 10.1155/2016/6058286.

[222] E. O. Eltai, J. D. Scantlebury, and E. V. Koroleva, "The effects of different ionic migration on the performance of intact unpigmented epoxy coated mild steel under cathodic protection," *Prog. Org. Coatings*, vol. 75, no. 1–2, pp. 79–85, 2012, doi: 10.1016/j.porgcoat.2012.03.011.

[223] Z. Wang, Z. Zhou, W. Xu, L. Yang, B. Zhang, and Y. Li, "Study on inner corrosion behavior of high strength product oil pipelines," *Eng. Fail. Anal.*, vol. 115, 2020, doi: 10.1016/j.engfailanal.2020.104659.

[224] E. O. Eltai, J. D. Scantlebury, and E. V. Koroleva, "Protective properties of intact unpigmented epoxy coated mild steel under cathodic protection," *Prog. Org. Coatings*, 2012, doi: 10.1016/j.porgcoat.2011.08.012.

[225] S. Banerjee, V. Srivastava, and M. M. Singh, "Chemically modified natural polysaccharide as green corrosion inhibitor for mild steel in acidic medium," *Corros. Sci.*, 2012, doi: 10.1016/j.corsci.2012.02.009.

[226] S. A. Umoren, Z. M. Gasem, and I. B. Obot, "Natural products for material protection: Inhibition of mild steel corrosion by date palm seed extracts in acidic media," *Ind. Eng. Chem. Res.*, 2013, doi: 10.1021/ie401737u.

[227] H. R. Jeon, J. H. Park, and M. Y. Shon, "Corrosion protection by epoxy coating containing multi-walled carbon nanotubes," *J. Ind. Eng. Chem.*, 2013, doi: 10.1016/j.jiec.2012.10.030.

[228] A. M. Amaro, P. N. B. Reis, M. A. Neto, and C. Louro, "Effects of alkaline and acid solutions on glass/epoxy composites," *Polym. Degrad. Stab.*, 2013, doi:

10.1016/j.polymdegradstab.2012.12.029.

[229] S. Kajorncheappunngam, R. K. Gupta, and H. V. S. GangaRao, "Effect of Aging Environment on Degradation of Glass-Reinforced Epoxy," *J. Compos. Constr.*, 2002, doi: 10.1061/(asce)1090-0268(2002)6:1(61).

[230] D. Kotnarowska, "Epoxy coating destruction as a result of sulphuric acid aqueous solution action," *Prog. Org. Coatings*, 2010, doi: 10.1016/j.porgcoat.2009.10.026.

[231] J. D. Tanks, Y. Arao, and M. Kubouchi, "Diffusion kinetics, swelling, and degradation of corrosion-resistant C-glass/epoxy woven composites in harsh environments," *Compos. Struct.*, vol. 202, pp. 686–694, 2018, doi: 10.1016/j.compstruct.2018.03.078.

[232] E. Solis-Ramos and M. Kumosa, "Synergistic effects in stress corrosion cracking of glass reinforced polymer composites," *Polym. Degrad. Stab.*, vol. 136, pp. 146–157, 2017, doi: 10.1016/j.polymdegradstab.2016.12.016.

[233] ASTM, "Standard guide for laboratory immersion corrosion testing of metals," *ASTM Int.*, vol. G31-12a, pp. 1–10, 2012.

[234] A. E. Krauklis and A. T. Echtermeyer, "Mechanism of yellowing: Carbonyl formation during hygrothermal aging in a common amine epoxy," *Polymers (Basel).*, 2018, doi: 10.3390/polym10091017.

[235] K. T. Hassan, "Study the Effect of Some Solutions on Epoxy Resin & Calculate Diffusion Coefficient of Solution.," *J. Univ. anbar pure Sci.*, vol. 4, no. 1, 2010.

[236] W. L. Methods, "Standard Test Methods for Corrosivity of Water in the Absence of Heat Transfer," *Corrosion*, 1999.

[237] A. G.-03 Standard, "ASTM G1 - 03 Standard Practice for Preparing, Cleaning, and Evaluating Corrosion Test Specimens.," *ASTM Spec. Tech. Publ.*, 1985.

[238] Y. Wan *et al.*, "Insight into atmospheric pitting corrosion of carbon steel via a dual-beam FIB/SEM system associated with high-resolution TEM," *Corros. Sci.*, 2019, doi: 10.1016/j.corsci.2019.03.017.

[239] Y. Wang, G. Cheng, W. Wu, Q. Qiao, Y. Li, and X. Li, "Effect of pH and chloride on the micro-mechanism of pitting corrosion for high strength pipeline steel in aerated NaCl solutions," *Appl. Surf. Sci.*, 2015, doi: 10.1016/j.apsusc.2015.05.053.

[240] S. Nasrazadani and A. Raman, "The application of infrared spectroscopy to the study of rust systems-II. Study of cation deficiency in magnetite (Fe_3O_4) produced during its transformation to maghemite (γ-Fe_2O_3) and hematite (α-Fe_2O_3)," *Corros. Sci.*, 1993, doi: 10.1016/0010-938X(93)90092-U.

[241] M. Safiur Rahman, M. Whalen, and G. A. Gagnon, "Adsorption of dissolved organic matter (DOM) onto the synthetic iron pipe corrosion scales (goethite and magnetite): Effect of pH," *Chem. Eng. J.*, 2013, doi: 10.1016/j.cej.2013.08.077.

[242] P. Sarin, V. L. Snoeyink, J. Bebee, W. M. Kriven, and J. A. Clement, "Physico-chemical characteristics of corrosion scales in old iron pipes," *Water Res.*, 2001, doi: 10.1016/S0043-1354(00)00591-1.

[243] V. I. Grokhovsky, M. I. Oshtrakh, O. B. Milder, and V. A. Semionkin, "Mössbauer spectroscopy of iron meteorite Dronino and products of its corrosion," *Hyperfine Interact.*, 2005, doi: 10.1007/s10751-006-9339-9.

[244] H. Namduri and S. Nasrazadani, "Quantitative analysis of iron oxides using

Fourier transform infrared spectrophotometry," *Corros. Sci.*, 2008, doi: 10.1016/j.corsci.2008.06.034.

[245] J. W. Anthony, *Handbook of Mineralogy. Vol. 3: Halides, hydroxides and oxides*. 1997.

[246] R. L. Tallman, J. L. Margrave, and S. W. Bailey, "The Crystal Structure of Sodium Peroxide," *J. Am. Chem. Soc.*, 1957, doi: 10.1021/ja01568a087.

Appendix A: Electrochemical Impedance Spectroscopy (EIS) Component Values

Table 25. EIS component values for glass/epoxy in 0.5 M NaCl solution.

Components	5 h	10 h	15 h	20 h	25 h
R_s (ohms)	47.73e-3	29.04e-3	10.70e-3	16.58e-3	105.2e-3
R_{cor} (ohms)	143.0e6	273.4e6	671.4e6	2.493e9	334.7e6
R_{po} (ohms)	8.024e6	10.24e6	9.904e6	12.24e6	16.50e6
C_{cor} (S*s^a)	50.12e-9	54.08e-9	65.27e-9	49.51e-9	45.47e-9
n	703.4e-3	707.3e-3	638.7e-3	676.5e-3	696.8e-3
Cc (S*s^a)	189.8e-12	193.6e-12	184.3e-12	179.2e-12	183.7e-12
m	956.0e-3	952.9e-3	957.9e-3	960.0e-3	957.8e-3
Goodness of Fit	1.930e-3	2.267e-3	1.529e-3	1.492e-3	2.082e-3

Table 26. EIS component values for Kevlar/epoxy in 0.5M NaCl solution.

Components	5 h	10 h	15 h	20 h	25 h
R_s	76.75e-3	50.04e-3	40.45e-3	4.253e-3	39.13e-6
R_{cor}	941.1e6	3.575e9	3.148e9	2.212e9	1.498e9
R_{po}	6.411e6	517.8e3	227.4e3	68.68e3	27.74e3
C_{cor}	239.1e-12	154.8e-12	191.8e-12	173.8e-12	213.5e-12
n	473.5e-3	347.1e-3	469.7e-3	346.4e-3	414.2e-3
Cc	153.6e-12	159.5e-12	157.2e-12	165.7e-12	149.5e-12
m	972.9e-3	969.0e-3	970.9e-3	966.4e-3	975.3e-3
Goodness of Fit	447.7e-6	898.8e-6	630.2e-6	688.5e-6	663.0e-6

Table 27. EIS component values for Epoxy in 0.5M NaCl solution.

Components	5 h	10 h	15 h	20 h	25 h
R_s	10.77e-3	37.80e-3	3.928e-3	108.0e-3	65.71e-3
R_{cor}	598.9e6	254.8e6	542.3e6	3.482e9	37.37e9
R_{po}	10.03e6	7.946e6	6.309e6	7.581e6	4.349e15
C_{cor}	1.556e-9	1.786e-9	1.698e-9	1.387e-9	197.7e-9
n	838.1e-3	815.2e-3	811.5e-3	813.1e-3	9.127e-3
Cc	91.18e-12	94.68e-12	93.02e-12	91.63e-12	1.379e-9
m	993.1e-3	990.6e-3	992.7e-3	993.7e-3	773.4e-3
Goodness of Fit	1.265e-3	1.717e-3	1.577e-3	2.220e-3	89.93e-3

Table 28. EIS component values for Glass/epoxy in 0.5M HCl solution.

Components	5 h	10 h	15 h	20 h	25 h
R_s	26.15e-3	114.6e-6	229.1e-3	5.399e-3	861.1e-6
R_{cor}	1.036e6	146.9e3	9.009e9	10.32e9	8.902e9
R_{po}	7.123e9	1.366e9	3.595e6	8.786e6	117.0e3
C_{cor}	5.065e-12	9.671e-9	94.52e-12	78.00e-12	72.67e-12
n	863.1e-3	20.00e-3	606.9e-3	524.6e-3	395.3e-3
Cc	162.9e-12	184.6e-12	107.9e-12	114.0e-12	122.3e-12
m	951.2e-3	942.4e-3	990.2e-3	986.3e-3	981.0e-3
Goodness of Fit	6.144e-3	5.828e-3	378.1e-6	224.7e-6	415.8e-6

Table 29. EIS component values for Kevlar/epoxy in 0.5M HCl solution.

Components	5 h	10 h	15 h	20 h	25 h
R_s	356.9e-6	47.09e-3	331.9e-6	55.05e-6	2.008e-3
R_{cor}	193.5e9	71.77e9	123.1e9	34.25e9	6.792e9
R_{po}	45.03e3	493.0e6	5.721e3	867.7e3	3.874e6
C_{cor}	168.7e-12	157.6e-12	175.6e-12	144.3e-12	102.9e-12
n	563.6e-3	598.9e-3	539.8e-3	553.6e-3	485.0e-3
Cc	136.6e-12	158.5e-12	140.1e-12	146.5e-12	159.3e-12
m	978.4e-3	968.0e-3	979.5e-3	976.5e-3	970.5e-3
Goodness of Fit	311.4e-6	641.4e-6	671.8e-6	544.8e-6	798.3e-6

Table 30. EIS component values for Epoxy in 0.5M HCl solution.

Components	5 h	10 h	15 h	20 h	25 h
R_s	927.1e-6	4.228e-3	169.0e-3	1.311e-3	223.2e-3
R_{cor}	371.8e3	5.160e9	2.188e9	140.2e3	260.5e3
R_{po}	1.367e9	514.8e3	1.454e6	2.033e9	1.186e9
C_{cor}	11.43e-12	31.89e-12	42.23e-12	4.212e-9	858.1e-15
n	954.1e-3	591.3e-3	658.5e-3	219.7e-3	20.00e-3
Cc	96.99e-12	79.58e-12	70.15e-12	87.87e-12	92.55e-12
m	961.0e-3	981.1e-3	992.9e-3	974.5e-3	971.3e-3
Goodness of Fit	2.320e-3	1.509e-3	3.533e-3	1.503e-3	2.169e-3

Table 31. EIS component values for Glass/epoxy in 0.5M H_2SO_4 solution.

Components	5 h	10 h	15 h	20 h	25 h
R_s	337.5	489.4	702.1	851.2	857.5
R_{cor}	1.445e6	36.04e3	13.85e9	9.745e9	7.056e9
R_{po}	2.925e9	10.61e9	237.6e6	4.675e9	9.680e9
C_{cor}	18.88e-12	484.1e-9	18.41e-12	35.52e-12	54.42e-12
n	930.8e-3	16.29e-3	426.1e-3	761.1e-3	968.5e-3
Cc	59.57e-12	60.57e-12	63.61e-12	63.46e-12	66.70e-12
m	996.6e-3	998.7e-3	991.7e-3	994.8e-3	997.7e-3
Goodness of Fit	2.652e-3	2.983e-3	1.803e-3	4.345e-3	1.760e-3

Table 32. EIS component values for Kevlar/epoxy in 0.5M H_2SO_4 solution.

Components	5 h	10 h	15 h	20 h	25 h
R_s	57.85e-3	1.975e-3	2.837e-3	69.52e-3	153.2e-3
R_{cor}	4.708e9	125.3e9	1.577e9	10.10e6	567.5e3
R_{po}	1.788e9	18.79e6	5.657e6	373.4e3	112.7e3
C_{cor}	49.50e-12	40.95e-12	704.1e-12	19.23e-9	126.0e-9
n	887.4e-3	506.1e-3	776.1e-3	772.3e-3	776.1e-3
Cc	97.43e-12	106.1e-12	113.5e-12	155.1e-12	253.8e-12
m	979.7e-3	983.5e-3	986.5e-3	970.8e-3	942.9e-3
Goodness of Fit	364.7e-6	649.9e-6	1.001e-3	242.5e-6	1.140e-3

Table 33. EIS component values for Epoxy in 0.5M H_2SO_4 solution.

Components	5 h	10 h	15 h	20 h	25 h
R_s	354.4e-3	220.3e-3	1.686e-3	41.17e-3	27.21e-3
R_{cor}	18.94e6	11.61e9	35.75e6	68.37e6	3.571e9
R_{po}	16.85e9	28.64e9	11.81e9	22.49e9	5.868e6
C_{cor}	678.7e-15	61.11e-12	248.7e-15	1.128e-18	1.495e-15
n	912.0e-3	998.1e-3	973.3e-3	801.4e-3	827.6e-3
Cc	60.22e-12	61.71e-12	64.21e-12	64.94e-12	68.77e-12
m	1.000	1.000	1.000	1.000	1.000
Goodness of Fit	3.370e-3	6.540e-3	5.898e-3	11.53e-3	8.195e-3